MOLECULAR MODELLING OF THE EFFECT OF ALKALI PROMOTERS ON CO ADSORPTION AND DISSOCIATION ON THE Co(111) SURFACE

A Thesis Submitted to
the Graduate School of Engineering and Sciences of
İzmir Institute of Technology
in Partial Fulfillment of the Requirements for the Degree of

MASTER OF SCIENCE

in Chemical Engineering

by
Özüm ÖZBEK

December 2023
İZMİR

We approve the thesis of **Özüm ÖZBEK**

Examining Committee Members:

Assist. Prof. Dr. Ali Can KIZILKAYA
Department of Chemical Engineering, Izmir Institute of Technology

Prof. Dr. Erol ŞEKER
Department of Chemical Engineering, Izmir Institute of Technology

Assoc. Prof. Dr. Murat Oluş ÖZBEK
Department of Chemical Engineering, Gebze Technical University

8 December 2023

Assist. Prof. Dr. Ali Can KIZILKAYA
Supervisor, Department of Chemical
Engineering, Izmir Institute of Technology

Prof. Dr. Aysun SOFUOĞLU
Head of the Department of
Chemical Engineering

Prof. Dr. Mehtap EANES
Dean of the Graduate School of
Engineering and Sciences

ACKNOWLEDGEMENTS

I would like to express my deep gratitude to my thesis supervisor, Dr. Ali Can KIZILKAYA for his constant support, encouragement, and mentorship throughout this research work. I am truly appreciative of the invaluable insights and constructive feedback provided by Professor Kızılkaya which have not only enriched my knowledge but also inspired me to strive for excellence. His belief in my potential and his dedication to my success have been truly inspiring. I am honored to have had Professor Kızılkaya as a mentor, and I will carry the knowledge and skills gained under his guidance throughout my life.

I also would like to thank my family for their love, support, and encouragement throughout my academic journey. Especially, I want to offer a heartfelt acknowledgment to my beloved sister, Begüm ÖZBEK, whose unwavering support and encouragement have been the bedrock of my academic and personal development. Her guidance, motivation, and belief in my abilities have been my constant motivation.

I want to extend my heartfelt appreciation to my dedicated teammate, Dilan TUNÇER, who has been not just a research partner but also a trusted friend. I am thankful for the strong bond we have built in our research group. I also want to thank my beloved friends, Özgün ŞATIR, İrem YAKAR, Simge KOSTİK, Yağmur ÇETİN and Bulut Cem ÖCAL as their constant support, laughter, and trusted friendship have brought immeasurable joy to my journey.

I would like to thank two incredibly special people in my life, Onur İPEK and Büşra SEZEN. Your love has given me the strength to pursue my goals and the courage to face life's challenges. Your belief in me and our shared dreams has been the strength to pursue my goals. I am incredibly grateful for your presence in my life, and I dedicate my achievements to you, as they are a reflection of the support, love, and encouragement you have showered upon me.

ABSTRACT

MOLECULAR MODELLING OF THE EFFECT OF ALKALI PROMOTERS ON CO ADSORPTION AND DISSOCIATION ON THE Co(111) SURFACE

Fischer-Tropsch Synthesis (FTS) is a surface polymerization process that has been industrially used to convert non-petroleum feedstocks to synthetic transportation fuels. Modification with an alkali promoter of the Co-based catalysts provided promising results to obtain hydrocarbons with enhanced olefin content in FTS. Activation of CO is the key factor to achieve desired end products in FTS, yet the mechanism related to the CO dissociation behavior on alkali promoted cobalt surfaces remains unknown. This study aims to examine the impact of alkali promoters (Li, Na, K) on the adsorption and dissociation characteristics of CO on the Co(111) surface using Density Functional Theory (DFT). Our results revealed that CO adsorption energy increased by 32-37% with alkali addition, yet H adsorption energy remained relatively unchanged. The effect of alkali addition on CO dissociation routes were also examined. The high activation barrier (>200 kJ/mol) makes it improbable for direct CO dissociation to occur on alkali promoted Co(111) surfaces under FTS conditions. For H-assisted pathways, alkali addition increased the activation barrier for HCO and H_2CO dissociation, overall reducing the H-assisted CO dissociation rate. It was found that alkali addition makes the surface more carbophilic since the C adsorption energy increased by 7-11% upon alkali addition. Also, with increasing C concentration on the Co(111) surface, subsurface carbon geometries became more stable. Ultimately, it is concluded that alkali promoters of Li, Na and K have similar effects on CO adsorption and dissociation on the Co(111) surface.

ÖZET

ALKALİ GELİŞTİRİCİLERİN Co(111) YÜZEYİNDEKİ CO ADSORPSİYONUNA VE AYRIŞMASINA OLAN ETKİSİNİN MOLEKÜLER MODELLENMESİ

Fischer-Tropsch Sentezi, petrol dışı hammaddeleri sentetik ulaşım yakıtlarına dönüştürmek için endüstriyel olarak kullanılan bir yüzey polimerizasyon reaksiyonudur. Kobalt bazlı katalizörlerin bir alkali geliştirici ile modifikasyonu, FTS'de arttırılmış olefin içeriğine sahip hidrokarbonlar elde etmek adına umut verici sonuçlar doğurmuştur. CO'nun aktivasyonu, FTS'de istenen son ürünleri elde etmek için kilit bir faktördür, ancak alkali geliştiriciye sahip kobalt yüzeylerindeki CO ayrışma davranışı ile ilgili mekanizma hala bilinmemektedir. Bu çalışma, alkali geliştiricilerin (Li, Na, K), Co(111) yüzeyindeki CO adsorpsiyon ve ayrışma davranışına olan etkisini Yoğunluk Fonksiyonel Teorisi (DFT) kullanarak incelemeyi amaçlamıştır. Adsorpsiyon çalışmaları alkali ilavesi ile CO adsorpsiyon enerjisinin %32-37 oranında arttığını ancak H adsorpsiyon enerjisinin nispeten değişmediğini ortaya koymuştur. Alkali ilavesinin CO'nun ayrışma yolları üzerindeki etkisi de incelenmiştir. Yüksek aktivasyon bariyeri (>200 kJ/mol), FTS koşulları altında alkali destekli Co(111) yüzeylerinde doğrudan CO ayrışmasının meydana gelmesini imkansız hale getirir. H destekli yollar için alkali ilavesi, HCO ve H_2CO ayrışmasına yönelik aktivasyon bariyerini arttırmıştır ve genel olarak H destekli CO ayrışma hızını düşürmüştür. Alkali ilavesi üzerine C adsorpsiyon enerjisinin %7-11 oranında artması nedeniyle alkali ilavesinin yüzeyi daha karbofilik hale getirdiği bulunmuştur. Ayrıca Co(111) yüzeyinde C konsantrasyonunun artmasıyla birlikte yüzey altı karbon geometrileri daha kararlı hale gelmiştir. Nihai olarak, Li, Na ve K alkali geliştiricilerinin Co(111) yüzeyinde CO adsorpsiyonu ve ayrışması üzerinde benzer etkilere sahip olduğu sonucuna varılmıştır.

TABLE OF CONTENTS

LIST OF FIGURES

Figure **Page**

LIST OF TABLES

Dedicated to my family,

CHAPTER 1

INTRODUCTION

Greenhouse gas emissions resulting from the fossil fuel usage possess a great threat to environment and humans. Many recent investigations focus on finding alternative pathways to produce energy to mitigate human civilization's current reliance on fossil fuels. Among various energy conversion technologies, Fischer-Tropsch Synthesis (FTS) stands out as it is a surface polymerization reaction that converts carbonaceous feedstocks to high quality synthetic transportation fuels. Even though Fischer-Tropsch synthesis is an industrially applied technology, it still faces challenges to overcome to compete with current crude oil market.

Cobalt-based FT catalysts are highly applied in the literature due to their various advantages such as high activity, high stability, and high C-C chain growth ability. The resulting products of cobalt-based catalysts are usually enriched in paraffins. However, in order to improve engine efficiency and environmental compliance, olefin content in liquid fuels needs to be enhanced. Modification of cobalt catalysts with alkali promoters was found to be an effective way to produce hydrocarbons with high olefin content.

Although the common view is that alkali promoters increase the selectivity of olefinic products, there are contradictory arguments in the literature on the effects of alkalis since several experimental studies revealed that activity and selectivity values change for different alkali promoters [1,2]. The fundamental reason for this difference has not been clearly explained to this day. In addition, although the mechanism of Fischer-Tropsch synthesis is still not fully resolved due to the complexity of the reaction, it is known that CO activation is the key factor to obtain the desired products. However, up to our knowledge, there are no experimental or computational studies exist in the literature that investigate the CO dissociation mechanism on alkali promoted cobalt catalysts.

Fundamental understanding of reaction mechanisms is essential in the field of catalysis for the rational design and fine-tuning of chemical processes and enhancing

the efficiency and selectivity of chemical reactions. Computational catalyst design has gained a lot of attention over the years as it provides accurate information about the chemical phenomena occurring at the nanoscale on catalyst surfaces without time and cost constraints. It helps researchers to access insights that would be either very difficult or not possible to obtain through experimental means and design more effective and sustainable catalysts through changes made at the atomic level.

The aim of this study is to analyze the effect of different alkali promoters (Li_2O, Na_2O, K_2O) on CO adsorption and dissociation on the Co(111) surface by using Density Functional Theory (DFT) calculations. In order to achieve this goal, detailed investigations based on adsorption studies, vibrational frequency calculations, electronic charge analysis and transition state calculations were performed. Our calculations show important mechanistic effects of alkali promoters on the adsorption and dissociation behavior of CO on the planar Co(111) surface.

CHAPTER 2

BACKGROUND INFORMATION

2.1 Global Energy Crisis and the Effect of Fossil Fuels on Environment

Energy plays a fundamental role in economic growth as numerous production and consumption activities rely on it as a fundamental input. Nevertheless, the majority of the energy (%75) used today is generated from fossil fuels [3]. Humans are highly dependent on fossil fuels for transportation, power generation, and industrial purposes. However, depletion of fossil fuel resources and increased energy demand due to increasing population along with the environmental concerns have led to research on renewable and clean energy sources.

Carbon dioxide emissions resulting from fossil fuel consumption are the largest contributor of global greenhouse gas emissions, with a share of about 72% [3]. Carbon neutrality accounts for achieving a state of equilibrium by both minimizing carbon dioxide emissions and eliminating the residual carbon dioxide from the atmosphere. Transportation serves as the cornerstone of every civilization, as it plays a vital role in economic growth. However, harmful emissions resulting from the fossil fuels in transportation engines have pushed this sector far from achieving carbon neutrality. Globally, 14% of the greenhouse emissions come from transportation sector which is the second biggest contributor after electricity and heat production [4]. Transportation sector is highly dependent on fossil fuels considering that 95.9% of it is supplied by fossil fuels, 1.0% from non-renewable electricity and only 3.1% are supplied by renewable energy sources [5]. Approximately 40% of greenhouse gas emissions in urban areas originate from fossil fuel-powered vehicles. Moreover, toxic gases (CO_2, CO, NO_x, SO_2, HC, C_6H_6) emitted from vehicles not only change the climate but also significantly affect human health by causing fatal diseases like cancer. That's why

replacing the petroleum derived fuels with renewable energy sources is essential to reduce air pollution and decrease the reliance on petroleum-based products.

2.2 Alternative Routes to Replace Fossil Fuels

Global efforts are presently in progress to seek alternative fuels that can fulfill the current and future energy requirements while decreasing the global warming effects. Highly investigated energy production alternatives are vegetable oils, ethanol, biodiesel, hydrogen, and synthetic fuels resulting from the Coal to Liquid (CTL) technologies.

Vegetable oils are a group of fats that are extracted from various plant sources which have gained attention as alternatives for conventional fuels. Vegetable oils can be used purely or as blends of different vegetable oils. However, it is reported that application of vegetable oils in diesel engines are challenging due to its properties such as high viscosity and unsaturated hydrocarbon chain reactivity [6]. These properties of vegetable oils potentially result in improper fuel combustion and higher air pollution emission [6].

Alcohol has been also proposed as an alternative to conventional fuels since it has a better anti-knock property than gasoline. Additionally, alcohols have lower CO and unburnt hydrocarbons emissions [7]. Due to their high flash point, alcohols are safe to store and transport. However, alcohols are not widely used in engines due to their high price and their technical limitations. As an example, ethanol's compatibility with water can lead to corrosion in metallic engine components. Additionally, ethanol requires a larger quantity than gasoline to produce an equivalent amount of energy, owing to its lower heating value [7].

Biodiesel, also referred to as fatty acid methyl ester (FAME), is fully compatible with conventional diesel engines, requiring no modifications. This compatibility has the potential to decrease pollutant emissions and reduce exposure to potential carcinogens [8]. Biodiesel has various advantageous properties, such as good lubricity and high flash point [9]. Also, biodiesel is renewable, biodegradable, non-toxic, and it is free of sulfur and aromatics [8]. Biodiesel is non-toxic as it is produced from natural and renewable sources [10]. However, due to its oxidation and polymerization during combustion or

storage, biodiesel is still not fully compatible with conventional fuels [7]. Also, the production cost of biodiesel remains 1.5–3 times higher than that of petroleum-based diesel [9].

Hydrogen has drawn attention as a potential substitute for traditional petroleum-based fuels due to its nearly emissions-free characteristics. Hydrogen can serve as a compact energy source in fuel cells and batteries but efficient storage of hydrogen is still an ongoing research topic [7]. Sangeeta et al. reported that no approach has successfully met the technical requirements for hydrogen storage while simultaneously satisfying all performance criteria up to this day [7].

Coal liquefaction (Coal to Liquid or CTL) involves the transformation of solid coal into liquid fuels and chemicals. Two distinct approaches have been employed to accomplish this task, which are direct coal liquefaction (DCL) and indirect coal liquefaction (ICL) [7]. In direct coal liquefaction, coal undergoes direct hydrogenation. However, direct coal liquefaction is not favored due to challenges related to the poor mixing of the three phases in the slurry-phase reactor, which requires the use of heavy-duty pumps for recirculation [7].

Indirect coal liquefaction begins with coal gasification, which breaks down coal into synthesis gas ($CO + H_2$). Then, this syngas can be transformed into liquid fuels and valuable chemicals with the aid of proper catalysts. In addition to coal, synthesis gas can be produced from wide range of non-petroleum carbon resources to produce various hydrocarbon fuels and chemicals [11]. Syngas conversion has drawn rousing attention over the years because it is an efficient and environmentally friendly technology to replace the existing dependence on petroleum products. Figure 1 represents the possible end products that can be obtained from syngas conversion through different routes. Syngas mainly consist of CO and H_2. However, depending on the nature of the feedstock, it may contain small amounts of CO_2, CH_4, and N_2. Also, different feedstocks will result in different CO/H_2 ratios which will affect the resulting end product and selectivity [12].

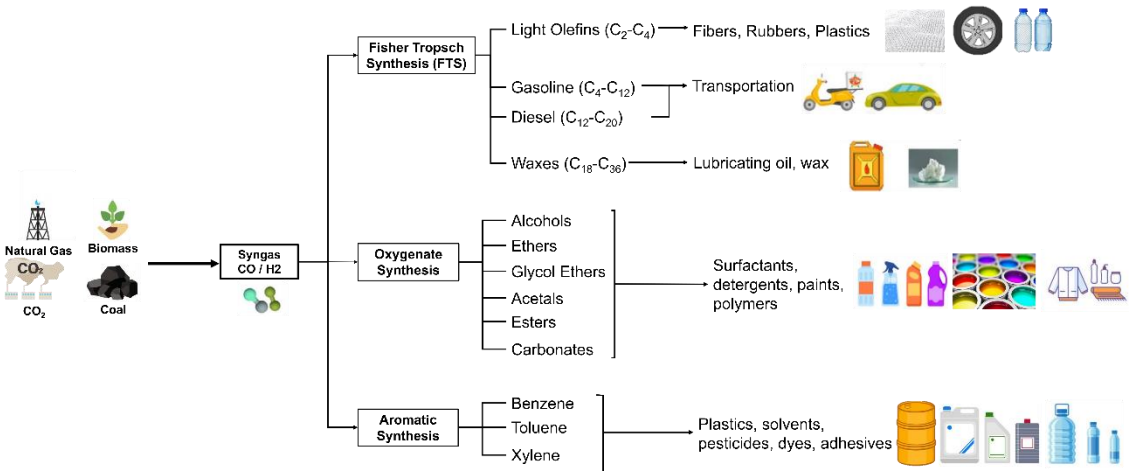

Figure 1. Possible syngas conversion routes to value added products. Original drawing prepared by the author.

Production of liquid fuels through syngas conversion via Fischer-Tropsch synthesis has gained a lot of attention over the academia and industry as the fuels generated via Fischer-Tropsch synthesis are fully compatible with modern diesel and gasoline-powered vehicles [7]. The ability to perform Fischer-Tropsch synthesis with syngas produced from any carbon source increases its attractiveness for researchers. Fischer-Tropsch synthesis has high thermal and carbon conversion efficiency. Additionally, fuels produced through Fischer-Tropsch synthesis exhibit significantly reduced levels of nitrogen oxides (NO_x) and particulate emissions [13]. Furthermore, transitioning from petroleum to FTS fuel does not require infrastructure changes for distribution or storage. Indeed, both coal and natural gas-based Fischer-Tropsch plants are currently in commercial operation. South Africa has three coal-based plants operated by Sasol, while PetroSA and Shell have been running two natural gas plants in South Africa and Malaysia, respectively [13]. Even though FTS is an already applied technology in the industry. There are still major challenges to overcome regarding its globalization and compatibility with conventional petroleum-based fuels.

2.3 Fischer-Tropsch Synthesis

Fischer-Tropsch synthesis is a chemical process that involves the catalytic conversion of synthesis gas (syngas, CO and H_2) into various hydrocarbons, where the mechanism was first proposed by German scientists Hans Fischer and Franz Tropsch in 1925 [11]. FT synthesis has been extensively used throughout the industry since the resulting products of FT synthesis include a wide range of hydrocarbons which are further upgraded to sulfur and aromatic free transportation fuels such as liquefied petroleum gas (LPG), gasoline, jet fuel, diesel, and wax [11,12]. Another major product of FT synthesis is light olefins (C_2-C_4) which are referred to as the building blocks of many chemical compounds [11,14].

2.3.1 Mechanism of Fischer-Tropsch Synthesis

Fischer-Tropsch synthesis is a very complex process that involves multiple steps and the exact mechanism of the FT reaction is still a subject of ongoing research. In particular, CO dissociation pathways that form monomers and chain growth mechanisms remain largely unresolved. FT synthesis proceeds through three main steps which are initiation, chain growth and chain termination.

Many reaction pathways have been proposed to explain the complicated mechanism of FT synthesis. Figure 2 represents the three most outstanding FT synthesis pathways which are the carbide mechanism, the CO insertion mechanism, and the hydroxycarbene mechanism.

Carbide mechanism was originally proposed by Franz Fischer and Hans Tropsch in 1926 [15]. In the carbide mechanism, both carbon monoxide and hydrogen are chemisorbed on a metal surface and subsequently dissociate into their monomeric units. The reaction between surface carbon and hydrogen generates CH_x intermediate species. A low CO dissociation barrier is required for carbide mechanism such that the methane formation occurs slower than CO activation and therefore chain growth is promoted [15]. However, the calculated activation barriers for CO dissociation on Co(111) and

Co(0001) surfaces are usually above 200 kJ/mol which does not explain the observed TOF values during FT synthesis [16,17]. Also, the calculated CO dissociation barrier during real-time FT synthesis varies between 100-200 kJ/mol [18]. Therefore, alternative pathways such as H-assisted routes and CO insertion have been proposed.

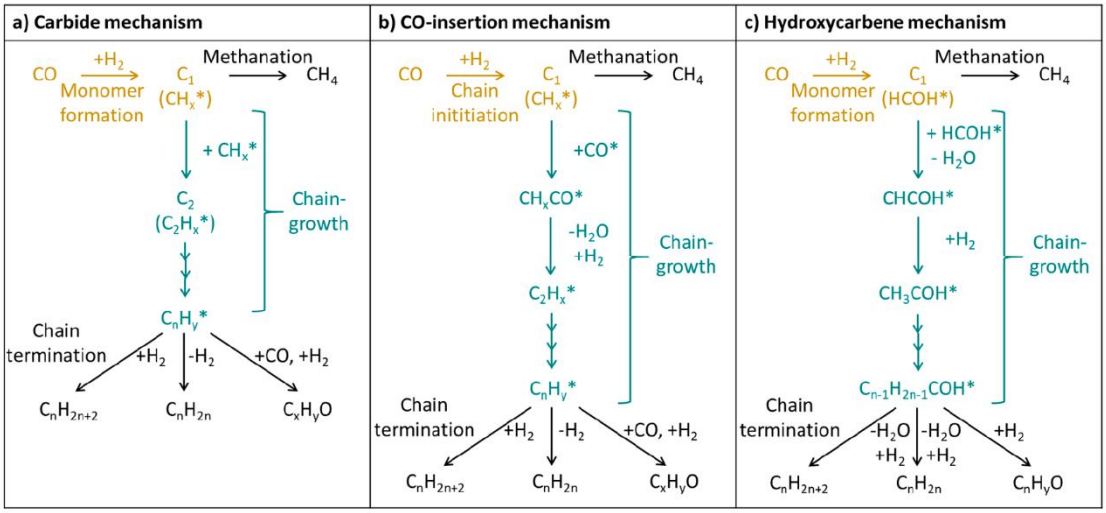

Figure 2. a) Carbide mechanism, b) CO-insertion mechanism and c) Hydroxycarbene mechanism for chain growth in FT synthesis [15]

The presence of hydrogen on the catalyst surface can significantly influence the CO dissociation mechanism and reduce the energy barrier for the reaction. In the context of hydrogen-assisted Fischer-Tropsch (FT) synthesis, CO molecules are not directly dissociated on the metal surface. Firstly, CO forms intermediates such as HCO, COH, and CH_2O with H* species and then these intermediates dissociate into CH_x monomers [19]. Experimental and computational studies revealed that the H-assisted assisted pathway significantly decreases the activation barrier for CO activation [18–20].

The CO insertion mechanism was initially proposed by Pichler and Schulz in 1970 [21]. In the process of CO insertion, CO serves as the monomeric unit that inserts itself into the developing chain, subsequently undergoing hydrogenation and C−O bond cleavage [14]. It differs from the carbide mechanism primarily due to the formation and breaking of carbon-oxygen bonds. In the carbide mechanism, cleavage of the C−O bond occurs first whereas in the CO insertion mechanism the formation of the C−C bond

happens first [15]. In this mechanism, chain growth proceeds through the coupling of CO with an RCH_2 group, rather than through the coupling of two CH_2 groups. As a result, this mechanism doesn't rely on a high surface concentration of CH_2 groups to facilitate rapid chain growth compared to chain termination [18].

The third established mechanism for Fischer-Tropsch synthesis is referred to as the hydroxycarbene mechanism. Contrary to the CO insertion mechanism, CO first hydrogenates to HCO* and subsequently further hydrogenates into HCOH* [14]. Within the hydroxycarbene mechanism, HCOH* engages in condensation polymerization with an extending RCOH* chain [15]. The elimination of water through the condensation of two hydroxymethylene groups facilitates the creation of C-C bonds [14]. The expansion of the chain is facilitated through the collaboration of oxygenated surface intermediates [14].

2.3.2 Operating Conditions of FTS

FT synthesis reaction involves the exothermic polymerization process where the product selectivity depends on the feed composition, catalyst selection and operating conditions [12]. Figure 3 summarizes the product distribution of FT synthesis based on catalyst selection and operating conditions. FT synthesis is divided into two categories based on operating conditions [11,12,22]. Different FT synthesis conditions are:

- **High Temperature Fischer-Tropsch (HTFT):** High Temperature Fischer-Tropsch synthesis operates at temperatures 300-350 ºC (20-40 bar) and iron (Fe) is used as the preferred catalyst. Main final products are gasoline and light olefins.
- **Low Temperature Fischer-Tropsch (LTFT):** Low Temperature Fischer-Tropsch is operated at 200-250 ºC (20-40 bar) and iron (Fe) and cobalt (Co) are used as catalysts for the reaction. Main final products are diesel and wax.

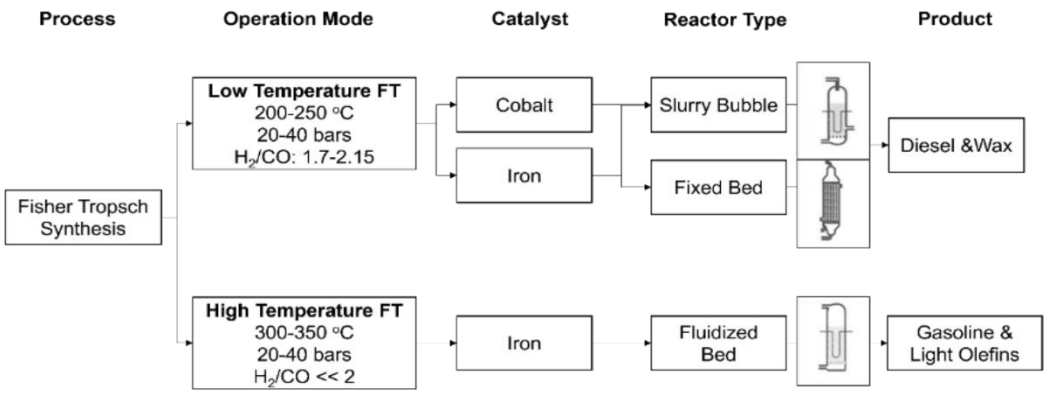

Figure 3. Process scheme for HTFT and LTFT. Original drawing prepared by the author.

Selecting the appropriate reactor in Fischer-Tropsch synthesis is essential for optimizing product distribution, catalyst performance, energy efficiency and scalability. Efficient removal of heat is the essential function of the reactors for the FT synthesis owing to fact that the reaction is highly exothermic. Elevated reaction temperatures result in increased methane production, carbon deposition, and catalyst deactivation [11,12]. For LTFT, slurry bubble bed reactors and tubular fixed bed reactors are industrially used [22]. In slurry bed reactors, effective heat removal is achieved by internal cooling coils. However, separation of product from the catalyst is a major problem. Fixed bed reactors are desirable for their lower maintenance cost and reduced losses due to attrition and wear [11,12,22]. Fixed bed reactors have an upper operating limit of 257 ºC therefore excessing this limit may cause carbon deposition hence blockage of the reactor [12]. For HTFT, circulating fluidized bed reactors are commercially used as temperature control is easy and they have high volumetric capacity [22].

2.3.3. FTS Catalysts

As represented in Figure 1, syngas can be transformed into valuable fuels and chemicals through CO hydrogenation [23]. Activations of both CO and H_2 are crucial factors for syngas conversion to obtain desired end products. CO can undergo both dissociative and non-dissociative adsorption, but dissociative adsorption is required for H_2. CO activation is driven by the electronic nature of metals which is represented in Figure 4.

Transition metals are a primary focus for syngas conversion due to their exceptional capability for adsorbing and dissociating carbon monoxide and hydrogen [11]. Different electronic natures of transition metals result in different CO dissociation behavior which results in different product distribution. As an example, the formation of methanol entails the non-dissociative adsorption of CO on Cu or Pd metals, while the formation of metal carbides involves the dissociative adsorption of CO on W and Mo metals [23].

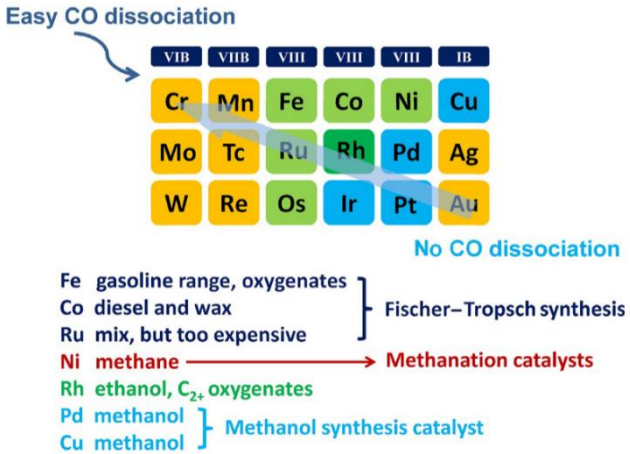

Figure 4. Different CO dissociation characteristics of transition metals and their effect on product distribution [24]

Most of the research on syngas conversion involves designing a stable transition metal-based catalyst with desired selectivity and high activity along with many other structural and chemical properties.

Carbon number distribution of the resulting product of FT synthesis follows the distribution law of Anderson−Schulz−Flory (ASF) (Figure 5) which states that the highest selectivity of products is limited to C_2−C_4 57%, C_5−C_9 39% and C_{10}−C_{20} 39%.

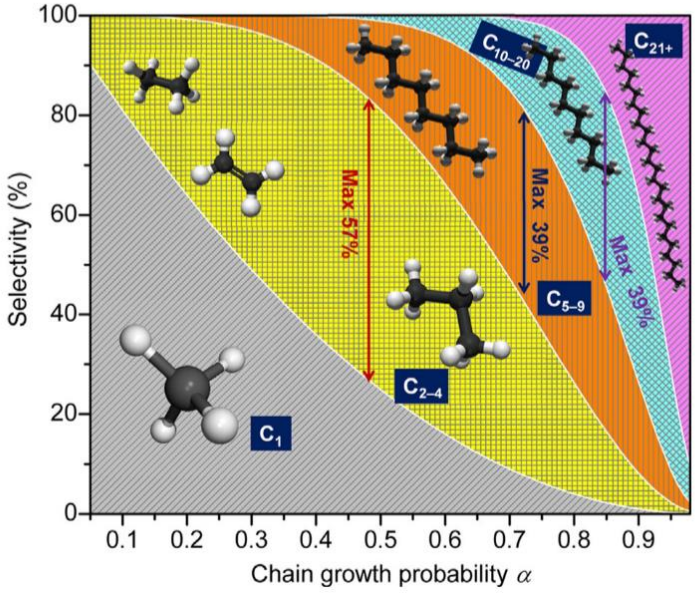

Figure 5. Product distribution of FT synthesis according to Anderson−Schulz−Flory (ASF) model [24]

Reactor type and process conditions can emend product selectivity, but catalysts are the key to achieve desired product selectivity at industrially feasible conditions. The conventional FT process is dominated by three catalysts which are cobalt (Co), iron (Fe) and ruthenium (Ru) because of their exceptional capability to adsorb and dissociate CO and H_2 [11,12,25]. Nickel (Ni) can also be used for FT synthesis, but nickel tends to promote methane formation thus generally it is not preferred. Even though Ru has the highest activity among other proposed catalysts, its high cost and low abundance limits its suitability for industrial applications. It is typically employed as a reduction promoter for cobalt-based FT catalysts [11].

Fe is the most used FT catalyst in the industry because of its advantages such as low methane selectivity, low price, and good catalytic activity [11,12,25]. Fe-based catalysts improve the olefin content due to their weak carbon chain growth ability and suitable hydrogenation strength. Fe can be operated in both high temperature and low temperature regime where Co only operates in the low temperature regime. One drawback of the Fe-based catalysts is the high water-gas-shift (WGS) activity resulting in a significant amount of CO_2. Therefore, iron is more suitable for lower H_2/CO ratio syngas such as those derived from coal or biomass [11,12,25].

Co-based catalysts have higher activity compared to Fe, higher C-C chain growth ability, more stability, lower water gas shift reaction (WGS) activity and longer lifetime [11,12,25]. The cost of Co is significantly higher than Fe but it is a useful alternative since it demonstrates activity at lower pressure where high cost can be offset by lower operating costs. Cobalt catalysts are preferred for FT synthesis using natural gas-derived syngas with a higher H_2/CO ratio and lower sulfur content because cobalt is more sensitive to sulfur impurities compared to Fe [11,12,25].

Essential characteristics of a FT catalyst are the ability to adsorb and dissociate the C-O bond, and good adsorption capacity for H_2. The rate of CO dissociation depends on the control of localized electron density at the active catalyst surface through electronic back donation to the $2\pi^*$ antibonding molecular orbital of CO [12]. Figure 6 represents the effect of electronic back donation of metal particles on the interaction of species. If back-donation is weak, CO will weakly bound on the surface. In opposition, if back-donation is strong, the C-O bond weakens. To achieve desired catalyst selectivity without forming any undesired by-products, the balance of the electron back donation needs to be held. The perfectly balanced electron back donation ability of Co is one of the reasons why Co is one of the most used FT catalysts among others. Active metal's electron density can be altered by incorporating particular promoters and support materials [12].

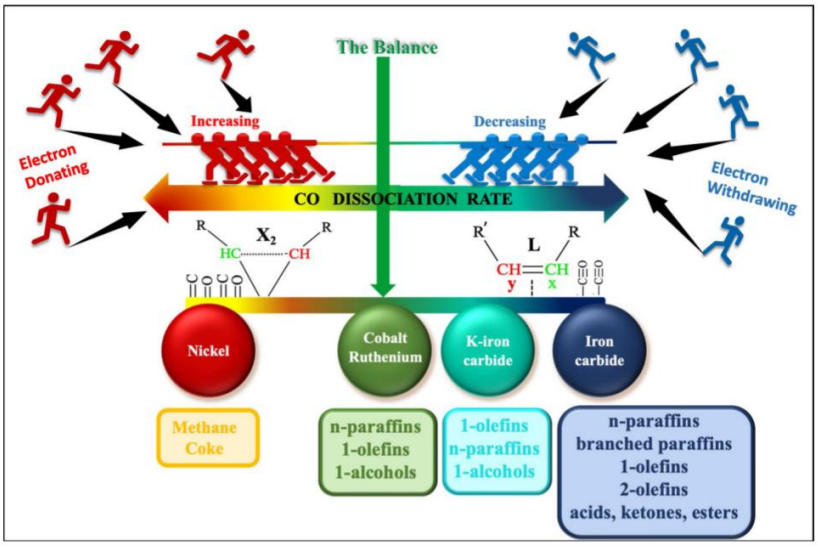

Figure 6. Effect of electronic back donation of metal particle on the interaction of species [12]

2.4 Cobalt-based FTS Catalysts

2.4.1 Catalytic Performance of Cobalt-based FTS Catalysts

Cobalt-based FTS catalysts have attracted attention over the years for the production of long-chain hydrocarbons due to their various properties such as high catalytic activity, low WGSR activity and high stability [11,12,25]. Contrary to Fe-based catalysts, cobalt catalysts are more sensitive to temperature and they can operate well under specifically selected temperatures and H_2/CO ratios. Also, the cobalt catalyst's structure and electron density could be affected by the incorporation of a support or promoter. Table 1 represents the various Co-based catalysts studied on different supporting materials and promoters by different authors.

Table 1. Activity of different Co-based FT catalysts

Catalyst	Promoter	T (°C)	P (bar)	H_2/CO	Product Selectivity (%)	CO conversion(%)	Ref
Co/Al_2O_3	-	220	25	2	90 C_{5+}	25	25
Co/TiO_2	Ag	220	20	2	89 C_{5+}	33.9	26
Co/Al_2O_3	Na	250	-	2	97.4 C_{5+}	48.7	2
Co/ZSM-5	Pt	250	20	2	27 C_{5+}	52.2	11
Co/SBA	-	220	20	2	64.7 C_{5+}	23.1	27
Co/SBA	Re	220	20	2	74.2 C_{5+}	43	27
Co/CNT	Ru	220	20	2	82.5 C_{5+}	31.4	28
Co/SiO_2+ZSM-5	Pt	250	20	2	60.5 C_{12+}	26.4	11
$Co/\alpha-Al_2O_3$	Re	210	20	2	80.8 C_{5+}	42.8	29
Co/SiO_2	-	210	20	2	81.7 C_{5+}	40.4	29
Co/Al_2O_3	Ru	220	22	2.1	85.2 C_{5+}	50.8	2

Aluminum oxide (Al_2O_3), titanium dioxide (TiO_2) and silicon oxide (SiO_2) are the most industrially used supports for cobalt catalysts. TiO_2 is an important support considering its high chemical and thermal stability, corrosion resistance and high specific surface area [11,29]. The metal interaction of TiO_2 is mostly governed by its crystal phase. Shimura et al. investigated the effect of the crystal phase of TiO_2 on Co metal particles at 230 °C and 10 bar in a slurry bed reactor [29]. Their research revealed that Co/TiO_2 catalysts prepared using TiO_2 containing more than 15% rutile phase exhibited approximately four times higher CO conversion rates compared to those derived from pure anatase TiO_2.

SiO_2 is preferred for FTS due to its abilities such as high surface area, narrow pore size distribution and ordered pore structure where those properties can enhance properties of the catalyst such as dispersion, reducibility, and thermal stability [11,29]. Alumina is a widely employed support for FTS catalysts due to its favorable textural properties, which facilitate the loading of active metals and enhance the accessibility of active sites [11]. Storsater et al. investigated the influence of $\gamma-Al_2O_3$, SiO_2 and TiO_2 supports on the shape, appearance, size, and reducibility on Co particles [30]. Particle size and dispersion of the Co^0 and Co_3O_4 particles were calculated by H_2 adsorption and XRD. Calculated results showed that Co^0 and Co_3O_4 particle sizes are controlled by the

pore diameter of the support. The TEM images revealed that on SiO_2 and Al_2O_3, Co_3O_4 appears as agglomerates of different sizes. On TiO_2, Co_3O_4 is found as single particles. The N_2 desorption curve showed that the pore size distribution is broader for the SiO_2 supported catalysts compared to Al_2O_3. The pore size distribution of the TiO_2 supported Co is much broader compared to Al_2O_3 and SiO_2 supports.

Promoters can be used as electronic modifiers, stabilizers, and structural modifiers. Structural promoters (TiO_2, Al_2O_3, and SiO_2) can modify the surface properties and electronic promoters can alter the electron density on the surface of the catalyst. Nobel metals such as platinum (Pt), ruthenium (Ru), and iridium (Ir) are the most used promoters for FTS since they can facilitate reduction and number of active sites [11]. Ma et al. studied the effect of different noble metal promoters (Pd, Pt, and Ru) on the activity and selectivity of Co/Al_2O_3 catalyst at 220 ºC, 22 bar and H_2/CO of 2.1 in CSTR [31]. Their results showed that the addition of noble metal promoters doubled the CO hydrogenation rate as a result of higher Co site density caused by a higher degree of Co reduction. Transition metals such as zirconium (Zr), manganese (Mn) and cerium (Ce) can enhance the catalytic activity by the formation of non-reducible species [11].

In addition to noble and transition metals, alkali and alkali earth metals have drawn much attention due to their various advantages, such as high activity and selectivity to heavier hydrocarbons in FTS with Co catalysts. Also, alkali and alkali earth metals are abundant and much cheaper compared to noble or transition metals. Osa et al. observed the effect of different alkali metals on the Co catalysts and found that addition of alkali promoters to Co catalyst inhibits the water-gas shift reaction and enhance the production of higher molecular hydrocarbons with high olefin content due to increased cobalt reducibility and cobalt active sites [2]. Research has demonstrated that adding a moderate amount of alkali additives can decrease the surface acidity and enhance the CO adsorption capacity of cobalt-based catalysts. This effect results in increased selectivity to 1-olefins and an increase in the olefin/paraffin ratio [32–34]. Alkali promoters also increase the selectivity towards heavier hydrocarbons and act as electron donors hence play an important role in stabilizing the surface structure of the catalyst [32,33]. Zhang et al. reported that the presence of potassium has a substantial influence on the electronic structure of the surface, resulting in a significant decrease in the work function and strong electron polarization [32]. Zhang et al. also reported that alkali suppresses stronger adsorption and enhanced dissociation of CO [35]. Therefore, the

incorporation of alkali metal promoters plays a pivotal role in the carbonization of the cobalt metal phase and in controlling the active components and products of cobalt-based catalysts. As alkali promoters are the primary focus of this study, a comprehensive examination of their characteristics and impact on cobalt-based catalysts is provided in Chapter 3.

2.4.2 Structure-Performance Relationships of Cobalt-based Catalysts in FTS

Fundamentally, catalytic activity and product selectivity in FT synthesis depend directly on the phase and structure of the catalysts utilized in the reaction. Advancements in surface science techniques and real-time characterization methods have played a significant role in enhancing our understanding of the fundamental connection between the catalyst's structure and its performance in the reaction.

2.4.2.1 Effect of Active Phase, Crystallography and Particle Size of Cobalt Nanoparticle in FTS

FTS is a highly structure sensitive reaction as the particle size and crystallographic structure of Co nanoparticle significantly influences the activity and selectivity which is proven by experimental and computational studies [36–39]. Understanding the chemical state of the active sites and phases is essential for designing Fischer-Tropsch (FT) catalysts that are highly active and selective. The effect of the cobalt crystal phase on product selectivity in FT synthesis is shown in Figure 7.

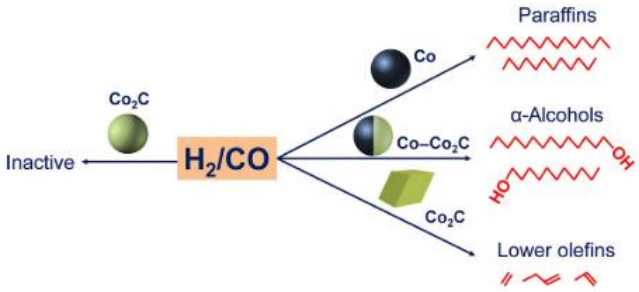

Figure 7. Effect of cobalt phase on product distribution in FT synthesis [24]

It is widely acknowledged that metallic cobalt particles serve as the active phase for CO hydrogenation in Fischer-Tropsch synthesis. However, it's common to observe cobalt carbides, cobalt oxides, and composite compounds containing cobalt in operational FT catalysts [24]. Metallic cobalt can exist in different crystalline forms which are α-Co (hcp) and β-Co (fcc). The size of cobalt nanoparticles has an impact on both the crystal phase and the accessibility of surface sites under reaction conditions [40]. It was reported that cobalt nanoparticles below 20 nm consist of pure fcc phase whereas above 40 nm cobalt nanoparticles consist of purely hcp phase [40].

The variation in catalytic rates based on particle size arises from alterations in the density of crystal planes exposed on the nanoparticle surface as the size changes. During FT synthesis, cobalt nanoparticles are present in the low nanometer range (1-50 nm). Under 100 nm, fcc cobalt was reported to be the most stable phase in cobalt nanoparticles [39]. Helden et al. reported (Figure 8) on the effect of cobalt nanoparticle size on TOF [39]. It was found that the highest TOF was achieved between the 5-10 nm region where there was a rapid drop in TOF above 10 nm. The effect of Co particle size was negligible when the particle size was larger than 10 nm. Moreover, as the cobalt particle size increased up to a critical point, the selectivity for methane decreased while the production of C_{5+} hydrocarbons increased [24].

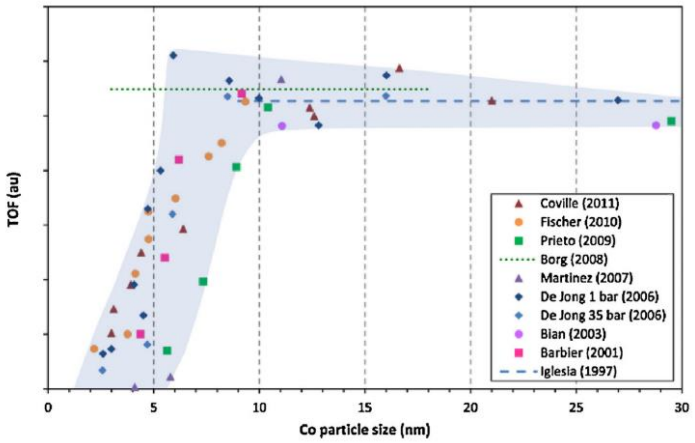

Figure 8. Effect of cobalt particle size on TOF in FT synthesis [39]

Cobalt nanoparticles consist of different facets that show different selectivity and activity for FT synthesis as shown by experimental and computational studies [41,42]. Helden et al. also revealed that facet density on cobalt nanoparticles is directly affected by the cobalt particle size [39]. Figure 9 represents how the density of different facets of cobalt nanoparticle changes with increasing particle size. Since the activity of FT synthesis is facet-dependent, the optimization of the facet density on cobalt nanoparticle is essential to achieve high activity and selectivity. Nie et al. studied the effect of hcp(10-11), hcp(10-10) and fcc(111) facets on FTS activity and selectivity and their results showed that exposed facets not only affect the activity but also the product selectivity [41]. The highest CO conversion was achieved on fcc(111) surface compared to hcp facets. Qin et al. also investigated the effect of (112), (111) and (001) facets of Co nanoparticle on FTS activity and selectivity [42]. Qin et al. found that CO conversion rate of facets follows the order of (001) > (112) > (111) whereas the C_{5+} selectivity follows the order of (112) > (111) > (001). The main reason for different activity and selectivity values resulting in different facets lies within the ability of a facet to dissociate CO. Recent studies have revealed that stepped surfaces are more active for CO dissociation than flat surfaces on cobalt which results in higher catalyst activity and selectivity towards heavier hydrocarbons [43].

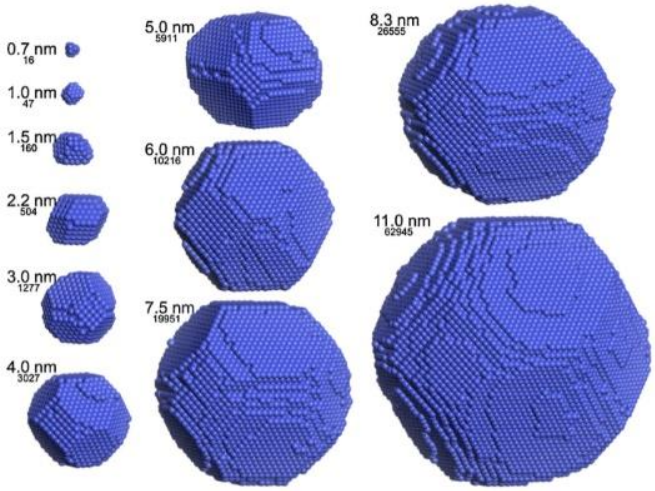

Figure 9. Effect of cobalt particle size on facet density [39]

The conversion of active Co^0 to cobalt oxides and cobalt carbides can occur due to interactions with the catalyst supports or reaction conditions [40]. The formation of cobalt oxide (Co_3O_4) due to oxidation by water has been suggested as a possible cause of catalyst deactivation. Surface oxidation is observed under conditions of high CO conversion and elevated reaction temperatures [40]. Additionally, research has indicated that smaller cobalt particles are more susceptible to surface oxidation compared to larger particles [40]. Small metallic cobalt nanoparticles can readily undergo re-oxidation to form cobalt oxide during Fischer-Tropsch synthesis.

Cobalt carbide (Co_2C) formation was believed to be one of the reasons for catalyst deactivation in the earlier studies and Co_2C formation was thought to be unlikely as the rate of carbon diffusion over Co to form carbides is very low. However, recent studies revealed that alkali addition can stabilize carbide formation during FTS [35]. Additionally, the presence of both Co^0 and Co_2C phases were found to create a dual active site for higher alcohol synthesis [44].

2.5 Computational Catalyst Design and Surface Science Approaches

Impact of catalysts on society is tremendous as it effects many modern life activities from chemical synthesis and environmental protection to energy production [45]. Therefore, optimization and discovery of new catalysts are key to develop industries with more efficiency while achieving global sustainability goals.

In the field of heterogeneous catalysis, surface science serves as a vital tool for understanding and optimizing catalyst materials and their interactions with reactants [46]. All catalytic reactions occur on catalyst surface hence understanding this interface where reactants adsorb, react, and desorb possess a great importance to understand catalytic reactions and design more active and selective catalysts. By using the power of surface science, researchers can investigate and characterize the structural, electronic, and chemical properties of catalyst surfaces at the atomic and molecular scale.

Even though surface science allows scientists to manipulate catalyst properties with atomic precision, designing new catalysts is a resourceful process. Therefore, computational catalyst design has gained emerging importance due to significant advances in computer power and computational methods. To illustrate the power of current computational tools, calculation of the transition state for the Diels–Alder reaction required six months of computational time in the 1980s. The same calculation took 3.3 seconds in 2021 [47].

Computational catalyst design offers extraordinary capabilities that enhance our understanding of catalysis and drive the development of more efficient and sustainable catalytic materials [46]. By modeling catalysts at the atomic and molecular scales, scientists can gain insights into key parameters like adsorption energies, reaction pathways, and reaction kinetics. Such a granular level of insight is often exceedingly challenging to attain using experimental methods alone. Furthermore, the manipulation of parameters like catalyst composition, crystal structure, and active site geometry empowers researchers to carefully adjust catalysts, tailoring them for optimal performance in specific reactions. This level of control allows for the creation of catalysts that are not only highly active but also selective and stable, essential attributes for practical applications in industrial processes and environmental remediation.

Computational catalyst design is not only valuable for reducing time and cost but is also a critical and evolving research field. It complements experimental efforts by inspiring new directions and facilitating rapid catalyst screening. Additionally, it offers experimentally testable hypotheses that can guide further research. By integrating computational design with experimental techniques, researchers can rapidly screen catalysts for catalyst development and innovation.

2.6 Objectives of the Study

Co-based catalysts are highly used in FT-synthesis due their high activity, high selectivity to heavier hydrocarbons and thermal/chemical properties. Alkali addition to Co-based catalysts provided promising results to obtain hydrocarbons with increased olefin content for FT-synthesis. However, in the literature, there are conflictive arguments about the effects of alkali promoters.

Due to weakened C-O bond, experimental studies expected CO dissociation rate to be increased with alkali addition. However, there are no experimental or computational studies that show alkali promotion results in increased CO dissociation rate on cobalt catalysts. In addition, the mechanism related to CO dissociation behavior remains unknown. Furthermore, experimental studies reported different activity and selectivity values for different alkalis but the fundamental reason for this varying effect is still unexplained.

In order to explain the conflictive arguments regarding the effects of different alkali promoters and CO dissociation mechanisms, a Density Functional Theory study is performed to analyze the effect of alkali promoters (Li, Na, K) on the adsorption and dissociation behavior of CO on the Co(111) surface and aimed to answer the following questions:

- What are the effect of alkali promoters on CO adsorption and dissociation on Co(111) surface?
- What is the effect of alkali coverage on FTS adsorbates?
- What are the effect of alkali promoters on cobalt carbide formation?

CHAPTER 3

LITERATURE SURVEY

3.1 Effect of Alkali Promoters on Heavy Hydrocarbon and Olefin Selectivity

Compared to Fe-based FT catalysts, Co-based FT catalysts predominantly yield long chain (heavy) linear paraffins, with fewer olefins and alcohols as products [48]. Experimental observations indicated that modification with an alkali promoter of the Co-based catalysts resulted in increased olefin content, which is proposed to be due to reduction of surface acidity and increase of CO adsorption energy [2,43,49]. Alkali promoters act as electronic and structural modifiers on cobalt catalysts to adjust the catalyst performance and selectivity by altering the surface chemistry and electronic properties of cobalt particles. Dai et al. reported that the olefin to paraffin ratio for Na promoted Co/SiO_2 catalyst was nearly four times higher compared to the unpromoted catalyst (Figure 10) [50]. Osa et al. performed a study to understand the effect of the addition of alkali metal and alkali-earth metal promoters on cobalt-based catalysts on FTS activity and on hydrocarbon product distribution [2]. Their results reported that C_{15}-C_{18} hydrocarbon selectivity for Co/Al_2O_3 catalyst improved from 6.6% to 21.5% and 26.2% for Na and K promoted Co catalysts, respectively. Increased heavier hydrocarbon selectivity upon alkali addition was attributed to increase in cobalt particle size due to an increase in the basicity. Li et al. showed that when alkali promoters were added on CoMn catalyst, the activity of FTS follows the order of Li > Na > K > Rb whereas the highest C_{5+} selectivity (%37.6) was achieved with Na [33]. Also, it was found that with each alkali addition, the olefin to paraffin ratio increased, especially for Na and K promoted surfaces.

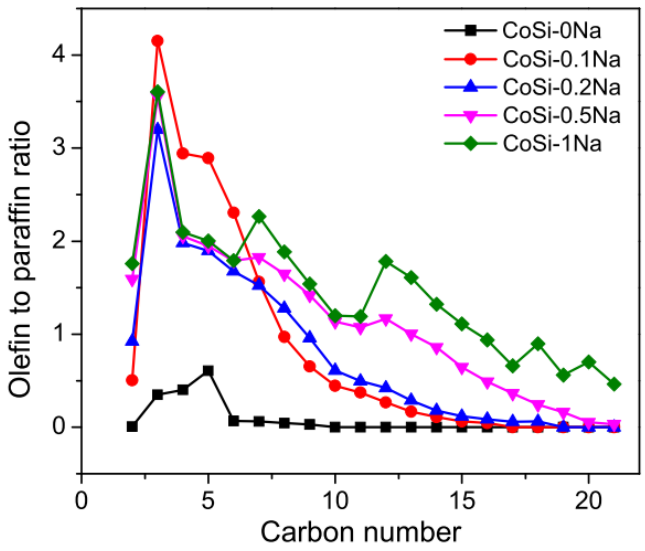

Figure 10. Olefin to paraffin ratio on Co/SiO_2 catalyst with different Na loadings [50]

Alkali promoters were also reported to be beneficial for the stabilization of active phases for FTS. Huo et al. studied the effect of K_2O promoter on iron-based FTS catalysts. Their results indicated that K_2O can stabilize more active facets during catalyst synthesis such as Fe(211) [51]. The presence of the alkali promoter also promotes the formation of small particles with significantly higher density of active facets.

Density functional theory (DFT) calculations have been performed in the literature to explore the effects of different alkali promoters on the FTS activity and selectivity on Co and other transition metals. Zhang et al. investigated the effect of potassium on carbon adsorption on the Co(0001) surface [34]. It was found that the presence of potassium on the surface increases the adsorption energy of the adsorbed species under any coverage. Additionally, the presence of potassium enhances the stability of carbon adsorption configurations. Yang et al. investigated the interaction of alkali metals (Li, Na, K, Rb, and Cs) with Fe_3O_4(111) surface [52]. Their results indicated the electron transfer capacity of alkali promoters follows the order of Li < Na < K ≈ Rb ≈ Cs. They also analyzed their mobility on Fe_3O_4(111) surface and found that alkali metals have simple migration ability on the Fe_3O_4(111) surface since the calculated activation barriers are highly insignificant.

Although there is a common denominator that alkali promoters increase the olefin selectivity, there are conflicts in the literature on the effects of different alkalis. Yu et al. studied the effect of different alkali promoters (Li, Na, K, Rb, and Cs) on Ru-based FTS catalysts and revealed that high electronegative alkali metals (Li and Na) show higher selectivity to lower olefins ($C_{2-4=}$) whereas lower electronegative alkali metals (K, Rb, Cs) give higher selectivity to long-chain α-olefins ($C_{5+=}$) (Figure 11a) [53]. Yu et al. also showed that CO conversion rate varies for different alkalis (Figure 11b). CO conversion rate follows the following order of Li > Na > K > Rb > Cs. Contrary, Owen et al. performed a study on Li, Na and K promoters on Co-based FTS catalysts found that Na promoted catalyst showed the highest C_{5+} selectivity whereas K promoted catalyst gave the highest C_2-C_4 selectivity [1]. Li et al. studied the effect of different alkali promoters (Li, Na, K, Rb and Cs) on iron-based FTS catalysts and achieved the highest C_{5+} selectivity (46.1%) with K promoted catalyst [54]. Osa et al. also investigated the effect of alkali promoters on Co-based catalysts and found that Na promotion results in higher olefin ratio compared to K promoted system (Figure 11c) [2].

Recently, Jeske and Kizilkaya et al. studied the effect of different alkali promoters (Na, K, Cs) on $CoRu/Al_2O_3$ catalyst on a combined experimental and computational study [43]. Their study showed that at 1.0 M_{at}/nm^2 alkali coverage, CTY decreases with increasing cation size and decreasing electronegativity of alkali promoters. Additionally, alkali promoters decreased the chain growth ability in the order of Cs > Na > K compared to unpromoted counterpart. Moreover, their study showed that there were no distinguishable differences between different alkali promoters in C_5-C_{10} olefin selectivity whereas the selectivity values were found as %56.2, %57.2 and %54.2 for Na, K and Cs promoted catalysts, respectively. The addition of alkali promoters also increased WGSR activity in the order of Cs > K > Na. Especially, when the Na loading is changed from 1.0 to 3.0 M_{at}/nm^2 , CO_2 selectivity significantly increased from %1.0 to %8.1. The computational part of the work of Jeske and Kizilkaya et al. also revealed important factors to understand the promotional effects of alkali promoters. Firstly, they found that adsorption of alkali promoters were energetically more feasible on stepped surfaces compared to flat surfaces. Also, they revealed that alkali addition increases CO adsorption energy but has little or no effect on the H adsorption energy. Finally, their study on the electronic behavior of the system showed that alkali addition enhances the electron back-donation from cobalt atoms to CO* which causes an additional charge

accumulation on CO*. In our work, emphasis was placed on identifying the fundamental reason for the different behavior of alkali promoters observed in experimental studies.

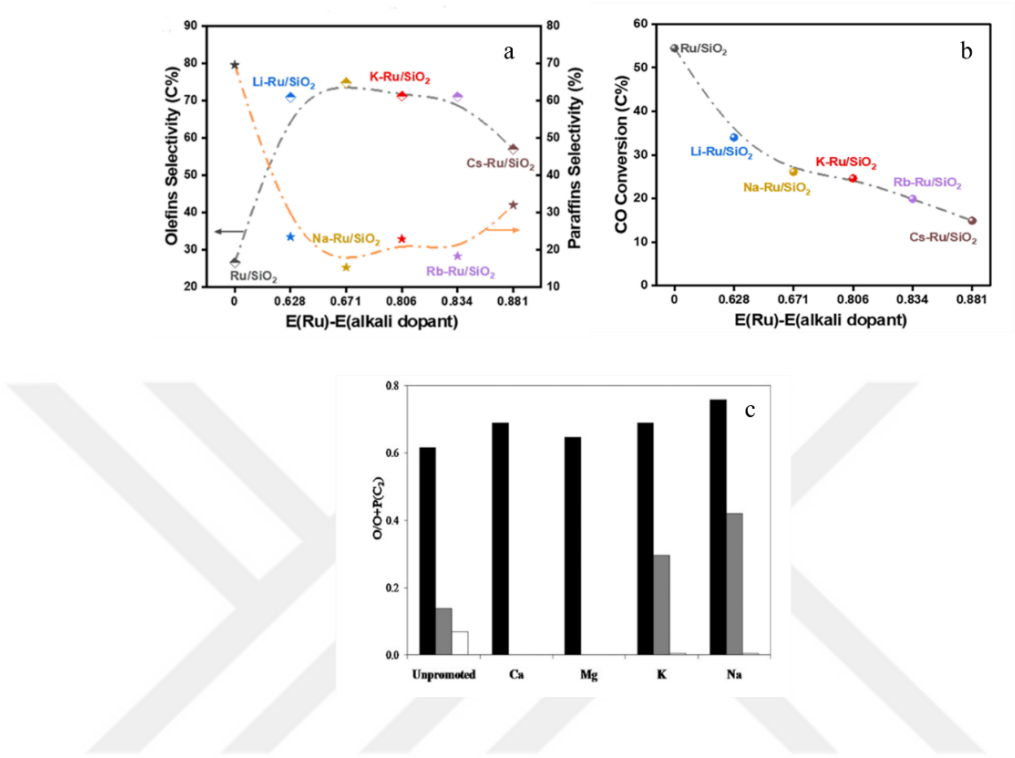

Figure 11. Effect of different alkali promoters on a) olefin to paraffin ratio and b) CO conversion by work of Yu et al. [53] c) effect of alkali and alkali earth metals on olefin selectivity by work of Osa et al. [2]

3.2 Effect of Alkali Coverage on FTS Adsorbates

Coverage of alkali promoters on metal surfaces have a significant effect on the FTS reactants since the alkali metal ions interact with the catalyst surface, modify its electronic properties, and promote the activation of CO and H_2. Jeske and Kizilkaya et al. reported that alkali coverages above 0.25 ML on Co(111) surface results in either CO desorption to the gas phase or decomposition of the promoter structures [43]. Jeske and Kizilkaya et al. also found that decreasing alkali coverage results in increased alkali adsorption energy (Figure 12) for both Co(111) and Co(211) surfaces. They found that low basic promoter coverage (< 1 atom/nm^2) is necessary to maintain low CH_4 and CO_2

selectivity. Additionally, low promoter surface coverages on cobalt were found to be sufficient to reduce CO hydrogenation activity. Chen et al. studied the effect of K coverages ranging from 0.040 ML to 0.126 ML on Co(0001), Co(10-11) and Co(10-12) facets [55]. Their results revealed that, the adsorption energy of the promoter decreases with increasing coverage on all surfaces. Han et al. investigated the effect of K coverage on $Mo_2C(001)$ surface and showed a notable dependence on coverage, primarily due to the substantial repulsive interactions stemming from the dipole moment of adsorbed K [56]. The study of Yang et al. on the coverage effect of alkali metals (Li, Na, K, Rb and Cs) on $Fe_3O_4(111)$ surface revealed that the promoting effect of alkali metals does not improve with an increase in the quantity of alkali metal present which indicates that there is an optimum promoter coverage for alkali metals [52].

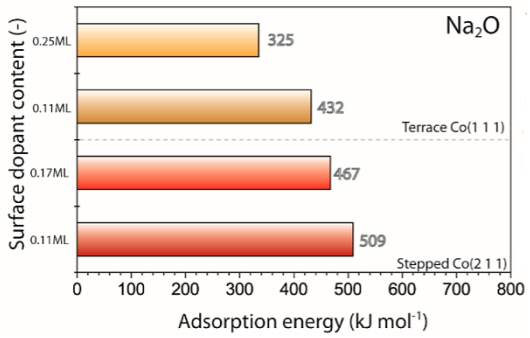

Figure 12. Effect of alkali coverage on alkali adsorption energy on Co(111) and Co(211) surfaces [43]

The study of Politano et al. on the effect of alkali promoter coverage on CO dissociation on Cu(111) and Ni(111) surfaces revealed that alkali coverage dependence of CO dissociation varies between different transition metals [57]. On the Cu(111) promoted surface, CO dissociation occurs regardless of the alkali coverage, yet the Ni(111) surface requires a threshold alkali coverage for CO dissociation. Liu et al. investigated the effect of K promotion on Rh(111) surface and found that K promotion in CO dissociation on the Rh(111) surface is significantly influenced by the distance between the potassium and the CO molecule undergoing dissociation [58]. If the distance between K and the dissociating CO is short (2-3 Å), ionic interactions are observed between the alkali promoter and metal which result in direct K-O bonding. The ionic

interaction between metal and alkali promoter greatly stabilizes O at the transition state and reduces the CO dissociation barrier. However, if the distance is above 3 Å, there is only electrostatic interaction between the alkali promoter and CO.

3.3 Effect of Alkali Promoters on Cobalt Carbide Formation

It is known that due to CO dissociation, there will be carbon accumulation on Co surface during FT synthesis. Excessive C content on Co(111) surface may result in carbonaceous deposits on the catalyst surface, which can lead to catalyst poisoning and reduced activity or promote the cobalt carbide formation. As stated in the previous sections, the possibility of formation of cobalt carbides is low in FT synthesis conditions. However, alkali addition may also cause cobalt carbide (Co_2C) formation by stabilizing the Co_2C phase during FTS process [33,35,50] which can promote the unwanted water–gas shift reaction (WGSR). Electron donor characteristics of alkali promoters on Co(111) surface can alter the surface chemistry and make the surface more carbophilic which promotes the carbide formation [43]. Dai et al. studied the effect of Na addition on cobalt formation. Their results indicated that as the Na loading increases pure hcp and fcc cobalt phases disappear due to Co_2C formation (Figure 13). Zhang et al. investigated the effect of alkali promoters on cobalt carbide formation and found that K_2O coverage strongly affects the Co_2C formation and Co_2C crystal morphology [35]. Figure 14 represents how alkali coverage changes the Co_2C crystal morphology. The higher K_2O coverages results in higher surface energy drops and the surface energy reduction rates of most C terminated surfaces were found to be higher than those of the Co-terminated surfaces [35].

Jeske and Kizilkaya et al. reported that alkali oxide addition results in enhanced WGSR activity (up to 8%) on CoRu/γ-Al_2O_3 catalyst [43]. Presence of both Co^0 and Co_2C phases were also found to create a dual active site for higher alcohols which reduces the hydrocarbon selectivity [44]. DFT study of Pei et al. revealed that Co_2C serves as the active site for non-dissociative adsorption of CO [44]. On the other hand, metallic cobalt functions as the active site for the dissociative adsorption of CO and facilitates the subsequent growth of carbon chains, thus promoting the formation of alcohols.

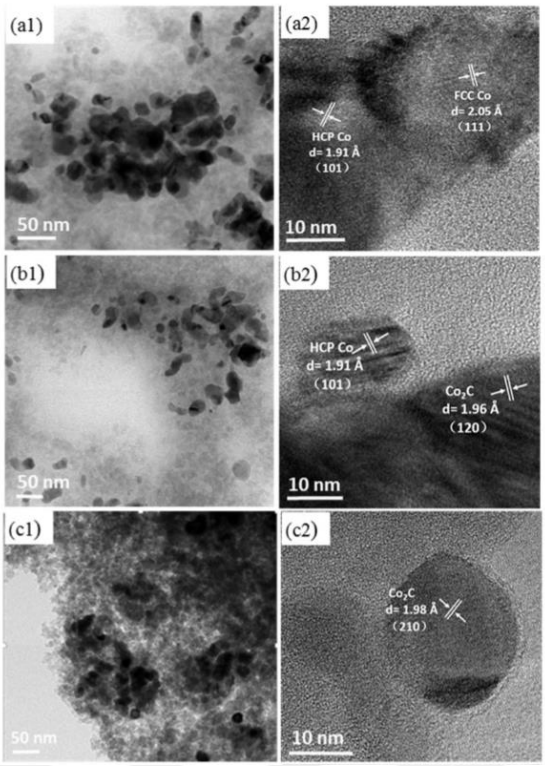

Figure 13. TEM images of cobalt catalysts at various Na loadings. a:Co/SiO_2-0Na; b: Co/SiO_2-0.1Na; c: Co/SiO_2. Adapted from the work of Dai et al [50]

Helden et al. investigated the effect of surface carbon concentration on clean Co(111) surface and revealed that as the carbon coverage increases, due to strong lateral repulsions, subsurface carbon geometries exhibit increased stability compared to having all the carbon atoms located on the surface [59]. However, carbon migration into the subsurface layer is not plausible without the presence of an appropriate kinetic pathway on the Co(111) surface. Therefore, reconstruction of cobalt surface is more anticipated. In the literature, it has been shown that there is a strong likelihood of carbon reconstruction on the Co(111) surface above 0.50 ML carbon coverages [60]. Presence of atoms in the lattice can significantly affect the adsorption characteristics of molecules and subsequent reactions. Zonnevylle et al. investigated the effect of subsurface carbon on Co(0001) surface and suggested that the presence of subsurface C decreases the backbonding capacity of Co metal which results in the reduction of CO adsorption and dissociation capacity [61].

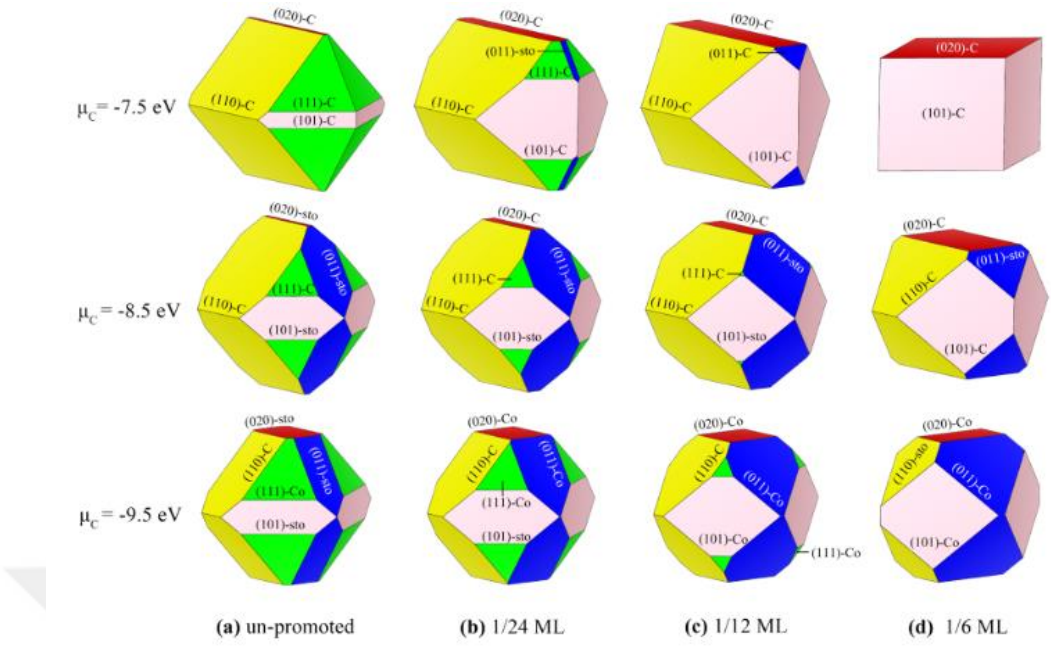

Figure 14. Equilibrium morphologies of Co_2C crystallites as a function of the K_2O coverage at (a) Unpromoted Co_2C, (b) 1/24 ML, (c) 1/12 ML, and (d) 1/6 ML [35]

3.4 Effect of Alkali Promoters on CO Dissociation and Effect of CO Coverage

CO dissociation is the first and rate-limiting step in Fischer-Tropsch synthesis to convert syngas into hydrocarbons. The C-O bond must be broken to generate intermediate species that will ultimately lead to the formation of hydrocarbons. The C-O bond scission is an energy demanding process where a significant amount of energy needs to be supplied to break the bond. Efficiency of the FT synthesis is therefore highly dependent on the CO dissociation mechanism. For the Co(111) surface, two mechanisms have been extensively discussed for CO dissociation which are direct and H-assisted CO dissociation [18]. Direct CO dissociation involves the breaking of the C-O bond directly on the cobalt surface, while H-assisted CO dissociation involves the assistance of a hydrogen atom in breaking the C-O bond.

In normal FT conditions, cobalt surface is mostly covered with CO where the coverage ranges from 0.6 ML to 1 ML [62]. CO coverage on a cobalt surface is crucial for FTS because it plays a significant role in determining the overall reaction kinetics and product selectivity during the FTS process. Zijlstra et al. studied the coverage effects in CO dissociation on low-reactive Co(0001) and high-reactive Co($11\bar{2}\bar{1}$) surfaces [62]. Their results indicate that higher CO coverage results in lower average CO adsorption energy where the saturation coverage was calculated as 0.6 ML for both surfaces. Step-edge sites were found to be highly active for CO dissociation at high coverages whereas on a terrace Co surface, a higher CO coverage leads to a higher activation barrier for CO dissociation. Therefore, H-assisted pathways are more preferred on terraces. Jeske and Kizilkaya et al. also reported that slight increase in CO coverage is sufficient to hinder dissociative H_2 adsorption by blocking available adsorption sites where lowered CO hydrogenation rates results in higher selectivity to olefins [43]. Therefore, CO coverage significantly affects the CO dissociation mechanism on cobalt surfaces and the activation of CO is a key factor to achieve desired end products in FTS. Experimental studies attribute the increased hydrocarbon selectivity with the addition of alkali promoters to the increase in the rate of CO dissociation [33,35,50]. However, up to our knowledge, there are no experimental or computational studies that show alkali promotion results in increased CO dissociation rate on cobalt catalysts.

Ma et al. investigated the effect of alkali metals (Li, Na and K) on co-adsorbed carbon monoxide on Co(0001) surface [63]. The introduction of alkali metal atoms significantly reinforced the stabilization of CO on the substrate surface. This presence also reduced the surface potential in the vicinity of the CO molecule and weakened the carbon-oxygen bond. Zhang et. al. performed a study to investigate the CO activation on the K_2O/Cu(111) surface (Figure 15) [32]. Their results showed that K_2O promotion makes direct dissociation of CO energetically favorable by decreasing the activation barrier by 2.50 eV. Also, the activation barrier of HCO formation decreases by 0.18 eV upon alkali addition.

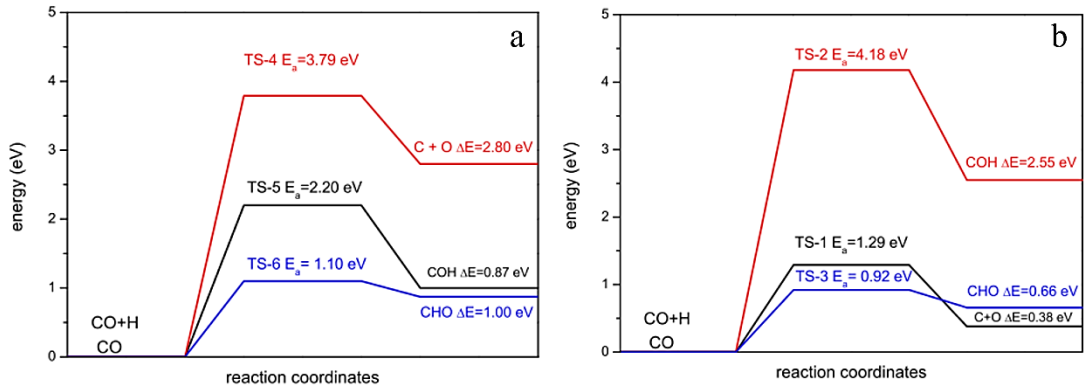

Figure 15. The direct and H-assisted dissociation routes of CO on a) Cu(111) and b) K_2O/Cu(111) surface [32]

CHAPTER 4

COMPUTATIONAL METHODOLOGY

4.1 Computational Tool

Spin-polarized Density Functional Theory (DFT) calculations were performed with Vienna Ab-Initio Simulation Package (VASP). VASP calculates an approximate solution to the many-body Schrödinger equation based on density functional theory (DFT).

In the VASP software, fundamental properties such as one-electron orbitals, electronic charge density, and the local potential are represented using plane wave basis sets. The electron-ion interactions are characterized through the utilization of norm-conserving or ultrasoft pseudopotentials, as well as the projector-augmented-wave method. In this study, the electron-ion interaction was modeled by the projector-augmented wave (PAW) method [64] and the exchange-correlation energy was calculated with the van der Waals (VdW) functional. VdW functional has been selected for this project because it accounts for long-range, non-local correlations that give rise to VdW forces (Keesom, Debye, London) which provides more accurate estimations of adsorption sites and energies, in particular for the adsorption of CO [65].

VASP requires 4 input files to run which are INCAR, POTCAR, KPOINTS and POSCAR files. After the calculations are completed, VASP generates various output files which contain information about various properties of the system such as energy, vibrations, charge density, atomic coordinates and etc. The content of input and output files of VASP are listed in Table 2.

Table 2. Input files required to run VASP and resulting output files

	File Name	Description
INPUT FILES	INCAR	The central input file in VASP serves as a directive to instruct the calculation on what tasks to perform and how to carry them out.
	POTCAR	This file contains the pseudopotential for each atomic species used in the calculation
	KPOINTS	This file specifies the Bloch vectors (k points) used to sample the Brillouin zone
	POSCAR	This file contains the lattice geometry and the positions of atoms within the crystal structure.
OUTPUT FILES	OUTCAR	The primary output file where various information can be found such as electronic steps, forces on atoms, magnetic moments and etc.
	CHGCAR	This file includes charge density information, lattice vectors, atomic coordinates, and one-center occupancies.
	CONTCAR	This file contains information about lattice geometry and position of atoms.
	OSZICAR	This file offers a concise summary of several critical results, including the selected self-consistent field (SCF) algorithm, convergence of total energy, charge and spin densities, free energies, and magnetic moments of the cell.
	XDATCAR	This file contains the updated positions of ions or atoms for each step in the ionic relaxation or dynamics calculation.
	DOSCAR	It contains the total and integrated DOS and optionally the local partial DOS.
	WAVECAR	It contains the wave function coefficients.

4.1.1 Density Functional Theory

In order to simultaneously capture the thermodynamic properties, electronic behavior and atomic structure of a system, the Schrödinger equation (Equation 4.1) needs to be solved. While the form of the Schrödinger equation is well-established, obtaining exact solutions for realistic systems containing multiple electrons is typically unattainable, primarily due to the challenges in modelling the exchange-correlation interactions between these electrons [66]. Considering the three spatial coordinates per electronic position, the Schrödinger equation becomes a 66-dimensional problem even

for a simple molecule like CO_2. Therefore, different approaches have been developed to overcome the complexity of Schrödinger equation. Among various approaches, density functional theory (DFT) has been the most widely used approach to solve the Schrödinger equation. Density functional theory has become the bedrock of computational catalysis since it offers best balance between accuracy and efficiency [66].

$$-\frac{\hbar^2}{2m}\nabla^2\Psi + V\Psi = E\Psi \tag{4.1}$$

In density functional theory, the one-body density is employed as the fundamental variable, as opposed to the many-body wave function. This approach enhances the feasibility of DFT, particularly when dealing with large systems [67]. Density functional theory is founded on the principles of the Hohenberg–Kohn and Kohn–Sham theorems. The Hohenberg-Kohn theorem provides the foundational theoretical framework for developing an effective single-particle approach. This approach allows for the calculation of the ground-state density and energy of systems containing interacting electrons. The resulting Kohn–Sham equations are the foundations of modern density-functional theory [67]. The central idea of the Kohn-Sham equation is to approximate the behavior of a system of interacting electrons by mapping it onto a system of non-interacting electrons with an effective potential. The Kohn-Sham equation aims to find the electronic density and energy of the system by solving for the wavefunctions and eigenvalues of these fictitious non-interacting electrons. The Kohn-Sham equation is given in Equation 4.2 where $v_{eff}(r)$, ε_i, and φ_i are local effective (fictitious) external potential, orbital energy of the corresponding Kohn–Sham orbital, and Kohn–Sham orbital, respectively.

$$\left(-\frac{\hbar^2}{2m}\nabla^2 + v_{eff}(r)\right)\varphi_i(r) = \varepsilon_i\varphi_i(r) \tag{4.2}$$

In DFT, most important energetic contributions are accounted for by the kinetic energy of a fictitious non-interacting system and electrostatic interactions of the electrons. The electronic energy that is not accounted for by the non-interacting kinetic and electrostatic terms is referred to as the exchange-correlation energy (E_{xc}). Exchange-correlation effects cannot be computed directly and must instead be approximated through computational methods. Numerous exchange–correlation density functionals have been developed over the years to obtain quantum mechanical systems with high accuracy. Figure 16 represents the Jacob's ladder of DFT functionals from the simplest form to more complex and high-accuracy functionals.

Functional methods in computational chemistry are broadly categorized as semi-empirical and non-empirical. Semi-empirical functionals use flexible electronic density forms with coefficients fitted to reference values from advanced quantum chemistry calculations or experimental data, such as the popular B3LYP functional [66]. Non-empirical functionals, on the other hand, derive their functional forms and parameters from the many-body Schrödinger equation, making them free from empirical parameters. An example of a widely used non-empirical functional is the Perdew-Burke-Ernzerhof (PBE) functional, particularly prominent in computational materials science [66].

The simplest functional model is based on the Hatree Fork theory where the exchange–correlation energy is considered as zero. In the case of the local density approximation (LDA), the exchange-correlation functional depends solely on the electronic density. However, the accuracy of LDA functional is lacking as LDA functionals tend to over-estimate the strength of the binding of molecules on the surface and shorter bond lengths [66]. Better accuracy generalized gradient approximation (GGA) is proposed which includes the dependence of the magnitude of the gradient of the electronic density [66]. Numerous GGA (B88, PW91, BLYP, and PBE) and meta-GGA (B88C, B95, Becke Roussel, and TPSS) exchange–correlation functionals have been developed in the literature [66]. Another category of approximations for the exchange-correlation energy is represented by hybrid functionals, which blend a portion of exact exchange with generalized gradient approximation (GGA) exchange. Hybrid functionals have proven to be highly effective in the field of quantum chemistry.

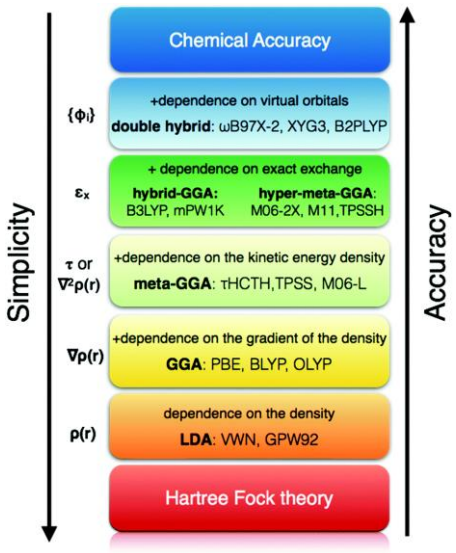

Figure 16. Jacob's ladder of DFT functionals [68]

The key advantage of DFT lies in its practical solvability for systems comprising approximately up to 100 atoms, as it demands comparatively lower computational resources per atom than other quantum mechanical methods [69]. DFT can accurately compute various chemical properties, including adsorption energies and geometries, adsorption structures, transition state geometries and energies, vibrational frequencies, and more. Even though DFT is an extremely powerful tool for computational catalyst design, one should always be aware of its limitations as the accuracy of density functional theory (DFT) relies on the thoughtful selection of the exchange-correlation functional.

4.2 Modelling Approaches in Computational Catalysis

As mentioned in previous section, due to its high computational cost, DFT calculations are limited to systems with several atoms, typically below 100. Therefore, different atomistic models are used to define a system which will represent the whole

nanoparticle. Two most common methods used in computational catalyst design are cluster and slab models which are demonstrated in Figure 17.

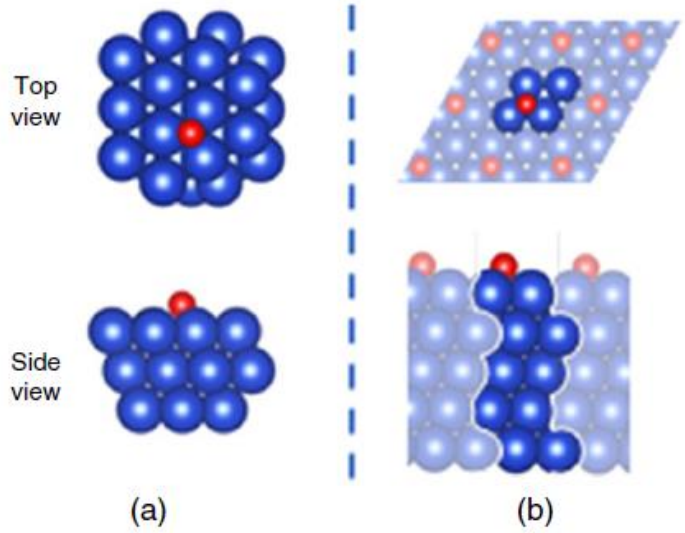

Figure 17. Visual representation of a) cluster and b) slab models [70]

A cluster model involves selecting a specific group of atoms or molecules from a larger system and studying their properties and interactions in isolation, without considering the surrounding environment. Cluster models are particularly useful for investigating the local properties and reactivity of a specific region within a larger system. Cluster models are valuable for reducing the computational complexity of simulations, making it more feasible to perform calculations that would be computationally expensive or time-consuming for the entire system [70]. However, it's important to note that cluster models have limitations, as they may not accurately capture the influence of the surrounding environment or long-range effects on the properties being studied.

A slab model is a representation of a crystalline surface or interface. It involves creating a finite, repeating unit of a crystal structure, often composed of atoms or molecules arranged in layers, and studying the properties and interactions of this surface region. Slab models are used to simulate the behavior of surfaces and interfaces in various materials, including metals, semiconductors, and insulators. Slab models are

valuable for studying surface properties, adsorption processes, and reactions occurring at the surfaces of materials [71]. Unlike cluster models that focus on a specific group of atoms or molecules, slab models provide a more realistic representation of a surface by considering the interactions between surface atoms and their neighboring atoms within the bulk material.

For large metal nanoparticles exceeding 5 nm in size, periodic slab models provide excellent approximations [71]. These models effectively capture the delocalized electronic structure of metals and the relatively flat local curvature of larger nanoparticles. Consequently, slab models have become a prominent choice for simulating heterogeneous catalysts. Slab models provide a more realistic representation of the surfaces of catalyst materials, capturing the atomic and molecular arrangements at the catalyst's active sites [71]. They offer valuable insights into the mechanisms of catalytic reactions, aiding in the development of efficient and sustainable catalysts for a wide range of chemical processes and applications. Based on the advantages listed above, a slab model was selected for this project to represent the Co nanoparticle as adsorption sites and CO dissociation mechanism needs to be studied on the surface.

4.2.1 Surface Model

Fcc cobalt was reported to be the most stable phase in cobalt nanoparticles below 100 nm [39]. Fcc Co nanoparticles tend to favor a regular truncated octahedral shape and these nanoparticles predominantly expose close-packed (111) terraces and step-edges (Figure 18a). According to Wulff construction, (111) facet (terrace) is the most favorable facet on fcc-Co [41]. Helden et al. showed that with increasing size of Co nanoparticle from 1 nm to 8 nm, the terrace site fraction decreases from 100% to 65% but it is still the highest facet fraction on Co nanoparticles under relevant FTS conditions (Figure 18b) [39].

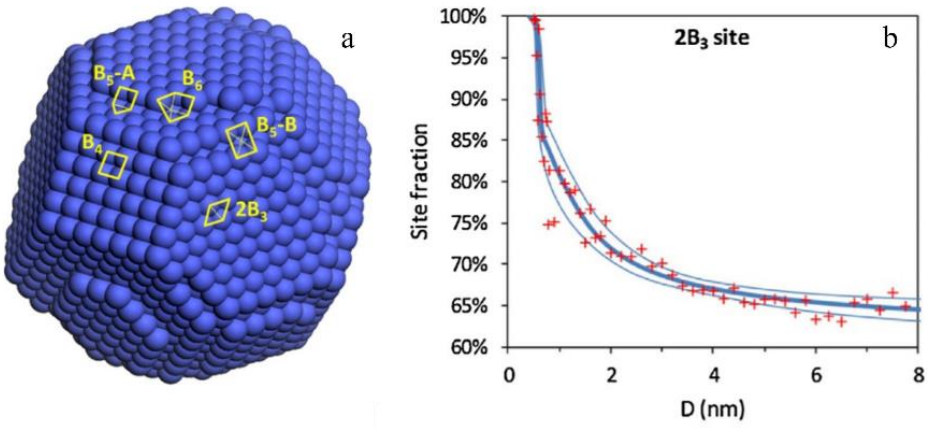

Figure 18. a) Different facets on cobalt nanoparticle and b) Effect of cobalt particle size on surface fraction of 2B3 (terrace site) [39]

In addition to being the most abundant facet on the surface, Co(111) facet was reported to be active for the FTS reaction. Nie et al. studied the effect of hcp(10-11), hcp(10-10) and fcc(111) facets on FTS activity and selectivity and their results showed that highest CO conversion was achieved on fcc(111) surface compared to hcp facets [41]. Qin et al. also investigated the effect of (112), (111) and (001) facets of Co nanoparticle on FTS activity and selectivity [42]. Qin et al. found that (111) facet showed a CO conversion value of 37.2% and C_{5+} selectivity value of 57.5%. Since the cobalt nanoparticle surface is mostly occupied by (111) facet and it is active towards FTS, the primary emphasis of this study was directed towards examining the Co(111) surface.

4.3 Bulk Optimization

A bulk system is a representation of a material or substance that is not affected by its surface characteristics. Bulk optimization in DFT includes volume relaxation, ENCUT optimization, and KPOINT optimization. Volume relaxation involves finding the geometry with the lowest energy and determining the lattice constant. The surfaces were cut from a bulk fcc-Co structure with an optimized lattice parameter of 3.56 Å.

In the Materials Studio software program, a p(3x3) surface was generated by specifying the lattice constant and entering the space group. Bulk contains 9 cobalt

atoms in each layer with a total of 4 layers. Top and side views of the optimized p(3x3) Co(111) surface is represented in Figure 19. To prevent coupling between consecutive slabs in the z-direction, a minimum vacuum height of 10 Å was included.

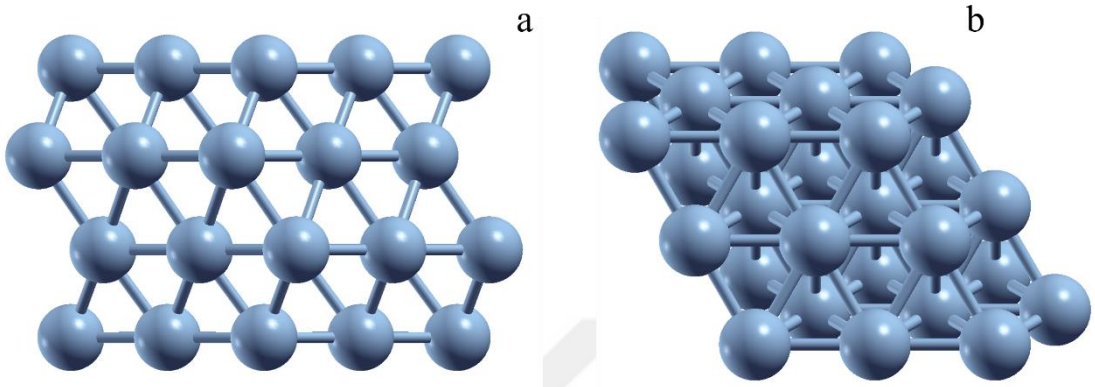

Figure 19. a) Side view and b) Top view of modelled p(3x3) Co(111) surface

The ENCUT value represents the maximum kinetic energy cutoff for the plane waves used to expand the electronic wavefunctions in the DFT calculations. A higher ENCUT value includes more plane waves in the calculation, which can lead to more accurate results but also increases the computational cost. Conversely, a lower ENCUT value reduces the computational cost but may sacrifice accuracy. ENCUT optimization was performed to determine the optimum ENCUT value which was found as 500 eV.

The reciprocal space was sampled with (3x3x1) k-points grid for p(3x3)-Co(111) by using Monkhorst-Pack method [16,72]. During the optimization of promoters and adsorbates, atoms located in the bottom half of the slabs in the z-direction were kept fixed at their pre-optimized positions. Meanwhile, all other atoms were allowed to relax and adjust their positions. The optimization of the structural models continued until the forces acting on the atoms reached a magnitude smaller than 0.01 eV/Å. Additionally, dipole corrections were applied in the z-direction for all optimization steps.

4.4 Clean Surface and Gas Phase Optimizations

Before studying adsorption of FTS adsorbates and analyzing CO dissociation reactions, firstly the Co(111) surface needs to be optimized for accurate results. The use of accurate input files and input commands is crucial for obtaining precise and reliable results in computational simulations and calculations. A sample INCAR file for surface optimization and explanation of input commands are given in Table 3.

Table 3. INCAR file for clean surface optimization

TAGS	DEFINITION
NPAR = 4	determines the number of parallel jobs
ALGO = Fast	specifies the electronic minimization algorithm
ISTART = 1	determines whether or not to read the WAVECAR file
IDIPOL = 3	switches on dipole corrections to the total energy
LDIPOL = .TRUE.	switches on corrections to the potential and forces in VASP
EDIFFG = -0.02	defines the break condition for the ionic relaxation loop
ISPIN = 2	specifies spin polarization
ICHARG = 1	determines how VASP constructs the initial charge density
MAGMOM = 36*3 1*0	specifies the initial magnetic moment for each atom
IBRION = 2	determines how the ions are updated and moved
ENCUT = 600	specifies the cutoff energy for the plane-wave-basis set
ISMEAR = 1	determines how the partial occupancies f_{nk} are set for each orbital
SIGMA = 0.2	specifies the width of the smearing
NSW = 999	sets the maximum number of ionic steps
LREAL = AUTO	determines whether the projection operators are evaluated in real-space or in reciprocal space
GGA = RE	Tags for VDW Functional
LUSE_VDW = .TRUE.	
AGGAC = 0.0000	
LASPH = .TRUE.	

Molecule optimization involves calculating the energy of a molecule in the gas phase while iteratively adjusting its structure to find the most energetically favorable configuration. Gas phase energies are used for the calculation of the adsorption energy for the molecules on adsorbed surfaces.

4.5 Adsorption Energy Calculations

On clean Co(111) surface, there are 4 different adsorption sites that atoms and molecules can adsorb which are represented in Figure 20.

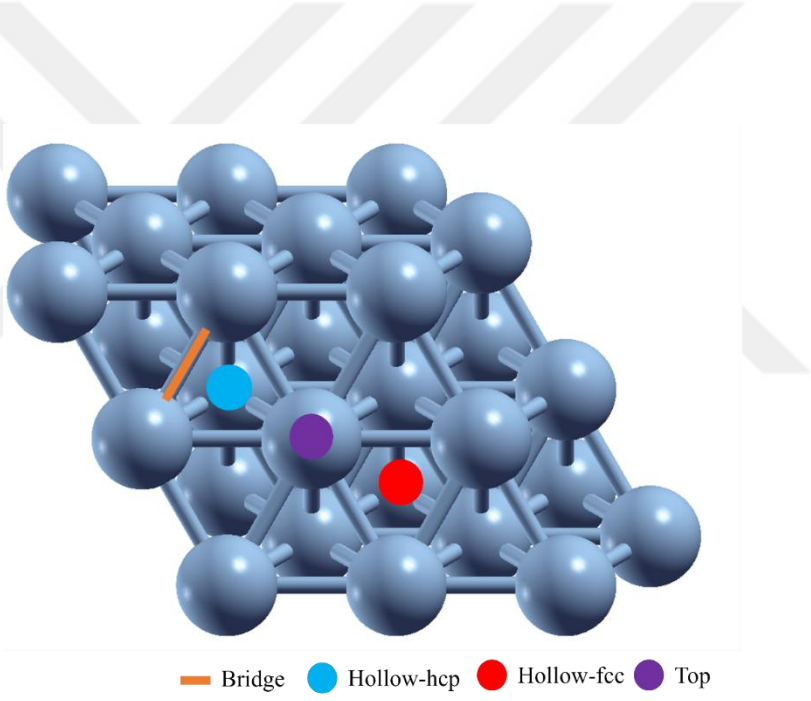

Figure 20. Different adsorption sites on Co(111) surface

The adsorption energy is calculated as the energy difference between the total energy of the adsorbate-surface system and the sum of the energies of the isolated adsorbate and the clean, unoccupied surface. The adsorption energy equation which was used to measure the strength of adsorbent substrate adsorption are defined in Equation 4.3 where E_{sub}, E_{mol}, and $E_{mol/sub}$ are total energies of substrate, total energies of free

adsorbent, and total energy of adsorbent substrate system in its equilibrium state, respectively.

$$E_{ads} = E_{sub} + E_{mol} - E_{mol/sub} \quad (4.3)$$

4.6 Calculations Related to Vibrational Frequencies of Adsorbates and Electronic Charge

Vibrational frequency analyses are performed to analyze the effect of promoter addition on the C-O bond strength. It has long been known qualitatively that, shorter bond lengths lead to higher force constants and higher vibrational frequencies, while longer bond lengths result in lower force constants and lower vibrational frequencies.

Bader charge analysis [73–75] was performed to investigate changes in electronic charge on cobalt and adsorbates as a result of the deposition of various alkali promoters (Li_2O, Na_2O, K_2O) on Co(111) surface. Henkelman et al. have developed an algorithm for calculating the electronic charges on individual atoms in molecules or crystals based on the Bader partitioning scheme [75]. This approach relies solely on the electron density and determines the partitioning based on zero-flux surfaces.

4.7 Transition State Calculations

Henry Eyring developed the transition state theory in 1935 as an alternative to the previously employed Arrhenius equation and collision theory to explain chemical reactions [76]. According to transition state theory (TST), there exists an intermediate state known as the transition state situated between the initial state composed of reactant molecules and the final state comprising product molecules. In the transition state, the reactants are combined in a species called as activated complex which is formed at

maximum energy. For a reaction to proceed, this maximum energy point, which is also referred as activation barrier, needs to be overcome. After surpassing the energy barrier, the reaction is able to proceed and product formation occurs.

The transition state theory holds crucial importance in surface science and catalysis. It enables the comprehension of reaction mechanisms on catalytic surfaces, facilitating the design and optimization of catalysts, prediction of reaction kinetics, control of selectivity, and understanding catalyst deactivation processes. TST also aids in quantifying surface coverage, and its application in computational chemistry allows for accurate modeling of surface reactions, offering valuable insights into a wide range of industries, including the chemical, petrochemical, pharmaceutical, and environmental sectors.

Numerous transition state research techniques can be found in the scientific literature. For example, if the only known variable is the initial state, the dimer method is the most appropriate method which is available in softwares such as VASP [77]. Methods like Conjugate Peak Refinement (CPR) and the Ridge method have been developed for identifying fluid phase transition states and energy barriers. These methods are incorporated into software programs like CHARMM [69]. However, when both the initial and final states are defined, the Nudged Elastic Band (NEB) method is the most commonly used approach which is applicable in VASP, CASTEP, GPAW and Quantum Espresso [69].

4.7.1 Nudged Elastic Band (NEB) Method

The Nudged Elastic Band (NEB) method is a widely used computational technique for studying the minimum energy path (MEP) or transition state of a chemical or physical process [69]. NEB introduces a set of "images" or intermediate states between the initial and final states. These images represent the pathway that connects the two states (Figure 21). Each image seeks to attain the lowest energy possible while preserving equal spacing from neighboring images. An imaginary spring-like "elastic band" connects the images. The images are moved along this band in such a way that they converge toward the minimum energy path.

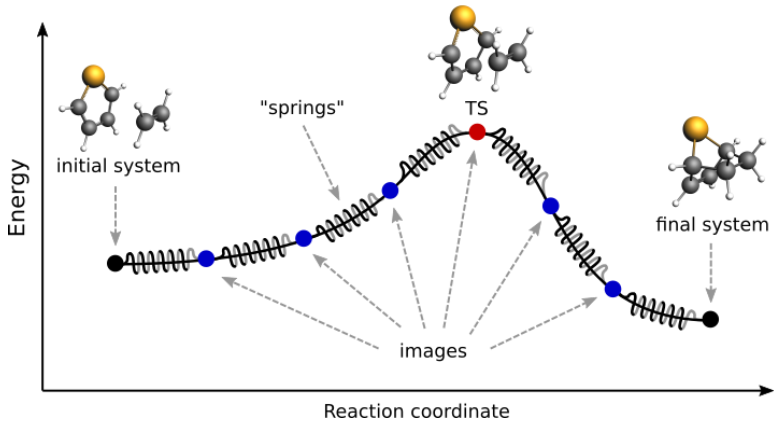

Figure 21. Visual representation of reaction pathway with NEB [78]

In the initial stage of a NEB calculation, the geometries of both the initial and final systems are optimized to minimize their energy. Subsequently, a preliminary approximation of the reaction pathway is constructed by generating a series of intermediate images through linear interpolation between the initial and final systems. Ultimately, the reaction path is determined by carrying out a simultaneous optimization of all the images. In the NEB method, the images are not independent from each other. The forces acting on each image depend on their neighboring images. During each step of the optimization, the forces parallel to the reaction path are eliminated, and a spring force is introduced to keep each image positioned between its neighboring images. This process guides the images to converge toward the minimum energy pathway connecting the initial and final states. This prevents the images from sliding toward either the initial or final reaction states and ensures their even distribution along the reaction path. Within the NEB path optimization, a climbing image algorithm is employed to guide the highest-energy image toward the transition state [79]. This specific image experiences a modification in which it no longer responds to the spring forces along the pathway. Instead, the true force acting on this image along the tangent is reversed, causing the image to maximize its energy along the path while minimizing it in all other directions, ultimately converging precisely at the saddle point. All TS candidates obtained by CI-NEB[79] calculations are further confirmed to as the actual transition states, based on having a single imaginary vibrational mode.

CHAPTER 5

RESULTS AND DISCUSSION

5.1 Effect of Alkali Promoters on the Adsorption of the Reactants and Intermediates of FTS on Co(111)

5.1.1 Adsorption of Oxidic Promoters (Li_2O, Na_2O and K_2O) on Co(111) surface

This project aims to analyze the effect of alkali promoters on CO adsorption and dissociation on the Co(111) surface. In order to understand the effect of alkali promoters, firstly the adsorption of oxidic promoters (Li_2O, Na_2O and K_2O) was studied. Table 4 and Figure 22 represent the adsorption energies and most stable adsorption geometries of alkali promoters, respectively. Alkali promoters were modelled in their oxidic form and as repetitive units on Co(111) since experimental studies showed that oxidic promoters are dispersed on metal surfaces and bind the surface through their oxygen atoms and they are most stable in their oxidic form under real FTS conditions [35,43]. Zang et al. reported that K_2O is thermodynamically stable under relevant FTS conditions [35]. It is less likely to decompose into K_2 or metal K nor form clusters. Adsorption energies for Li_2O, Na_2O and K_2O were calculated as 314, 403 and 398 kJ/mol, respectively, where hcp site was slightly more preferred for each oxidic promoter. Zhang et al. stated that fcc position is the primary adsorption position for K_2O on Cu(111) surface [32]. However, there is only 5 kJ/mol difference exist between hcp and fcc sites for each alkali promoter which indicates that these adsorption sites are compatible. The small changes in the adsorption configurations and adsorption energies can be attributed to the high mobility of alkali promoters [54,80].

Table 4. Adsorption site and corresponding adsorption energy values for oxidic promoters at 0.11 ML coverage

Alkali Promoter	Adsorption Site	Adsorption Energy (kJ/mol)
Li_2O	hcp	-314
	fcc	-309
Na_2O	hcp	-403
	fcc	-398
K_2O	hcp	-398
	fcc	-393

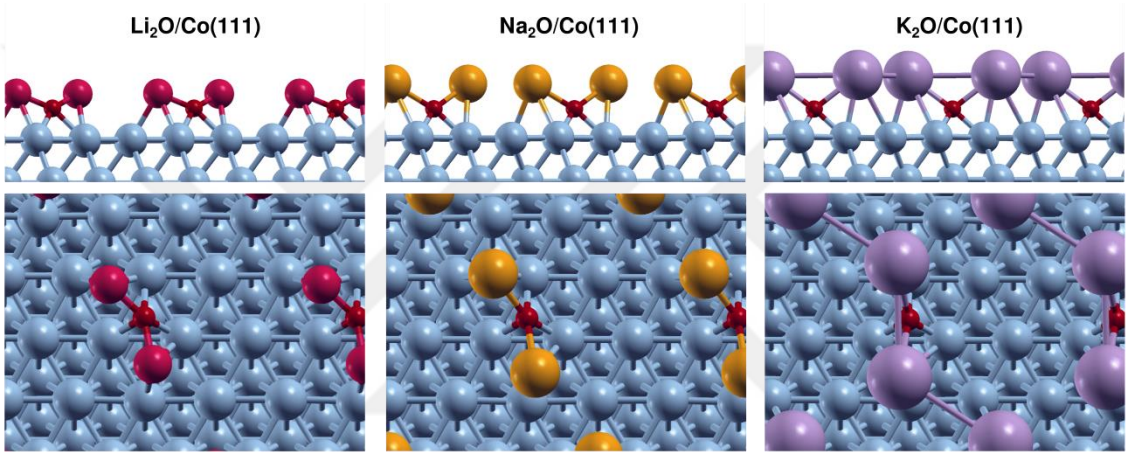

Figure 22. Adsorption energy configurations of oxidic promoters on Co(111) at 0.11 ML coverage

As previously reported in surface science and experimental studies, alkali promoters transfer electrons to the metal surface and alter the surface chemistry hence affecting the adsorption characteristics of FTS reactants [32,53]. Table 5 represents the Bader Charge Analysis for oxidic promoters on the Co(111) surface. Table 5 shows that when alkali promoters are added on Co(111) surface, they donated electron to the Co(111) surface and caused an additional charge accumulation. The charge density of Co particles increased with the increased electronegativity of the alkali promoter. This increased charge density on cobalt particles is reported to form partially reduced cobalt particles [81] and promotes olefins' desorption and restrains the secondary hydrogenation [53] of olefins which is especially beneficial for long-chain olefin production.

Table 5. Bader charge analysis for oxidic promoters on Co(111) surface at 0.11 ML coverage

	Slab (Top 2 Layer)	Alkali Promoter
Clean	0.001	
Li_2O/Co	-0.268	0.272
Na_2O/Co	-0.090	0.090
K_2O/Co	-0.076	0.070

5.1.2 Adsorption of FTS Adsorbates and Intermediates on Co(111) Surface

The main reactants of the Fischer-Tropsch (FT) reaction are carbon monoxide (CO) and hydrogen (H_2). The reaction involves the conversion of these gases into hydrocarbons through a series of chemical reactions. It is known that each catalytic reaction starts with the adsorption of reactants on the surface. Adsorption strength and adsorption site of the reactants and intermediates can significantly affect the reaction pathway, hence product selectivity. Therefore, adsorption of the main reactants and intermediates of FT synthesis was studied for this project.

In order to find the most stable adsorption position for each reactant, all possible adsorption sites on the Co(111) surface are screened and their corresponding adsorption energies are given in Appendix A. Table 6 shows the adsorption energies of FTS reactants and intermediates at their most stable adsorption positions where the geometries are represented in Figure 23.

According to Figure 23, alkali addition changes the adsorption preference of CO from top to hollow site. Also, adsorbates and intermediates mostly preferred the adsorption sites within the region between the two neighboring alkali promoters. Alkali promoters acted as electronic donor on the surface and their interaction with the adsorbates and intermediates stabilized the structures.

Table 6. CO, C, O, H, HCO and H_2CO adsorption energies (kJ/mol) on clean and alkali promoted Co(111) surface at 0.11 ML coverage

	Co (111)	Li_2O/Co(111)	ΔEad (%)	Na_2O/Co(111)	ΔEad (%)	K_2O/Co(111)	ΔEad (%)
CO	-131	-209	37	-194	32	-195	33
C	-604	-679	11	-642	6	-652	7
O	-527	-607	13	-562	6	-569	7
H	-276	-275	-0.4	-269	-2.6	-269	-3
HCO	-192	-245	28	-252	31	-251	31
H_2CO	-43	-104	141	-102	137	-97	56

Experimental and computational investigations indicated that CO adsorption energy increases with alkali promoter addition on Co surface [43]. Our results support the literature since CO adsorption energy increased by 32-37% with alkali addition, but H adsorption energy remained relatively unchanged. Additionally, adsorption energies of FTS intermediates, HCO and H_2CO, significantly increased up to 141%. The restricted hydrogenation capacity along with increased CO adsorption energy is discussed to be one of the reasons for increased olefin selectivity upon alkali addition on cobalt surfaces by experimental and computational studies [43,53]. Moreover, the findings are in line with the experimental studies that under relevant FTS conditions, the surface of the cobalt catalyst is mostly occupied by molecular CO [62].

Even though each alkali promoter's effect on CO and H_2 were analogous, the magnitude of their effect varies. Different effects of alkali can be linked to their capacity to transfer electrons to the Co(111) surface as charge accumulation on the Co(111) surface follows the order of $Li_2O > Na_2O > K_2O$, whereas CO adsorption energy follows the order of $Li_2O > Na_2O \cong K_2O$. To comprehend the varying effects of alkali promoters on the adsorption energies of adsorbates, a Bader Charge Analysis was conducted. The outcomes of this analysis are presented in Table 7. It was found that when CO was added on the alkali promoted surface, both the alkali promoter and the Co(111) surface transferred electrons to CO, causing an additional charge accumulation on CO where CO activation is modulated. The charge accumulation on CO with alkali addition follows the order of $Li_2O > Na_2O > K_2O$ which largely correlates with the corresponding adsorption energies. Alkali addition also increases the charge density on C*, O* and H*. However, the change between the unpromoted and promoted surface is

most dramatic in the case of C and CO which supports the statement that alkalis specifically affect the activation of CO.

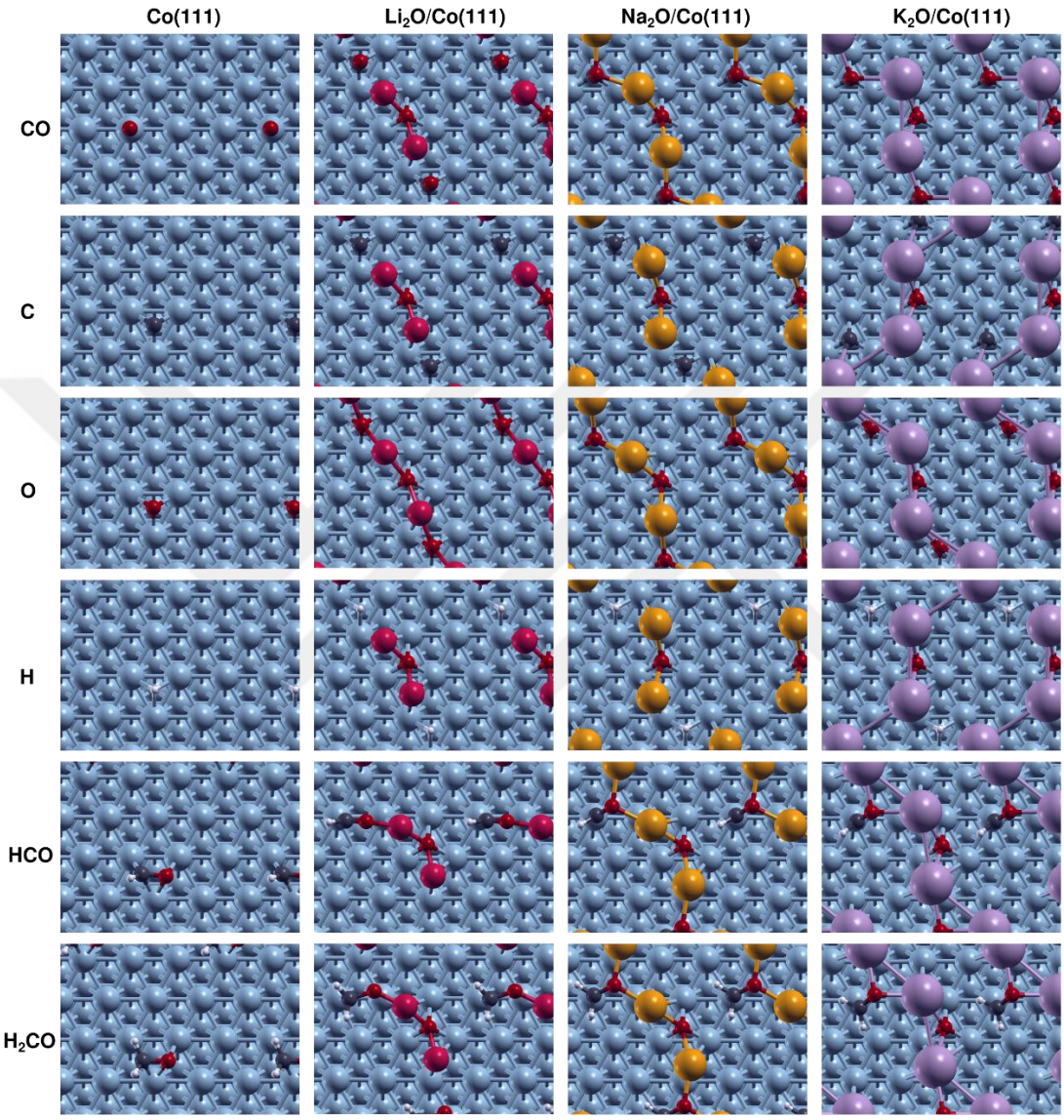

Figure 23. CO, C, O, H, HCO and H_2CO adsorption geometries on clean and alkali promoted Co(111) surface at 0.11 ML coverage

Table 7. Bader charge analysis results for the adsorbates on clean and alkali promoted Co(111) surfaces at 0.11 ML Coverage

		Clean	CO/Co	C/Co	O/Co	H/Co
Clean	Slab (Top 2 Layer)	0.001	0.353	0.879	1.034	0.416
	Alkali Promoter					
	CO		-0.347			
	C			-0.884		
	O				-1.038	
	H					-0.408
Li_2O/Co	Slab (Top 2 Layer)	0.001	0.771	0.899	0.864	0.232
	Alkali Promoter		0.426	0.386	0.444	0.312
	CO		-1.203			
	C			-1.298		
	O				-1.312	
	H					-0.539
Na_2O/Co	Slab (Top 2 Layer)	0.001	0.750	0.949	0.950	0.326
	Alkali Promoter		0.126	0.260	0.234	0.121
	CO		-1.134			
	C			-1.226		
	O				-1.192	
	H					-0.453
K_2O/Co	Slab (Top 2 Layer)	0.001	0.751	1.030	1.106	0.519
	Alkali Promoter		0.237	0.069	0.100	-0.030
	CO		-0.996			
	C			-1.107		
	O				-1.208	
	H					-0.482

As discussed, alkali addition enhances the extent of back-donation from the Co(111) surface to adsorbed CO which effects the bond strength between metal-CO and C-O bonds. In the literature, the interaction between CO and metal particles is often observed through a noticeable shift in the infrared absorption bands of CO [82]. According to Blyholder model, there's a transfer of electrons from carbon monoxide to the metal orbitals through the s bond [83]. Simultaneously, there's an electron back-donation from the metal to the vacant 2p* orbitals of CO. This electron flow leads to a reduction in the bond strength between the carbon and oxygen atoms. Consequently, the infrared absorption bands exhibit a shift towards lower wave numbers compared to gaseous phase CO, which typically resonates at 2143 cm^{-1}. Figure 24 represents the relationship between the C-O bond frequency and C-O bond length for CO on clean and alkali

promoted Co(111) surface. Figure 24 clearly shows that C-O bond frequency decreases with alkali addition whereas C-O bond length increases subsequently. It is reasonable to conclude that alkali addition weakens the C-O bond on the Co(111) surface.

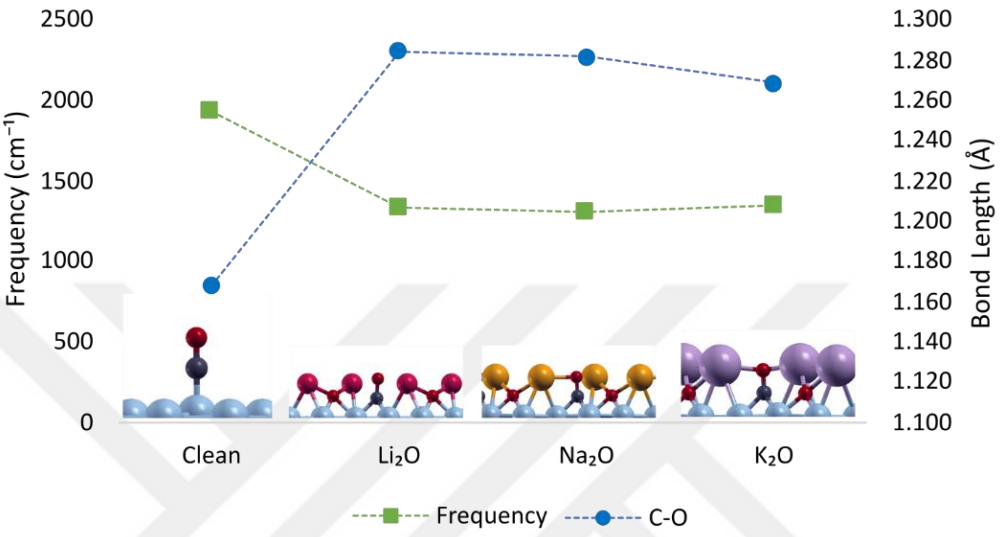

Figure 24. Relationship between C-O bond length and C-O bond frequency for a) CO on clean and alkali promoted Co(111) surface at 0.11 ML coverage. Lines are given to guide the eye.

5.2 Effect of Alkali Coverage on the Adsorption of the Reactants and Intermediates of FTS on Co(111)

5.2.1 Effect of Alkali Coverage on Oxidic Promoter (Li_2O, Na_2O and K_2O) Adsorption

The alkali metal ions interact with the catalyst surface and modify its electronic properties. Therefore, the coverage of alkali promoters on the Co(111) surface is an important subject to discuss as the position of promoters and adsorbates significantly

affect the electronic distribution on the surface. In our work, we have compared the effect of 0.11 ML and 0.06 ML alkali promoter coverages, which correspond to p(3x3) and p(4x4) unit cells, on the adsorption of FTS reactants. 0.11 ML and 0.06 ML coverages also corresponds to 0.493 and 0.659 alkali/nm^2 coverages. Higher promoter coverages was not studied since the study of Jeske and Kizilkaya et al. revealed that coverages exceeding 0.25 ML on the Co(111) surface results in either desorption of CO to the gas phase or decomposition of the promoter structures [43]. Figure 25 represents the adsorption geometries of oxidic promoters on the p(4x4) surface and Table 8 shows the corresponding adsorption energies.

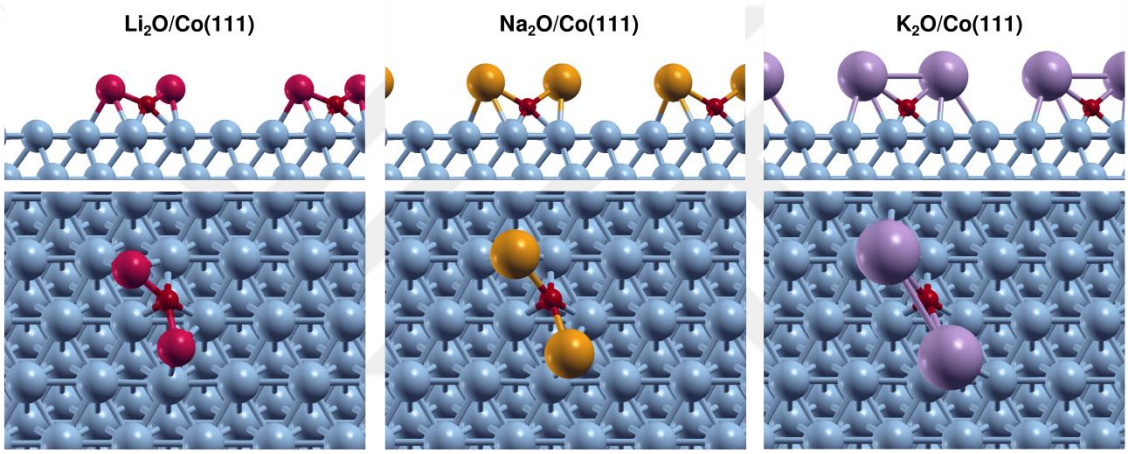

Figure 25. Adsorption energy configurations of oxidic promoters on p(4x4) Co(111) surface at 0.06 ML coverage

As a result of steric effects, adsorption energies increased from 314 to 336 kJ/mol for Li_2O, from 403 to 437 kJ/mol for Na_2O and from 398 to 452 kJ/mol for K_2O. Similar to the p(3x3) surface, hcp adsorption site was slightly more preferred compared to fcc site for each oxidic promoter but the energy difference between the adsorption sites varies between 3-5 kJ/mol, making the adsorption sites compatible. Decreasing alkali coverage resulted in increased alkali adsorption energy, which was expected since with decreasing coverage, repulsive interaction between alkalis also decreases.

Table 8. Adsorption site and corresponding adsorption energy values for oxidic promoters on Co(111) surface at 0.06 ML coverage

Alkali Promoter	Adsorption Site	Adsorption Energy (kJ/mol)
Li_2O	hcp	-336
	fcc	-333
Na_2O	hcp	-437
	fcc	-434
K_2O	hcp	-452
	fcc	-447

Table 9 represents the Bader Charge Analysis for oxidic promoters on Co(111) surface at 0.06 ML coverage. As expected, with the addition of alkali promoters charge density on cobalt particles was increased. Compared to the p(3x3) surface, the charge density on the cobalt surface increased from -0.268 to -0.465 for Li_2O, from -0.090 to -0.515 for Na_2O and from -0.076 to -0.277 for K_2O. Contrary to p(3x3) surface, magnitude of charge density does not correlate with the electronegativity of alkali promoters.

Table 9. Bader charge analysis results for oxidic promoters on the Co(111) surface at 0.06 ML coverage

	Slab (Top 2 Layer)	Alkali Promoter
Clean	-0.095	
Li_2O/Co	-0.465	0.372
Na_2O/Co	-0.515	0.341
K_2O/Co	-0.277	0.298

5.2.2 Effect of Alkali Coverage on Adsorption Characteristics of FTS Adsorbates

Figure 26 demonstrates the most stable adsorption positions of the FTS adsorbates on the p(4x4) surface and Figure 27 compares the adsorption energies of FTS reactants at 0.11 ML and 0.06 ML coverage at their most stable adsorption positions. All possible adsorption sites on the p(4x4) surface and their corresponding adsorption energies are given in Appendix B. When coverage is changed from 0.11 ML to 0.06 ML, the adsorption site preference of the reactants does not change significantly. The region between the alkali promoters still created the most stable adsorption geometries for the reactants.

On clean surface, only the adsorption energy of C significantly changes from 604 to 642 kJ/mol but the coverage does not have a considerable effect on other reactants. On alkali promoted Co(111) surfaces, when coverage is changed from 0.11 ML to 0.06 ML, CO adsorption energy decreased from 209 to 179 kJ/mol and from 194 to 176 kJ/mol for Li_2O and Na_2O promoted Co(111) surfaces, respectively. Contrary, CO adsorption energy on K_2O promoted Co(111) surface slightly increased from 194 kJ/mol to 202 kJ/mol. Even though a slight increase in CO adsorption energy is observed for K_2O promoted surface, it is expected to be decreasing with further decreased coverages. Based on these results, 0.11 ML (0.493 alkali/nm^2) coverage is discussed to be the optimum coverage for alkali promoters on the Co(111) surface as higher coverages result in CO desorption to the gas phase and lower coverages results in reduced CO adsorption energy.

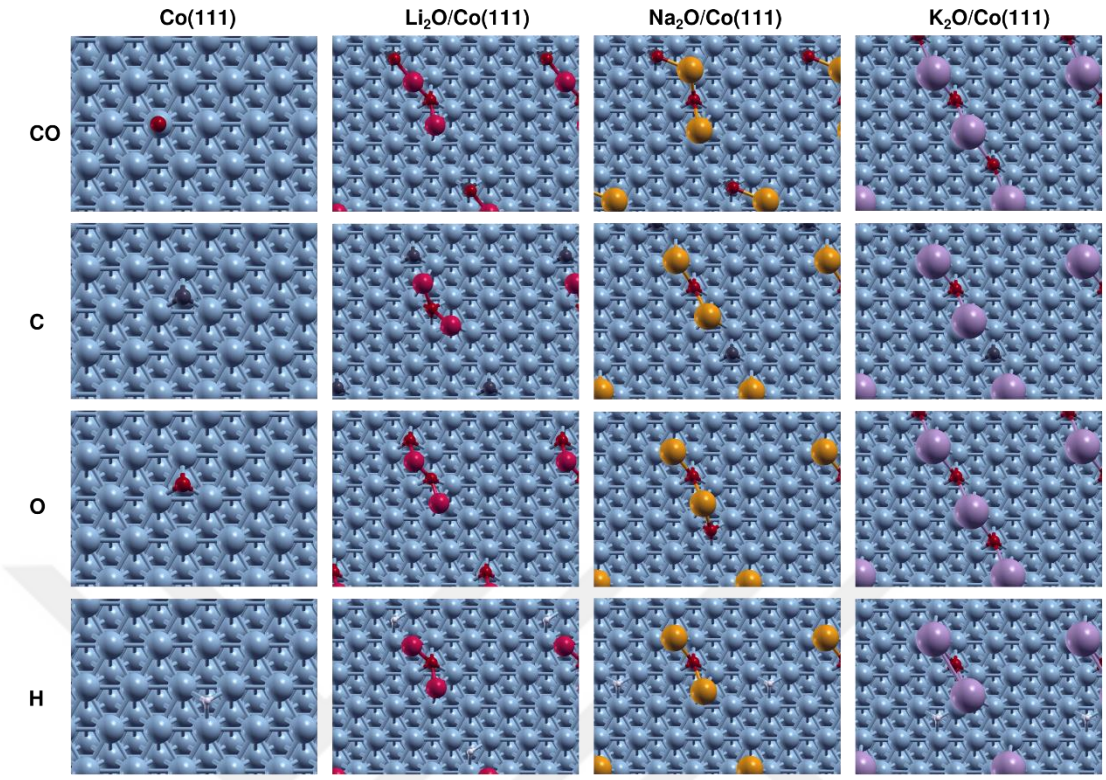

Figure 26. CO, C, O and H adsorption geometries on clean and alkali promoted Co(111) surfaces at 0.06 ML coverage

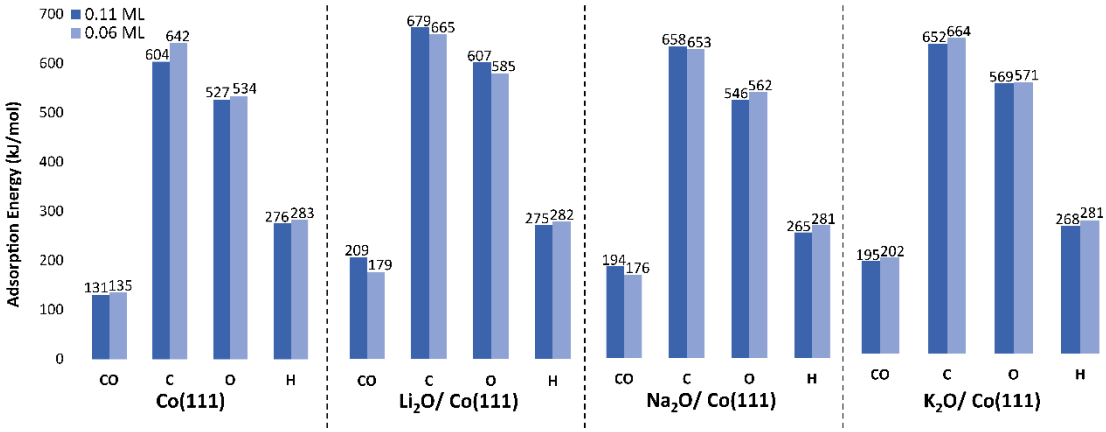

Figure 27. CO, C, O and H adsorption energies for clean and alkali promoted p(3x3) and p(4x4) surfaces

In order to explain the different coverage-related adsorption characteristics of alkali promoted Co(111) surfaces, Bader Charge Analysis was performed and results are given in Table 10. According to Table 10, charge density resulting from the electron transfer of alkali promoter and cobalt surface to CO decreased from -1.203 to -0.928 and from -1.134 to -0.901 for Li_2O and Na_2O promoted surfaces, respectively. Contrary, charge accumulation on CO increased from -0.996 to -1.018 for K_2O which well explains the increased CO adsorption energy for K_2O promoted surface when coverage changed from 0.11 ML to 0.06 ML. Additionally, it was found that decreasing the alkali coverage also decreases the charge accumulation on C*, O* and H*.

Table 10. Bader charge analysis results for the adsorbates on clean and alkali promoted Co(111) surfaces at 0.06 ML coverage

		Clean	**CO/Co**	**C/Co**	**O/Co**	**H/Co**
	Slab (Top 2 Layer)	-0.095	0.392	0.892	0.966	0.369
	Alkali Promoter					
Clean	CO		-0.378			
	C			-0.923		
	O				-0.984	
	H					-0.387
	Slab (Top 2 Layer)	-0.095	0.491	0.702	0.692	0.037
	Alkali Promoter		0.436	0.413	0.422	0.383
Li_2O/Co	CO		-0.928			
	C			-1.116		
	O				-1.165	
	H					-0.420
	Slab (Top 2 Layer)	-0.095	0.425	0.584	0.811	0.018
	Alkali Promoter		0.462	0.439	0.399	0.370
Na_2O/Co	CO		-0.901			
	C			-1.072		
	O				-1.140	
	H					-0.421
	Slab (Top 2 Layer)	-0.095	0.604	0.803	0.702	0.090
	Alkali Promoter		0.486	0.351	0.411	0.305
K_2O/Co	CO		-1.018			
	C			-1.109		
	O				-1.115	
	H					-0.422

As mentioned previously, the work of Liu et al. revealed the importance of the distance between adsorbates and alkali promoter as CO dissociation strongly depends on the distance from the alkali promoter. In order for an alkali promoter to fully exhibit its promotional effect, the distance between alkali promoter and CO needs to be lower than 3 Å for ionic interactions to become dominant. Figure 28 represents the distance between the alkali promoter and CO on 0.11 ML and 0.06 ML surfaces. As expected, the distance between the alkali promoter and CO increases with increasing atomic radius of the alkali promoter. As the coverage changes from 0.11 ML to 0.06 ML, the distance between the alkali promoter and CO decreases for Li_2O and Na_2O promoted surfaces. There is no considerable change in K_2O promoted surface. The magnitude of reduction of the distance also decreases with atomic radius. Ultimately, the distance between alkali promoter and CO is below 3 Å for each alkali promoter at each tested coverage which indicates that the interaction between alkali promoter and CO will be ionic and promotional effect of alkali promoters will not be reduced. However, the calculations also revealed that in order to maximize the efficiency of the CO dissociation, the fine tuning of alkali-CO distance below 3 Å also possesses great importance. On Na_2O promoted surface, even though the distance (2.354 Å) between the alkali promoter and CO is shorter on the 0.06 ML surface, the charge accumulation on CO (0.11 ML: -1.134, 0.06 ML:-0.901) on the 0.11 ML surface is higher as CO makes bond with two alkali promoters instead of one.

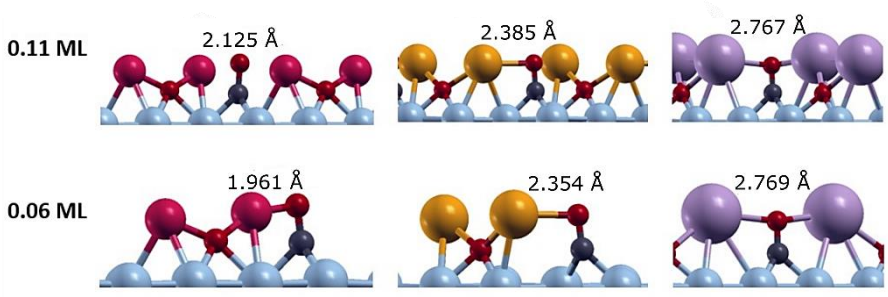

Figure 28. Distance between alkali promoters and CO at 0.11 and 0.06 ML coverages

5.3 Effect of Alkali Promoters on CO Dissociation on Co(111)

For Co-based FTS catalysts, two mechanisms have been extensively discussed for CO dissociation which are direct and H-assisted dissociation [18]. All investigated reactions and their corresponding activation barriers and reaction energies are listed in Table 11.

Table 11. Investigated reactions and their corresponding activation barriers and reaction energies

	Reaction	E_a (kJ/mol)	E_{rxn} (kJ/mol)
Clean	$CO \rightarrow C + O$	276	100
	$CO + H \rightarrow HCO$	120	100
	$HCO \rightarrow CH + O$	77	-61
	$HCO + H \rightarrow H_2CO$	43	10
	$H_2CO \rightarrow CH_2 + O$	63	-56
Li_2O	$CO \rightarrow C + O$	241	112
	$CO + H \rightarrow HCO$	103	88
	$HCO \rightarrow CH + O$	88	-52
	$HCO + H \rightarrow H_2CO$	45	1
	$H_2CO \rightarrow CH_2 + O$	80	-47
Na_2O	$CO \rightarrow C + O$	240	117
	$CO + H \rightarrow HCO$	92	88
	$HCO \rightarrow CH + O$	95	-19
	$HCO + H \rightarrow H_2CO$	25	4
	$H_2CO \rightarrow CH_2 + O$	95	-2
K_2O	$CO \rightarrow C + O$	237	119
	$CO + H \rightarrow HCO$	100	86
	$HCO \rightarrow CH + O$	153	-15
	$HCO + H \rightarrow H_2CO$	23	11
	$H_2CO \rightarrow CH_2 + O$	86	-28

5.3.1 Direct CO Dissociation

The mechanism of CO dissociation on cobalt surfaces has been extensively studied using various experimental and theoretical methods [19,20]. In order to understand the effect of alkali promoters on direct CO dissociation, CI-NEB calculations were performed. Initial, transition and final state geometries are represented in Figure 29 and PED diagram is given in Figure 30. For the clean Co(111) surface, the activation barrier and the reaction energy were calculated as 276 kJ/mol and 100 kJ/mol, respectively. In the literature, activation barriers for direct CO dissociation on Co(111) are calculated as 231.4 kJ/mol and 235 kJ/mol for Co(111) [19,20]. The difference between the reported and literature values may be due to the usage of different functionals for DFT calculations performed in the other studies.

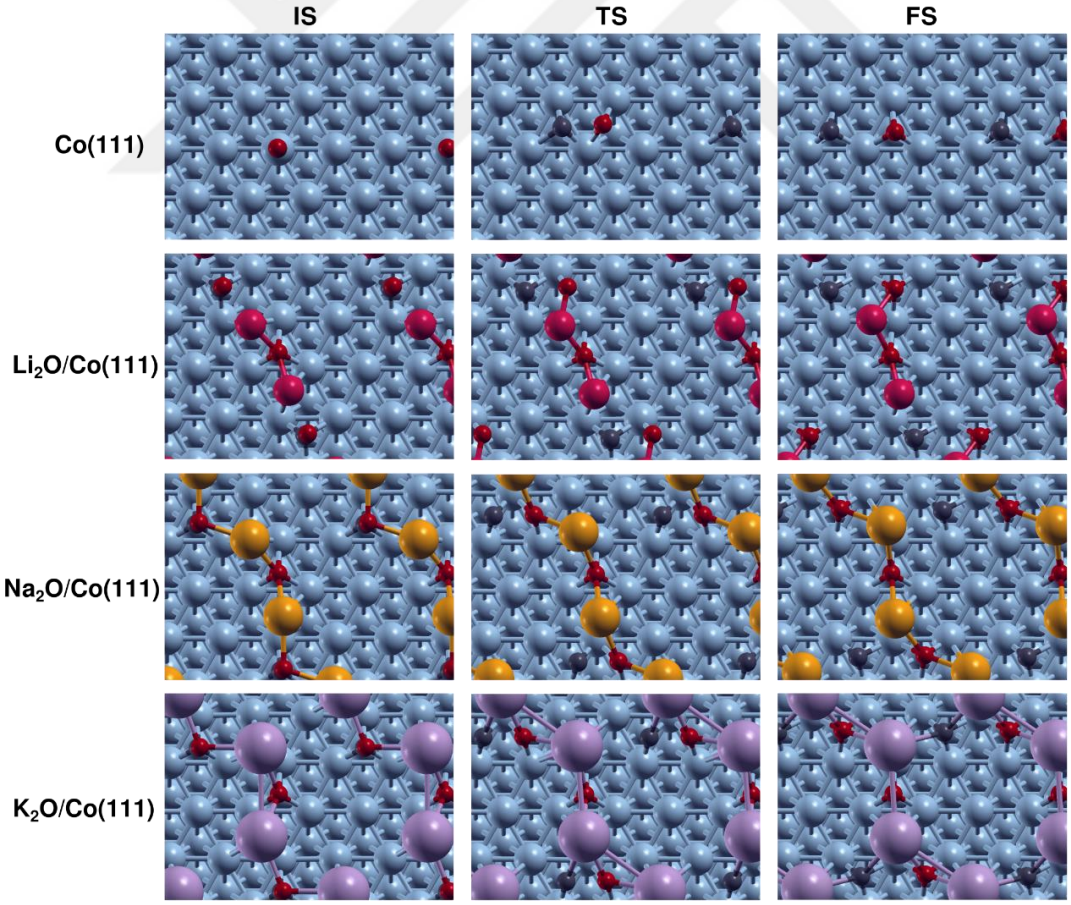

Figure 29. Initial, transition and final state geometries of direct CO dissociation on clean and alkali promoted Co(111) surfaces

It can be clearly seen that when alkali promoters are added on Co(111) surface, activation barrier decreased by approximately 35-39 kJ/mol. Similar dissociation mechanism (Figure 29) was observed in each alkali promoter where O* of the CO interacts with the alkali promoter and subsequently CO bond stretches compared to its initial state. For Li_2O, Na_2O and K_2O promoted surfaces, CO bond stretches from 1.168 Å to 1.285 Å, 1.282 Å and 1.269 Å, respectively.

Even though alkali oxides decrease the activation barrier and promote CO dissociation, the calculated barriers are still very high to simulate real life conditions where CO dissociation barrier during FTS varies between 100-200 kJ/mol [18]. Hence, it can be stated that direct CO dissociation is not likely to take place on clean and alkali promoted Co(111) surface due to its significantly high activation barrier of >200 kJ/mol.

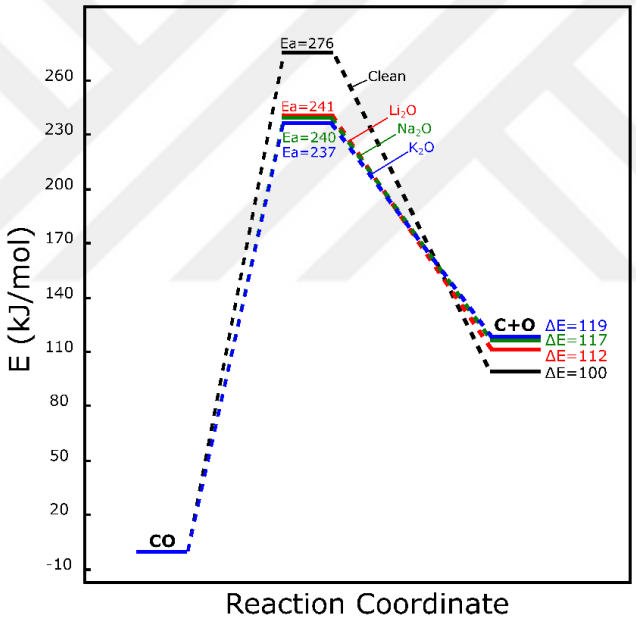

Figure 30. Potential energy diagram for direct CO dissociation on clean and alkali promoted Co(111) surface

5.3.2 H-assisted CO Dissociation

The presence of hydrogen on the catalyst surface can significantly influence the CO dissociation mechanism and reduce the energy barrier for the reaction. Experimental

and computational studies revealed that hydrogenation is the preferred path for CO activation on the flat Co(111) surface [18–20]. Also, Yu et al. reported that the direct dissociation is more favorable on hcp cobalt, while the hydrogen-assisted pathway is preferable for fcc cobalt [53]. In the H-assisted FTS, COH, HCO and H_2CO have been proposed as potential key intermediates on Co surfaces based on to the results of the DFT calculations. Chen et al. reported that, on the flat-Co(111) surface the formation of HCO as intermediate is more preferred both kinetically and thermodynamically compared to formation of COH since the hydrogenation of O has 50 kJ/mol higher activation barrier compared to oxidation of C [19,20]. Additionally, Zhang et al. showed that K_2O addition on Cu(111) surface increased the COH activation barrier by 99 kJ/mol [32]. Therefore, COH intermediate is excluded from this work.

Figure 31 represents the initial, transition and final state geometries for HCO mediated CO dissociation on clean and alkali promoted Co(111) surfaces. Potential energy diagram for the reaction also given in Figure 32. For HCO mediated CO dissociation, activation barriers for HCO formation and dissociation are calculated as 120 kJ/mol and 100 kJ/mol for clean surface, respectively. It clearly shows that CO activation via H-assisted route is more plausible than direct CO dissociation into C and O since significantly higher activation barrier is required for the direct C−O bond scission.

Alkali addition was found to promote HCO formation since the calculated HCO formation barriers for Li_2O, Na_2O and K_2O promoted surfaces were 103, 95 and 100 kJ/mol, respectively. Adsorption studies also revealed that alkali addition greatly stabilizes HCO formation as the adsorption energy of HCO increased from 192 kJ/mol to 245, 252 and 251 kJ/mol on Li_2O, Na_2O, and K_2O promoted surfaces, respectively. However, alkali addition increased the activation barrier for the dissociation of HCO into CH and O. Dissociation barriers for the Li_2O, Na_2O, and K_2O promoted Co surfaces were calculated as 88 kJ/mol, 95 kJ/mol and 153 kJ/mol, respectively. These reaction barriers are still achievable during FT synthesis since the plausible activation barriers for FTS ranges between 100-200 kJ/mol. However, alkali promoters do not appear to show enhanced properties in terms of C-O dissociation. In fact, they decrease the CO dissociation rate upon addition. Additionally, there are significant differences on the effect of alkali promoters on CO dissociation. K_2O addition significantly decreases the CO dissociation rate compared to other alkali promoters.

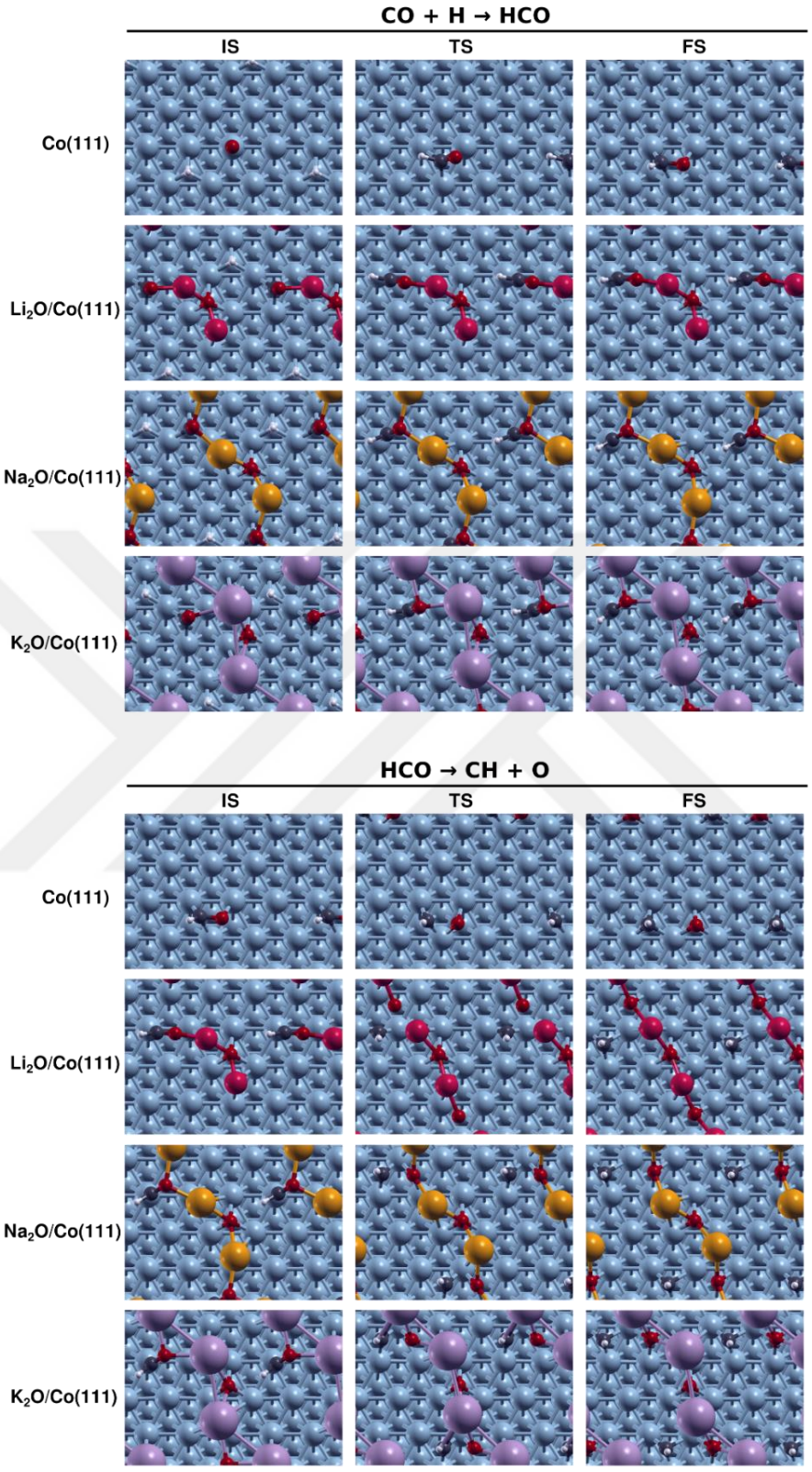

Figure 31. Initial, transition and final state geometries of HCO mediated CO dissociation on clean and alkali promoted Co(111) surface

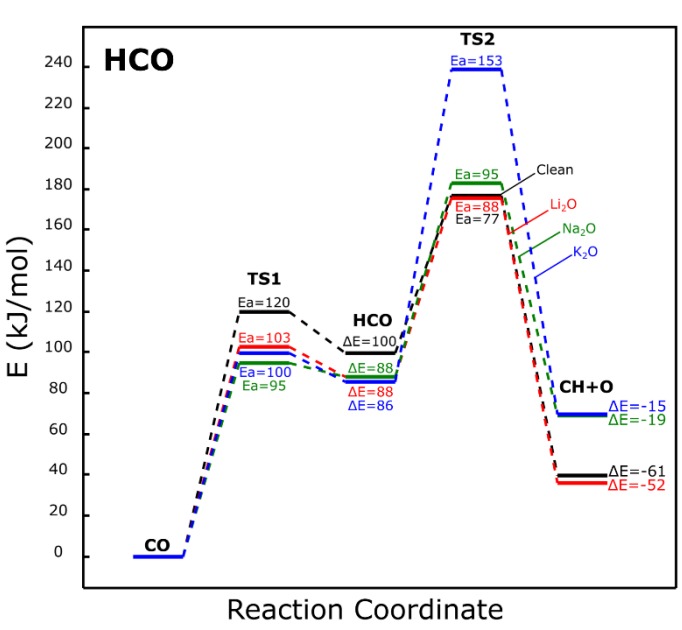

Figure 32. Potential energy diagram for HCO mediated CO dissociation on clean and alkali promoted Co(111) surface

HCO can further hydrogenate into H_2CO and subsequently dissociate into CH_2 and O. Figure 33 represents the initial, transition and final state geometries for H_2CO mediated CO dissociation on clean and alkali promoted Co(111) surfaces and corresponding potential energy diagram is given in Figure 34. On clean Co(111) surface, activation barriers for H_2CO formation and dissociation were calculated as 43 kJ/mol and 63 kJ/mol, respectively. Alkali addition significantly increases the adsorption energy of H_2CO intermediate as adsorption energy of H_2CO increased from 4 kJ/mol to 104, 102 and 97 kJ/mol on Li_2O, Na_2O, and K_2O promoted surfaces, respectively. H_2CO formation barriers on Li_2O, Na_2O, and K_2O surfaces were calculated as 45, 25, and 23 kJ/mol, respectively. H_2CO formation is promoted with the addition of Na_2O and K_2O whereas Li_2O addition does not have a considerable effect on the H_2CO formation. Similar to HCO mediated mechanism, alkali addition increased the activation barrier of H_2CO dissociation into CH_2 and O where activation barriers for Li_2O, Na_2O, and K_2O promoted surfaces were calculated as 80, 95, and 86 kJ/mol, respectively.

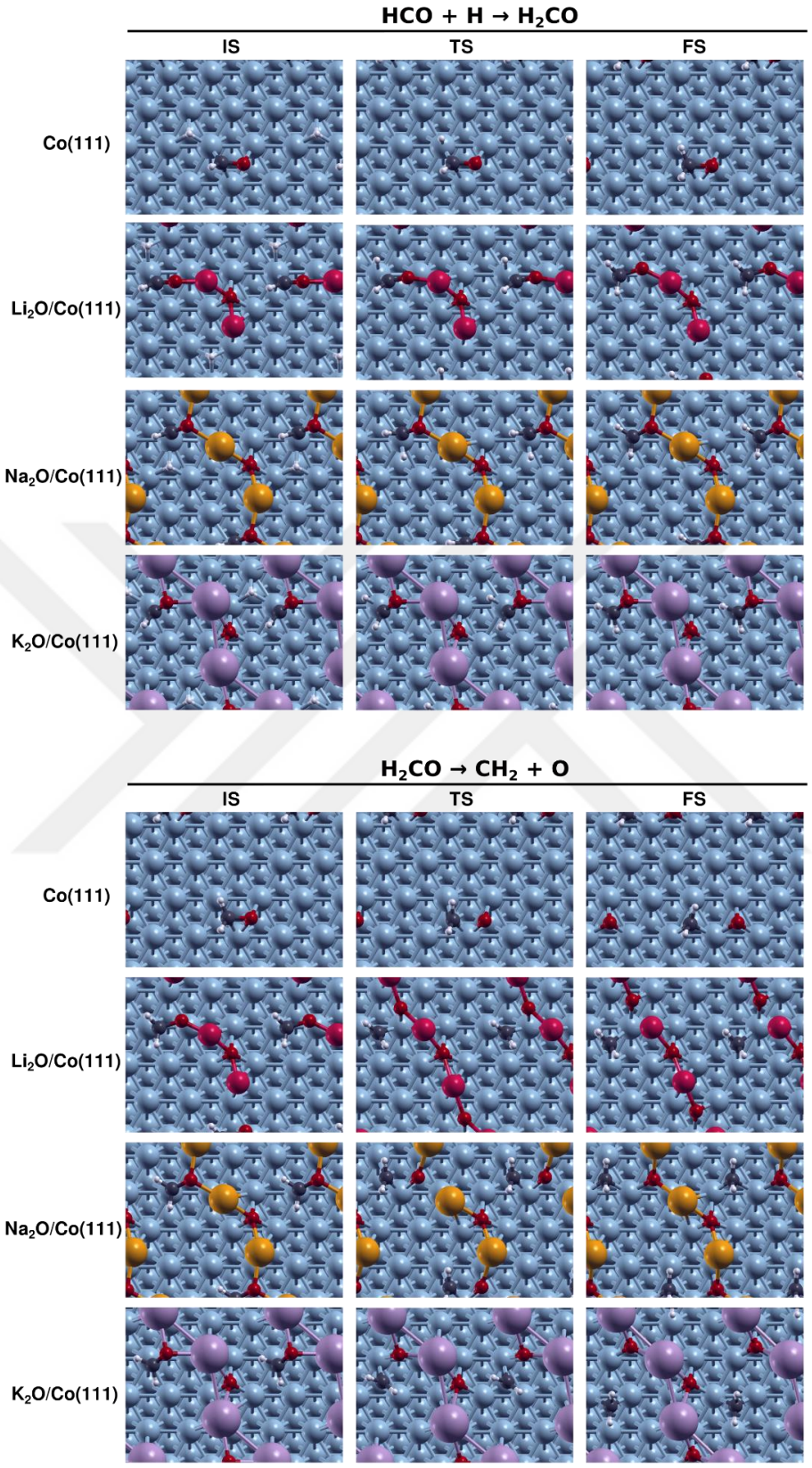

Figure 33. Initial, transition and final state geometries of H_2CO mediated CO dissociation on clean and alkali promoted Co(111) surface

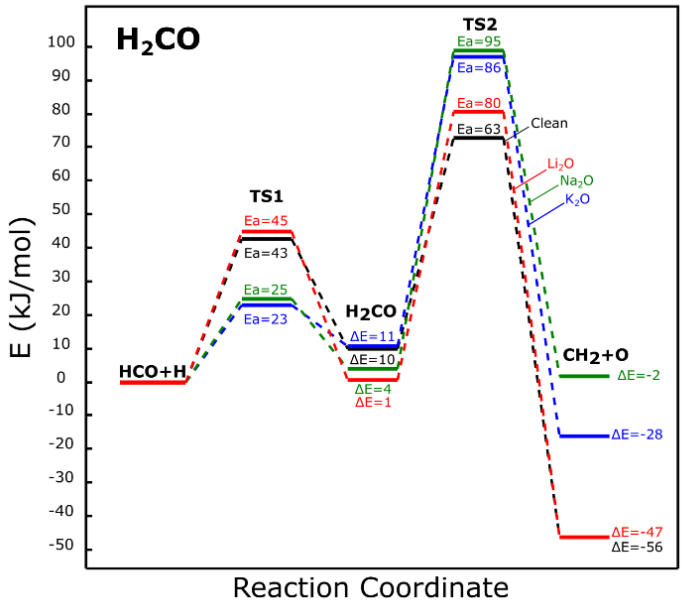

Figure 34. Potential energy diagram for H_2CO mediated CO dissociation on clean and alkali promoted Co(111) surface

For H-assisted pathways, although alkali promotion favors the formation of HCO and H_2CO, it increases the activation barrier for HCO and H_2CO dissociation, overall decreasing the H-assisted CO dissociation rate. In order to understand the increased activation barrier for the H-assisted mechanism, C-O bond length analysis was performed and the results are represented in Figure 35. The reason for the reduced CO dissociation rate upon alkali addition is the decreased C-O bond length resulting from the tilted geometry of HCO and H_2CO due to interaction with alkali promoters. Increased CO bond strength well explains the increased activation barrier upon alkali addition.

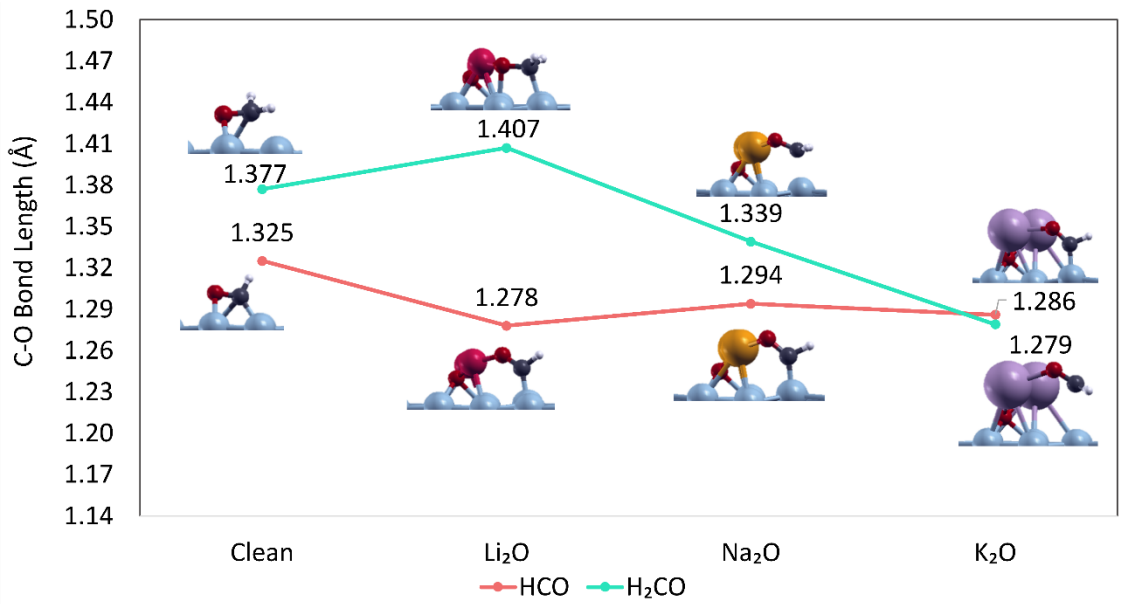

Figure 35. C-O bond length analysis for HCO and H_2CO for Li_2O, Na_2O and K_2O promoted Co(111) surfaces. Lines are given to guide the eye.

Several experimental studies stated that activity and selectivity values change for different alkali promoters [1,2,53]. Our results indicate that the CO dissociation mechanism on the alkali promoted Co(111) surface is not responsible for varying selectivity values for different alkalis, since all three alkali promoters affected the reaction in a similar way. However, different CO activity values could be linked to the magnitude of the effect of alkali promoters on HCO and H_2CO dissociation barriers. Additionally, adsorption characteristics of all alkali promoters were found analogous.

Different effects of alkali promoters during the FTS reaction could be resulted from the varying mobility of alkali promoters. Alkali metals exhibit an increasing atomic radius and decreasing electronegativities with increasing atomic number. This phenomenon can have an impact on their mobility and distribution within catalysts, consequently influencing their catalytic performance. Yu et al. was able to reveal a correlation between the electronegativity of alkali promoters and their FTS activity on Ru-based FTS catalysts [53]. However, our results on the Co(111) surface revealed no correlation between alkali promoters' electronegativity and their effect on CO adsorption and dissociation. Figure 36 represents the relationship between the charge transfer capacity of alkali promoters to cobalt surface to adsorption and dissociation

energy of CO, HCO and H_2CO. As shown in Figure 36a, as charge transfer capacity increases, adsorption energy also increases for H_2CO. However, for HCO and CO, no linear relationship was observed between the charge transfer capacity of alkali promoters and CO and H_2CO adsorption energies. According to Figure 36b, as charge transfer capacity of alkali promoters increases, activation barrier for CO dissociation also increases while decreases for HCO dissociation. H_2CO dissociation followed a volcano-like trend. No apparent relationship was observed between CO adsorption energy and activation energy for CO, HCO and H_2CO dissociations.

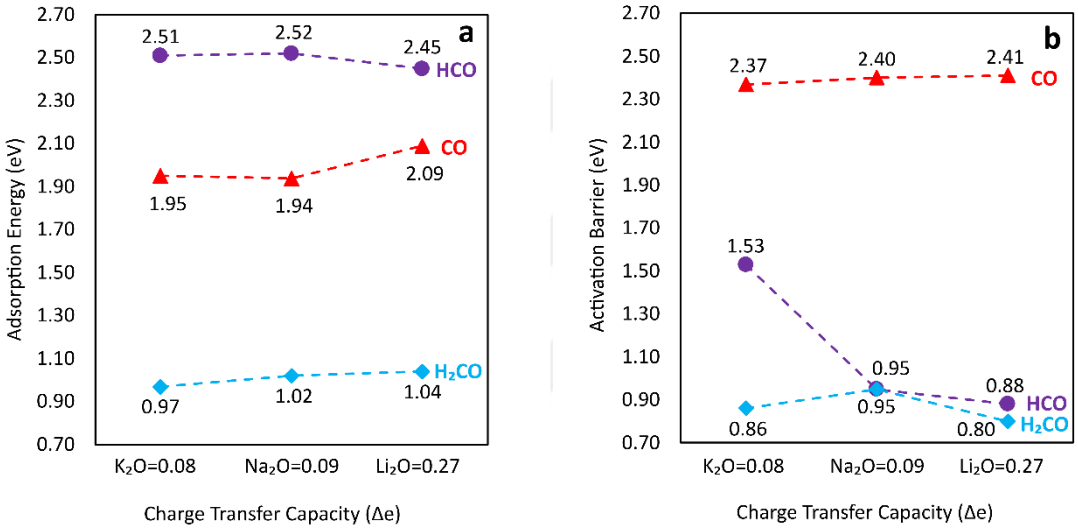

Figure 36. Relationship between charge transfer capacity of alkali promoters to cobalt surface (Δe) and a) adsorption energy (eV) and b) activation barrier for CO, HCO and H_2CO dissociation. Lines are given to guide the eye.

Li et al. studied the mobility of different alkali promoters (Li, Na, K, Rb and Cs) on Fe-based catalyst and found that the positions of the alkalis change during FTS reaction [54]. Their results revealed that Li and Na promoters diffuse into the bulk of catalysts while K mostly concentrates on the surface before the reaction. After FTS reaction, Li and Na diffuse out of the catalyst bulk while the surface K concentration remains unchanged. They linked the different activity and selectivity values of different alkali promoters to their varying mobility as Li and Na decrease the activity while K

increase the activity of iron catalysts. Further studies on the mobility of alkali promoters on the Co(111) surface could be useful to reveal the different effects of alkali promoters on the Co(111) surface.

As mentioned previously, cobalt nanoparticles consist of different facets that show different activity and selectivity values. Latest studies revealed that stepped surfaces show much higher CO activity compared to flat surfaces [43,84]. Further studies should be focused on analyzing the effect of alkali promoters on stepped surfaces to explain the increased CO activity and olefin selectivity upon alkali addition.

5.4 Effect of Alkali Promoters on Carbon Coverage

The results presented in Section 5.1 revealed that alkali addition makes the surface more carbophilic since C adsorption energy increased by 7-13% upon alkali addition. Zhang et al. examined the impact of K on the Co(0001) surface and concluded that as the surface carbon concentration rises, the carbon adsorbed on the cobalt surface undergoes a transformation into carbon chains [34]. It is also considered as the precursor to long-chain alkanes or graphene. Valero et al. performed a DFT study on the stability of carbon on the Co(111) surface and found that Co sites have a strong tendency to be covered by carbon during the FTS reaction [85]. However, this increased C affinity may either cause a formation of graphene overlayer which could be the reason for deactivation of Co-based catalysts during FTS or C atoms may diffuse into the subsurface of Co and cause carbide formation. Experimental and computational studies revealed that alkali addition can stabilize the cobalt carbide phase during FTS [35,43]. Cobalt carbide formation is not wanted as they shift the selectivity from heavy hydrocarbons to alcohols and can promote the unwanted WGSR [33,43,50]. Therefore, a detailed study was performed to understand the effect of alkali promoters on carbon coverage.

In our work, 0.11 ML, 0.22 ML, and 0.33 ML carbon coverages were studied on clean and alkali promoted Co(111) surfaces. Surface carbon geometries are given in Figure 37 and adsorption energy results are represented in Figure 38. Coverages above

0.33 ML was not studied as 0.33 ML was the highest coverage that can be achieved on K_2O promoted surface without the formation of carbon chains.

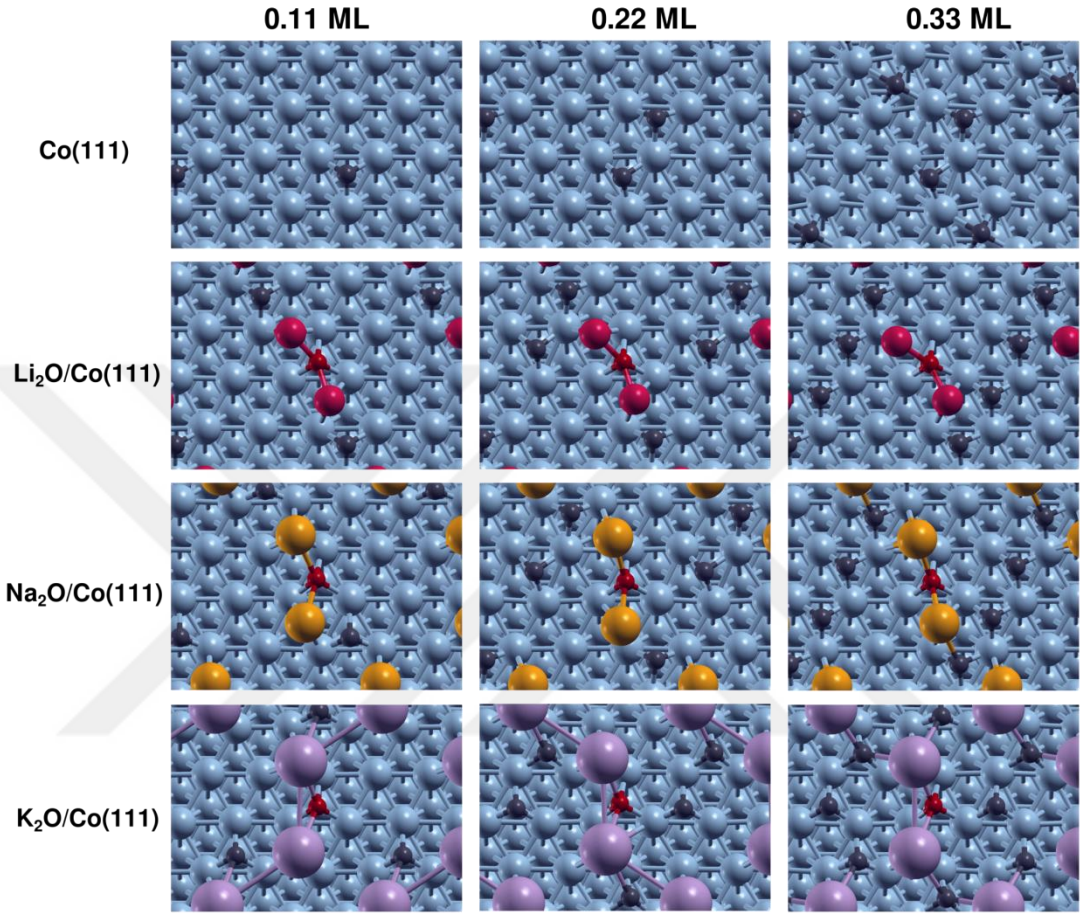

Figure 37. Surface carbon coverages at 0.11, 0.22 and 0.33 ML on clean and alkali promoted Co(111) surface

For clean Co(111) surface, subsurface C was more stable at every tested coverage. For alkali promoted Co(111) surfaces, at 0.11 ML coverage, surface C geometries were found to be more stable compared to subsurface geometries. As the surface carbon coverage on the alkali promoted Co(111) surface increases, subsurface carbon geometries became more stable due to strong repulsion between carbon atoms which may enhance the carbide formation. However, more detailed analyses based on

the kinetics of subsurface carbon diffusion have to be performed in order to have a clear understanding of carbide formation.

It was also found that the coverage dependent carbon diffusion effect of alkali promoters varies. K_2O increases the subsurface carbon diffusion rate more compared to other alkali promoters even at low coverages. Zhang et al. investigated the effect of alkali promoters on cobalt carbide formation and found that K_2O coverage strongly affects the Co_2C formation and Co_2C crystal morphology [35]. The higher K_2O coverages results in higher surface energy drops and the surface energy reduction rates of most C terminated surfaces were found to be higher than Co-terminated surfaces.

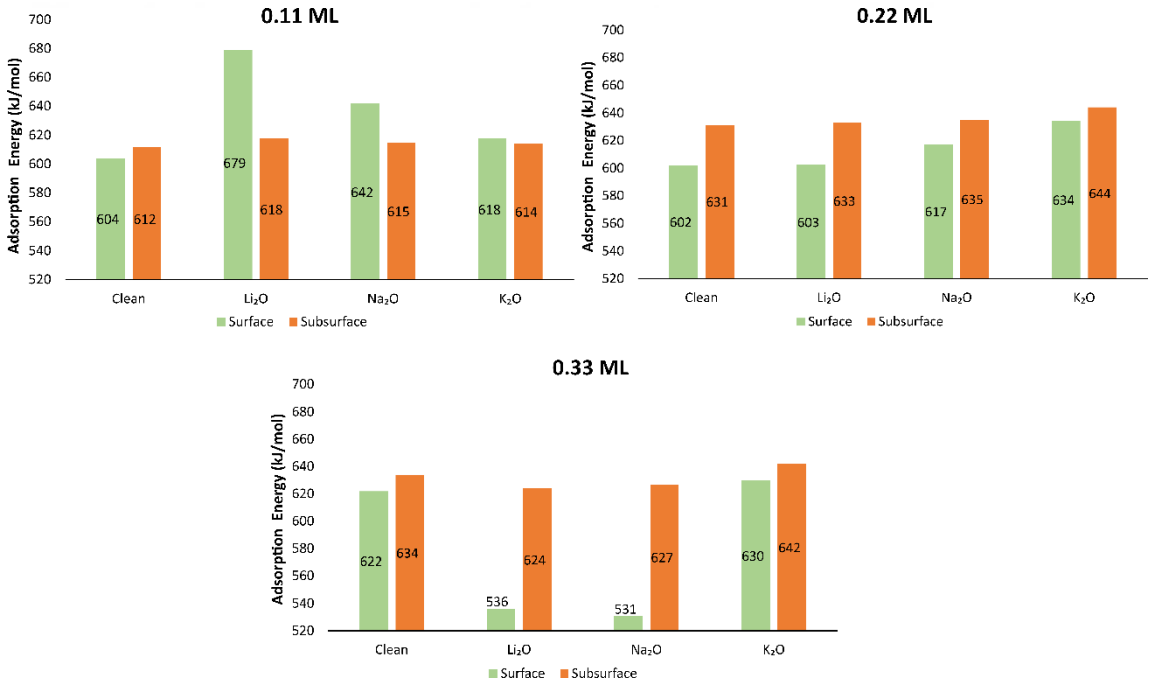

Figure 38. Adsorption energies of surface and subsurface carbon atoms on clean and alkali promoted Co(111) surface at a) 0.11 ML, b) 0.22 ML and c) 0.33 ML coverages

Zonnevylle et al. investigated the effect of subsurface carbon on the Co(0001) surface and suggested that the presence of subsurface C decreases the backbonding capacity of Co metal which results in the reduction of CO adsorption and dissociation [61]. In order to understand the effect of C on CO adsorption, Bader Charge Analysis was performed at 0.11 ML, 0.22 ML, and 0.33 ML C coverages on clean and alkali

promoted Co(111) surface and represented in Figure 39 along with corresponding CO adsorption energies. Figure 39 shows that when C is located at subsurface, the charge accumulation on CO increases except for clean and 0.11 ML Li_2O promoted surface. Also, regardless of the charge transfer, CO adsorption energy was higher at every tested coverage when C was located at subsurface of Co which indicates that subsurface C does not poison CO adsorption on the Co(111) surface.

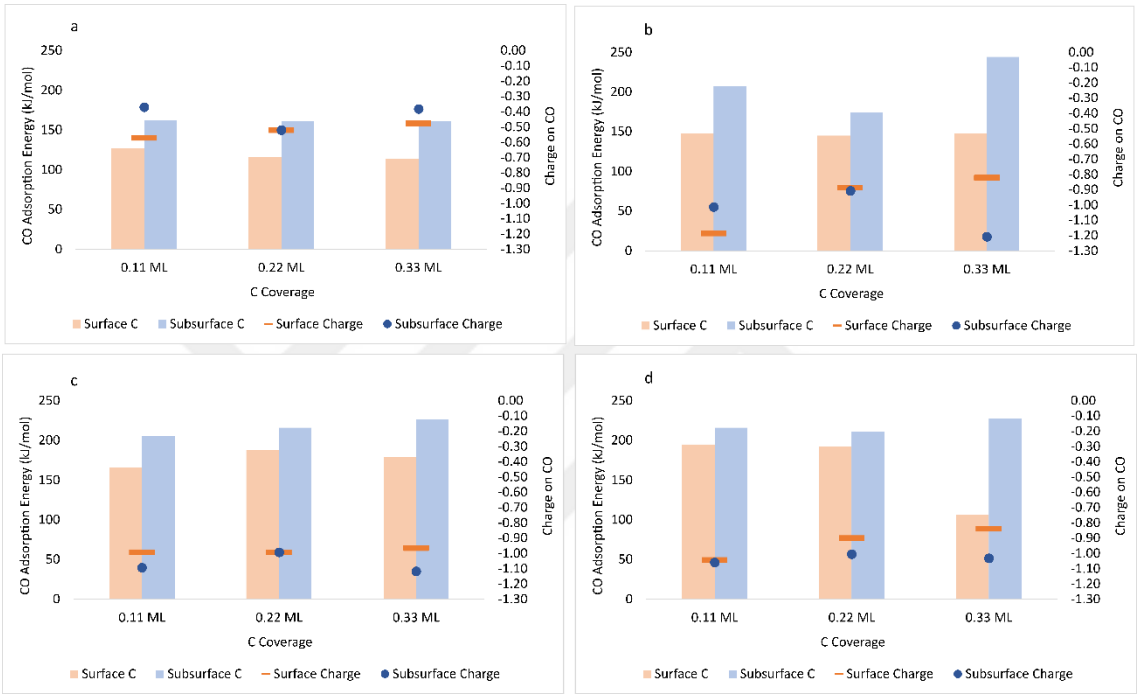

Figure 39. Charge and adsorption energy values of CO at 0.11 ML, 0.22 ML and 0.33 ML surface and subsurface C coverages on a) Clean, b)Li_2O, c)Na_2O and d)K_2O promoted Co(111) surface.

CHAPTER 6

CONCLUSION

In this work, the effect of oxidic alkali (Li, Na and K) promoters on the adsorption and dissociation mechanism of CO on the Co(111) surface were studied by using DFT modelling. The adsorption studies showed that adsorption energies of CO, HCO and H_2CO significantly increased upon alkali addition but alkali addition did not cause a significant effect on other FTS reactants. According to Bader Charge Analysis, alkali addition on Co(111) surface caused an additional charge accumulation on Co particles. The charge densities of surface cobalt atoms were increased with increasing electronegativity of alkalis. For Co(111) surfaces with adsorbed CO, charge transfer occurred from cobalt atoms and alkali promoter to the adsorbed CO which modulated the activation of CO. The increased backdonation from surface to CO decreased the strength of C-O bond which subsequently resulted in 35-39 kJ/mol lower activation barrier for direct CO dissociation compared to clean Co(111) surface. However, due to significantly high activation barrier (>200 kJ/mol) of direct CO dissociation, the reaction is not likely to take place in practical low-temperature FTS conditions. Alkali addition was also found to increase the activation barriers for HCO and H_2CO dissociation which decreased the overall CO dissociation rate. Yet, H-assisted pathway was found as the preferred pathway on alkali promoted Co(111) surface and CO dissociation follows the reaction path of $CO + H \rightarrow HCO \rightarrow HCO + H \rightarrow H_2CO \rightarrow CH_2 + O$. The decreased H-assisted CO dissociation rate was attributed to the increased C-O bond strength resulting from the interaction of HCO and H_2CO with alkali promoter.

Effect of alkali promoter coverage on FTS adsorbates was also studied and results indicated that 0.11 ML alkali coverage was the optimum alkali coverage on Co(111) surface. The fine tuning of the distance between alkali promoter and CO under 3 Å were found to have a significant importance for the destabilization of adsorbed CO.

Effect of alkali promoters on carbon coverage was also studied and results showed that alkali addition makes the surface more carbophilic since C adsorption energy increased by 7-13% upon alkali addition. Lastly, it was found that presence of C in Co lattice does not limit the charge transfer capacity of Co nanoparticle to CO.

REFERENCES

(1) Owen, R. E.; O'Byrne, J. P.; Mattia, D.; Plucinski, P.; Pascu, S. I.; Jones, M. D. Cobalt Catalysts for the Conversion of CO_2 to Light Hydrocarbons at Atmospheric Pressure. *Chem. Commun.* **2013**, *49* (99), 11683–11685. DOI: 10.1039/C3CC46351A

(2) De La Osa, A. R.; De Lucas, A.; Valverde, J. L.; Romero, A.; Monteagudo, I.; Coca, P.; Sánchez, P. Influence of Alkali Promoters on Synthetic Diesel Production over Co Catalyst. *Catal. Today* **2011**, *167* (1), 96–106. DOI: 10.1016/j.cattod.2010.11.064

(3) Olivier, J. G. J.; Schure, K. M.; Peters, J. A. H. W. *Trends in Global CO_2 and Total Greenhouse Gas Emissions 2017 Report*; PBL Netherlands Environmental Assessment Agency, 2017. https://www.pbl.nl/en/publications/trends-in-global-co2-and-total-greenhouse-gas-emissions-2017-report (accessed 2023-11-15)

(4) Newsham, A.; Kohnstamm, S.; Naess, L. O.; Atela, J. *Working Paper 9: Agricultural Commercialisation Pathways: Climate Change and Agriculture*; Agricultural Policy Research in Africa (APRA), 2018. https://www.future-agricultures.org/publications/working-papers-document/agricultural-commercialisation-pathways-climate-change-and-agriculture/ (accessed 2023-11-15)

(5) Umbach, *F. Energy Security in a Digitalised World and Its Geostrategic Implications*; Konrad Adenauer Stiftung: Hongkong, 2018

(6) Tabatabaei, M.; Aghbashlo, M.; Dehhaghi, M.; Panahi, H. K. S.; Mollahosseini, A.; Hosseini, M.; Soufiyan, M. M. Reactor Technologies for Biodiesel Production and Processing: A Review. *Prog. Energy Combust. Sci.* **2019**, *74*, 239–303. DOI: 10.1016/j.pecs.2019.06.001

(7) Sangeeta; Moka, S.; Pande, M.; Rani, M.; Gakhar, R.; Sharma, M.; Rani, J.; Bhaskarwar, A. N. Alternative Fuels: An Overview of Current Trends and Scope for Future. *Renew. Sustain. Energy Rev.* **2014**, *32*, 697–712. DOI: 10.1016/j.rser.2014.01.023

(8) Mahloujifar, M.; Mansournia, M. A Comparative Study on the Catalytic Performances of Alkali Metals-Loaded KAlSiO4 for Biodiesel Production from Sesame Oil. *Fuel* **2021**, *291*. DOI: 10.1016/j.fuel.2021.120145

(9) Dahdah, E.; Estephane, J.; Taleb, Y.; El Khoury, B.; El Nakat, J.; Aouad, S. The Role of Rehydration in Enhancing the Basic Properties of Mg–Al Hydrotalcites for Biodiesel Production. *Sustain Chem Pharm* **2021**, *22*. DOI: 10.1016/j.scp.2021.100487

(10) Marchetti, J. M.; Miguel, V. U.; Errazu, A. F. Possible Methods for Biodiesel Production. *Renew. Sustain. Energy Rev.* **2007**, *11* (6), 1300–1311. DOI: 10.1016/j.rser.2005.08.006

(11) Gholami, Z.; Tišler, Z.; Rubáš, V. Recent Advances in Fischer-Tropsch Synthesis Using Cobalt-Based Catalysts: A Review on Supports, Promoters, and Reactors. *Catal. Rev. Sci. Eng.* **2021**, *63* (3), 512–595. DOI: 10.1080/01614940.2020.1762367

(12) Martinelli, M.; Gnanamani, M. K.; LeViness, S.; Jacobs, G.; Shafer, W. D. An Overview of Fischer-Tropsch Synthesis: XtL Processes, Catalysts and Reactors. *Appl. Catal. A Gen.* **2020**, *608*. DOI: 10.1016/j.apcata.2020.117740

(13) Böhringer, W.; Kotsiopoulos, A.; De Boer, M.; Knottenbelt, C.; Fletcher, J. C. Q. Selective Fischer-Tropsch wax hydrocracking—opportunity for improvement of overall gas-to-liquids processing. *Stud. Surf. Sci. Catal.* **2007**, *163*, 345–365. DOI: 10.1016/S0167-2991(07)80488-5

(14) Mahmoudi, H.; Mahmoudi, M.; Doustdar, O.; Jahangiri, H.; Tsolakis, A.; Gu, S.; LechWyszynski, M. A Review of Fischer Tropsch Synthesis Process, Mechanism, Surface Chemistry and Catalyst Formulation. *Biofuels Eng.* **2017**, *2* (1), 11–31. DOI: 10.1515/bfuel-2017-0002

(15) Rommens, K. T.; Saeys, M. Molecular Views on Fischer-Tropsch Synthesis. *Chem. Rev.* **2023**, *123* (9), 5798–5858. DOI: 10.1021/acs.chemrev.2c00508

(16) Daga, Y.; Kizilkaya, A. C. Mechanistic Insights into the Effect of Sulfur on the Selectivity of Cobalt-Catalyzed Fischer–Tropsch Synthesis: A DFT Study. *Catalysts* **2022**, *12* (4). DOI: 10.3390/catal12040425

(17) Chen, C.; Wang, Q.; Zhang, R.; Hou, B.; Li, D.; Jia, L.; Wang, B. High Coverage CO Adsorption and Dissociation on the Co(0001) and Co(100) Surfaces from DFT and Thermodynamics. *Appl. Catal. A Gen.* **2016**, *523*, 209–220. DOI: 10.1016/j.apcata.2016.06.013

(18) Zhuo, M.; Tan, K. F.; Borgna, A.; Saeys, M. Density Functional Theory Study of the Co Insertion Mechanism for Fischer-Tropsch Synthesis over Co Catalysts. *J. Phys. Chem. C* **2009**, *113* (19), 8357–8365. DOI: 10.1021/jp900281h

(19) Chen, C.; Wang, Q.; Wang, G.; Hou, B.; Jia, L.; Li, D. Mechanistic Insight into the C2 Hydrocarbons Formation from Syngas on Fcc-Co(111) Surface: A DFT Study. *J. Phys. Chem. C* **2016**, *120* (17), 9132–9147. DOI: 10.1021/acs.jpcc.5b09634

(20) Gunasooriya, G. T. K. K.; Van Bavel, A. P.; Kuipers, H. P. C. E.; Saeys, M. Key Role of Surface Hydroxyl Groups in C-O Activation during Fischer-Tropsch Synthesis. *ACS Catal.* **2016**, *6* (6), 3660–3664. DOI: 10.1021/acscatal.6b00634

(21) Pichler, H.; Schulz, H. Recent Results in Synthesis of Hydrocarbons from CO and H2. *Chem. Ing. Technol.* **1970**, *42* (18), 1162–1174

(22) Sie, S. T.; Krishna, R. Fundamentals and Selection of Advanced Fischer-Tropsch Reactors. *Appl. Catal. A: Gen.* **1999**, *186* (1-2*)*, 55–70. DOI: 10.1016/S0926-860X(99)00164-7

(23) Kasipandi, S.; Bae, J. W. Recent Advances in Direct Synthesis of Value-Added Aromatic Chemicals from Syngas by Cascade Reactions over Bifunctional Catalysts. *Adv. Mater.* **2019**, *31* (34), 1803390. DOI: 10.1002/adma.201803390.

(24) Cheng, K.; Kang, J.; King, D. L.; Subramanian, V.; Zhou, C.; Zhang, Q.; Wang, Y. Advances in Catalysis for Syngas Conversion to Hydrocarbons. *Adv. Catal.* **2017**, *60*, 125–208. DOI: 10.1016/bs.acat.2017.09.003

(25) Gual, A.; Godard, C.; Castillón, S.; Curulla-Ferré, D.; Claver, C. Colloidal Ru, Co and Fe-Nanoparticles: Synthesis and Application as Nanocatalysts in the Fischer-Tropsch Process. *Catal. Today* **2012**, *183* (1), 154–171. DOI: 10.1016/j.cattod.2011.11.025.

(26) Eschemann, T. O.; Oenema, J.; De Jong, K. P. Effects of Noble Metal Promotion for Co/TiO2 Fischer-Tropsch Catalysts. *Catal. Today* **2016**, *261*, 60–66. DOI: 10.1016/j.cattod.2015.06.016

(27) Martínez, A.; López, C.; Márquez, F.; Díaz, I. Fischer-Tropsch Synthesis of Hydrocarbons over Mesoporous Co/SBA-15 Catalysts: The Influence of Metal Loading, Cobalt Precursor, and Promoters. *J. Catal.* **2003**, *220* (2), 486–499. DOI: 10.1016/S0021-9517(03)00289-6

(28) Zhang, H.; Chu, W.; Zou, C.; Huang, Z.; Ye, Z.; Zhu, L. Promotion Effects of Platinum and Ruthenium on Carbon Nanotube Supported Cobalt Catalysts for Fischer-Tropsch Synthesis. *Catal. Lett.* **2011**, *141* (3), 438–444. DOI: 10.1007/s10562-010-0536-4.

(29) Shimura, K.; Miyazawa, T.; Hanaoka, T.; Hirata, S. Fischer-Tropsch Synthesis over TiO2 Supported Cobalt Catalyst: Effect of TiO2 Crystal Phase and Metal Ion Loading. *Appl. Catal. A Gen.* **2013**, *460–461*, 8–14. DOI: 10.1016/j.apcata.2013.04.023

(30) Storsæter, S.; Tøtdal, B.; Walmsley, J. C.; Tanem, B. S.; Holmen, A. Characterization of Alumina-, Silica-, and Titania-Supported Cobalt Fischer-Tropsch Catalysts. *J. Catal.* **2005**, *236* (1), 139–152. DOI: 10.1016/j.jcat.2005.09.021

(31) Ma, W.; Jacobs, G.; Keogh, R. A.; Bukur, D. B.; Davis, B. H. Fischer-Tropsch Synthesis: Effect of Pd, Pt, Re, and Ru Noble Metal Promoters on the Activity and Selectivity of a 25%Co/Al2O3 Catalyst. *Appl. Catal. A Gen.* **2012**, *437*, 1–9. DOI: 10.1016/j.apcata.2012.05.037

(32) Zhang, T.; Wu, Y.; Zhang, J.; Zhang, Q.; Yang, G.; Tsubaki, N.; Tan, Y. Insight into Activation of CO and Initial C2 Oxygenate Formation during Synthesis of Higher Alcohols from Syngas on the Model Catalyst K2O/Cu(111) Surface. *Appl. Surf. Sci.* **2019**, *479*, 55–63. DOI: 10.1016/j.apsusc.2019.02.046

(33) Li, Z.; Zhong, L.; Yu, F.; An, Y.; Dai, Y.; Yang, Y.; Lin, T.; Li, S.; Wang, H.; Gao, P.; Sun, Y.; He, M. Effects of Sodium on the Catalytic Performance of CoMn Catalysts for Fischer-Tropsch to Olefin Reactions. *ACS Catal.* **2017**, *7* (5), 3622–3631. DOI: 10.1021/acscatal.6b03478

(34) Zhang, Z.; Liu, S.; Hou, X.; Qi, L.; Li, W. Effect of Potassium on Carbon Adsorption on the Co(0001) Surface. *J. Mol. Model.* **2020**, *26*, 1–9. DOI: 10.1007/s00894-020-04390-9

(35) Zhang, C.; Li, S.; Zhong, L.; Sun, Y. Theoretical Insights into Morphologies of Alkali-Promoted Cobalt Carbide Catalysts for Fischer-Tropsch Synthesis. *J. Phys. Chem. C* **2021**, *125* (11), 6061–6072. DOI: 10.1021/acs.jpcc.0c09164

(36) Den Breejen, J. P.; Radstake, P. B.; Bezemer, G. L.; Bitter, J. H.; Frøseth, V.; Holmen, A.; De Jong, K. P. On the Origin of the Cobalt Particle Size Effects in Fischer-Tropsch Catalysis. *J. Am. Chem. Soc.* **2009**, *131* (20), 7197–7203. DOI: 10.1021/ja901006x

(37) Agrawal, R.; Phatak, P.; Spanu, L. Effect of Phase and Size on Surface Sites in Cobalt Nanoparticles. *Catal. Today* **2018**, *312*, 174–180. DOI: 10.1016/j.cattod.2018.03.064

(38) Van Etten, M. P. C.; Zijlstra, B.; Hensen, E. J. M.; Filot, I. A. W. Enumerating Active Sites on Metal Nanoparticles: Understanding the Size Dependence of Cobalt Particles for CO Dissociation. *ACS Catal.* **2021**, *11* (14), 8484–8492. DOI: 10.1021/acscatal.1c00651

(39) Van Helden, P.; Ciobîcə, I. M.; Coetzer, R. L. J. The Size-Dependent Site Composition of FCC Cobalt Nanocrystals. *Catal. Today* **2016**, *261*, 48–59. DOI: 10.1016/j.cattod.2015.07.052

(40) ten Have, I. C.; Weckhuysen, B. M. The Active Phase in Cobalt-Based Fischer-Tropsch Synthesis. *Chem. Catalysis* **2021**, *1* (2), 339–363. DOI: 10.1016/j.checat.2021.05.011

(41) Nie, L.; Li, Z.; Kuang, T.; Lyu, S.; Liu, S.; Zhang, Y.; Peng, B.; Li, J.; Wang, L. Role of Well-Defined Cobalt Crystal Facets in Fischer-Tropsch Synthesis: A Combination of Experimental and Theoretical Studies. *Chem. Commun.* **2019**, *55* (71), 10559–10562. DOI: 10.1039/c9cc05528b

(42) Qin, C.; Hou, B.; Wang, J.; Wang, Q.; Wang, G.; Yu, M.; Chen, C.; Jia, L.; Li, D. Crystal-Plane-Dependent Fischer-Tropsch Performance of Cobalt Catalysts. *ACS Catal.* **2018**, *8* (10), 9447–9455. DOI: 10.1021/acscatal.8b01333

(43) Jeske, K.; Kizilkaya, A. C.; López-Luque, I.; Pfänder, N.; Bartsch, M.; Concepción, P.; Prieto, G. Design of Cobalt Fischer-Tropsch Catalysts for the Combined Production of Liquid Fuels and Olefin Chemicals from Hydrogen-Rich Syngas. *ACS Catal.* **2021**, *11* (8), 4784–4798. DOI: 10.1021/acscatal.0c05027

(44) Pei, Y.-P.; Liu, J.-X.; Zhao, Y.-H.; Ding, Y.-J.; Liu, T.; Dong, W.-D.; Zhu, H.-J.; Su, H.-Y.; Yan, L.; Li, J.-L.; Li, W.-X. High Alcohols Synthesis via Fischer–Tropsch Reaction at Cobalt Metal/Carbide Interface. *ACS Catal.* **2015**, *5* (6), 3620–3624. DOI: 10.1021/acscatal.5b00791

(45) R Rupprechter, G. Surface Science Approach to Heterogeneous Catalysis. *Surf. Interface Sci.* **2016**, 459–528. DOI: 10.1002/9783527680573.ch39

(46) Poree, C.; Schoenebeck, F. A Holy Grail in Chemistry: Computational Catalyst Design: Feasible or Fiction? *Acc. Chem. Res.* **2017**, *50* (3), 605–608. DOI: 10.1021/acs.accounts.6b00606

(47) Soyemi, A.; Szilvási, T. Trends in Computational Molecular Catalyst Design. *Dalton Trans.* **2021**, *50* (30), 10325–10339. DOI: 10.1039/d1dt01754c

(48) Chen, W.; Lin, T.; Dai, Y.; An, Y.; Yu, F.; Zhong, L.; Li, S.; Sun, Y. Recent Advances in the Investigation of Nanoeffects of Fischer-Tropsch Catalysts. *Catal. Today* **2018**, *311*, 8–22. DOI: 10.1016/j.cattod.2017.09.019

(49) Chen, L.; Song, G.; Fu, Y.; Shen, J. The Effects of Promoters of K and Zr on the Mesoporous Carbon Supported Cobalt Catalysts for Fischer-Tropsch Synthesis. *J. Colloid Interface Sci.* **2012**, *368* (1), 456–461. DOI: 10.1016/j.jcis.2011.11.030

(50) Dai, Y.; Yu, F.; Li, Z.; An, Y.; Lin, T.; Yang, Y.; Zhong, L.; Wang, H.; Sun, Y. Effect of Sodium on the Structure-Performance Relationship of Co/SiO2 for Fischer-Tropsch Synthesis. *Chin. J. Chem.* **2017**, *35* (6), 918–926. DOI: 10.1002/cjoc.201600748

(51) Huo, C.F.; Wu, B.-S.; Gao, P.; Yang, Y.; Li, Y.-W.; Jiao, H. The Mechanism of Potassium Promoter: Enhancing the Stability of Active Surfaces. *Angew. Chem. Int. Ed.* **2011**, *50* (32), 7403-7406. DOI: 10.1002/anie.201007484

(52) Yang, T.; Wen, X. D.; Li, Y. W.; Wang, J.; Jiao, H. Interaction of Alkali Metals with the Fe3O4(1 1 1) Surface. *Surf. Sci.* **2009**, *603* (1), 78–83. DOI: 10.1016/j.susc.2008.10.020

(53) Yu, H.; Wei, Y.; Lin, T.; Wang, C.; An, Y.; Yu, F.; Sun, F.; Jiang, Z.; Sun, Y.; Zhong, L. Identifying the Performance Descriptor in Direct Syngas Conversion to Long-Chain α-Olefins over Ruthenium-Based Catalysts Promoted by Alkali Metals. *ACS Catal.* **2023**, *13* (6) 3949–3959. DOI: 10.1021/acscatal.2c06158

(54) Li, J.; Cheng, X.; Zhang, C.; Wang, J.; Dong, W.; Yang, Y.; Li, Y. Alkalis in Iron-Based Fischer–Tropsch Synthesis Catalysts: Distribution, Migration and Promotion. *J. Chem. Technol. Biotechnol.* **2017**, *92* (6), 1472–1480. DOI: 10.1002/jctb.5152

(55) Chen, Q.; Svenum, I. H.; Qi, Y.; Gavrilovic, L.; Chen, D.; Holmen, A.; Blekkan, E. A. Potassium Adsorption Behavior on Hcp Cobalt as Model Systems for the Fischer-Tropsch Synthesis: A Density Functional Theory Study. *Phys. Chem. Chem. Phys.* **2017**, *19* (19), 12246–12254. DOI: 10.1039/c7cp00620a

(56) Han, J. W.; Li, L.; Sholl, D. S. Density Functional Theory Study of H and CO Adsorption on Alkali-Promoted Mo2C Surfaces. *J. Phys. Chem. C* **2011**, *115* (14), 6870–6876. DOI: 10.1021/jp200950a

(57) Politano, A.; Formoso, V.; Chiarello, G. Alkali-Promoted CO Dissociation on Cu(111) and Ni(111) at Room Temperature. *J. Chem. Phys.* **2008**, *129* (16). DOI: 10.1063/1.2996133

(58) Liu, Z. P.; Hu, P. An Insight into Alkali Promotion: A Density Functional Theory Study of CO Dissociation on K/Rh(111). *J. Am. Chem. Soc.* **2001**, *123* (50), 12596–12604. DOI: 10.1021/ja011446y

(59) van Helden, P.; Ciobëcă, I. M. A DFT Study of Carbon in the Subsurface Layer of Cobalt Surfaces. *ChemPhysChem* **2011**, *12* (16), 2925–2928. DOI: 10.1002/cphc.201100440

(60) Ciobîcă, I. M.; van Santen, R. A.; van Berge, P. J.; van de Loosdrecht, J. Adsorbate Induced Reconstruction of Cobalt Surfaces. *Surf. Sci.* **2008**, *602* (1), 17–27. DOI: 10.1016/j.susc.2007.09.060

(61) Zonnevylle, M. C.; Geerlings, J. J. C.; Van Santen, R. A. Conversion of Surface Carbidic to Subsurface Carbon on Cobalt (0001): A Theoretical Study. *Surf. Sci.* **1990**, *240* (1-3), 253-262. DOI: 10.1016/0039-6028(90)90746-U

(62) Zijlstra, B.; Broos, R. J. P.; Chen, W.; Oosterbeek, H.; Filot, I. A. W.; Hensen, E. J. M. Coverage Effects in CO Dissociation on Metallic Cobalt Nanoparticles. *ACS Catal.* **2019**, *9* (8), 7365–7372. DOI: 10.1021/acscatal.9b01967

(63) Ma, S. H.; Jiao, Z. Y.; Zhang, X. Z.; Dai, X. Q. Alkali Metal Induced Effects on Coadsorbed Carbon Monoxide on Co(0001): A Density Functional Theory Study. *Comput. Theor. Chem.* **2013**, *1009*, 55–59. DOI: 10.1016/j.comptc.2012.12.028

(64) Blöchl, P. E. Projector Augmented-Wave Method. *Phys. Rev. B* **1994**, *50* (24), 17953. DOI: 10.1103/PhysRevB.50.17953

(65) Hyldgaard, P.; Jiao, Y.; Shukla, V. Screening Nature of the van Der Waals Density Functional Method: A Review and Analysis of the Many-Body Physics Foundation. *J. Phys. Condens. Matter* **2020**, *32* (39). DOI: 10.1088/1361-648X/ab8250

(66) Sit, P.; Zhang, L. Density Functional Theory in Heterogeneous Catalysis. In *Heterogeneous Catalysts: Advanced Design, Characterization and Applications*, *2*, pp 405-418

(67) Kurth, S.; Marques, M.A.L.; Gross, E.K.U. Electronic structure: Density functional theory, **2003**

(68) Peng, Q.; Duarte, F.; Paton, R. S. Computing Organic Stereoselectivity—from Concepts to Quantitative Calculations and Predictions. *Chem. Soc. Rev.* **2016**, *45* (22), 6093–6107. DOI: 10.1039/c6cs00573j

(69) Shan, N.; Zhou, M.; Hanchett, M. K.; Chen, J.; Liu, B. Practical Principles of Density Functional Theory for Catalytic Reaction Simulations on Metal Surfaces – from Theory to Applications. *Mol. Simul.* **2017**, *43* (10–11), 861–885. DOI: 10.1080/08927022.2017.1303687

(70) Ke, H.; Taylor, C. D. Density Functional Theory: An Essential Partner in the Integrated Computational Materials Engineering Approach to Corrosion. *Corrosion* **2019**, *75* (7), 708–726. DOI: 10.5006/3050

(71) Chen, B. W. J.; Xu, L.; Mavrikakis, M. Computational Methods in Heterogeneous Catalysis. *Chem. Rev.* **2020**, *121* (2), 1007–1048. DOI: 10.1021/acs.chemrev.0c01060

(72) Monkhorst, H. J.; Pack, J. D. Special Points for Brillouin-Zone Integrations. *Phys. Rev. B* **1976**, *13* (12), 5188. DOI: 10.1103/PhysRevB.13.5188

(73) Tang, W.; Sanville, E.; Henkelman, G. A Grid-Based Bader Analysis Algorithm without Lattice Bias. *J. Phys. Condens. Matter* **2009**, *21* (8). DOI: 10.1088/0953-8984/21/8/084204

(74) Sanville, E.; Kenny, S. D.; Smith, R.; Henkelman, G. Improved Grid-Based Algorithm for Bader Charge Allocation. *J. Comput. Chem.* **2007**, *28* (5), 899–908. DOI: 10.1002/jcc.20575

(75) Henkelman, G.; Arnaldsson, A.; Jónsson, H. A Fast and Robust Algorithm for Bader Decomposition of Charge Density. *Comput. Mater. Sci.* **2006**, *36* (3), 354–360. DOI: 10.1016/j.commatsci.2005.04.010

(76) Peters, B. *In Reaction rate theory and rare events*; Elsevier, **2017**

(77) Henkelman, G.; Jónsson, H. A Dimer Method for Finding Saddle Points on High Dimensional Potential Surfaces Using Only First Derivatives. *J. Chem. Phys.* **1999**, *111* (15), 7010–7022. DOI: 10.1063/1.480097

(78) Nudged Elastic Band (NEB). https://www.scm.com/doc/AMS/Tasks/NEB (accessed 2023-11-15)

(79) Henkelman, G.; Uberuaga, B. P.; Jónsson, H. Climbing Image Nudged Elastic Band Method for Finding Saddle Points and Minimum Energy Paths. *J. Chem. Phys.* **2000**, *113* (22), 9901–9904. DOI: 10.1063/1.1329672

(80) Wang, Y. X.; Wang, G. C. Water Dissociation on K2O-Pre-Adsorbed Transition Metals: A Systematic Theoretical Study. *Phys. Chem. Chem. Phys.* **2018**, *20* (30), 19850–19859. DOI: 10.1039/c8cp03587c

(81) Cornaro, U.; Rossini, S.; Montanari, T.; Finocchio, E.; Busca, G. K-Doping of Co/Al2O3 Low Temperature Fischer-Tropsch Catalysts. *Catal. Today* **2012**, *197* (1), 101–108. DOI: 10.1016/j.cattod.2012.07.005

(82) Mojet, B. L.; Ebbesen, S. D.; Lefferts, L. Light at the Interface: The Potential of Attenuated Total Reflection Infrared Spectroscopy for Understanding Heterogeneous Catalysis in Water. *Chem. Soc. Rev.* **2010**, *39* (12), 4643–4655. DOI: 10.1039/c0cs00014k

(83) De Boer, J. H.; Blyholder, G. Molecular Orbital View of Chemisorbed Carbon Monoxide. *J. Phys. Chem.* **1964**, *68* (10), 2772–2777. DOI: 10.1021/j100792a006

(84) Shetty, S.; Van Santen, R. A. CO Dissociation on Ru and Co Surfaces: The Initial Step in the Fischer-Tropsch Synthesis. *Catal. Today* **2011**, *171* (1), 168–173. DOI: 10.1016/j.cattod.2011.04.006

(85) Corral Valero, M.; Raybaud, P. Stability of Carbon on Cobalt Surfaces in Fischer-Tropsch Reaction Conditions: A DFT Study. *J. Phys. Chem. C* **2014**, *118* (39), 22479–22490. DOI: 10.1021/jp5004177

APPENDIX A

Adsorption Sites and Corresponding Adsorption Energies on Alkali Promoted p(3x3) Surface

Adsorption Sites

Li_2O/Co(111)

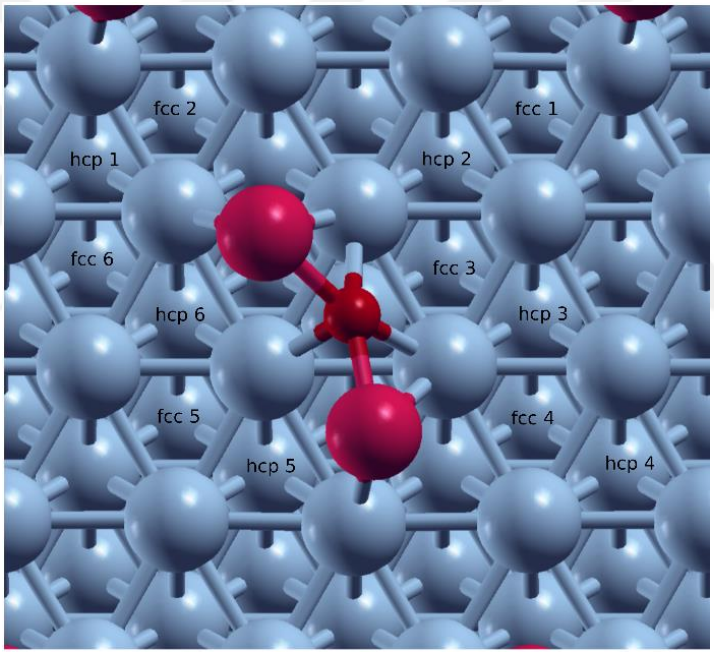

Figure A1. Possible adsorption sites on 0.11 ML Li_2O promoted Co(111) surface

Na_2O/Co(111)

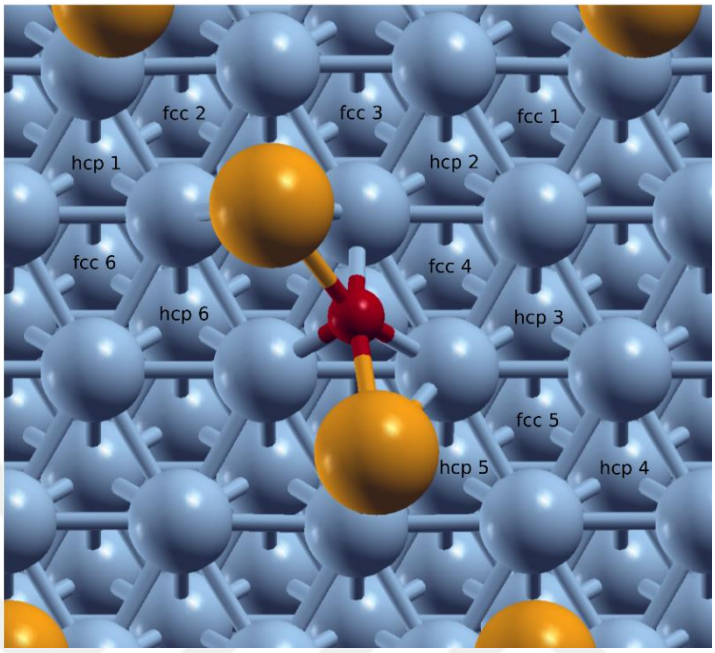

Figure A2. Possible adsorption sites on 0.11 ML Na_2O promoted Co(111) surface

K_2O/Co(111)

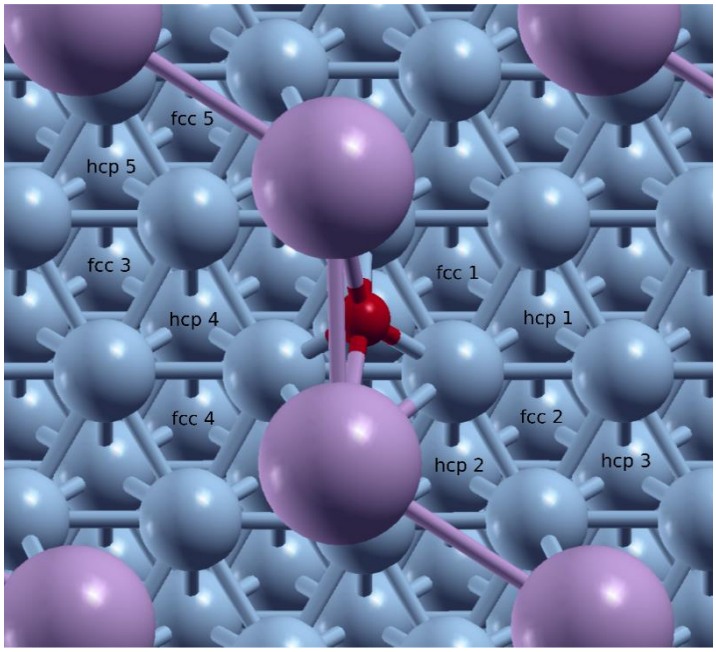

Figure A3. Possible adsorption sites on 0.11 ML K_2O promoted Co(111) surface

Adsorption Energies

$Li_2O/Co(111)$

Table A1. Adsorption energies on different adsorption sites on the 0.11 ML $Li_2O/Co(111)$ surface

Adsorbed Species	Adsorption Sites	Adsorption Energy (eV)
CO	hcp4	-1.543
	fcc2	-2.091
	fcc4	-1.785
	fcc5	-1.836
	fcc6	-1.788
C	hcp1	-6.562
	hcp4	-6.371
	hcp5	-6.511
	fcc1	-6.382
	fcc2	-6.792
	fcc5	-6.258
	fcc6	-6.379
O	hcp1	-5.540
	hcp4	-5.404
	fcc1	-5.720
	fcc2	-6.069
	fcc4	-5.755
	fcc5	-5.691
	fcc6	-5.719
H	hcp2	-2.691
	hcp3	-2.689
	hcp4	-2.749
	hcp5	-2.741
	hcp6	-2.735
	fcc1	-2.751
	fcc2	-2.756
	fcc 4	-2.739
	fcc5	-2.687
	fcc6	-2.750

Na_2O/Co(111)

Table A2. Adsorption energies on different adsorption sites on the 0.11 ML Na_2O/Co(111) surface

Adsorbed Species	Adsorption Sites	Adsorption Energy (eV)
CO	hcp1	-1.935
	hcp2	-1.778
	fcc2	-1.896
	fcc6	-1.648
C	hcp2	-6.249
	hcp3	-6.094
	hcp4	-6.390
	hcp5	-6.422
	hcp6	-6.294
	fcc1	-6.295
	fcc2	-6.416
	fcc6	-6.416
O	hcp1	-5.616
	hcp2	-5.463
	fcc5	-5.336
H	hcp1	-2.643
	hcp2	-2.653
	hcp4	-2.621
	hcp5	-2.639
	fcc1	-2.627
	fcc2	-2.688
	fcc3	-2.580
	fcc4	-2.598

K_2O/Co(111)

Table A3. Adsorption energies on different adsorption sites on the 0.11 ML K_2O/Co(111) surface

Adsorbed Species	Adsorption Sites	Adsorption Energy (eV)
CO	hcp4	-1.838
	hcp5	-1.948
	fcc4	-1.796
	fcc5	-1.857
C	hcp3	-6.518
	hcp5	-6.487
	fcc3	-6.185
	fcc5	-6.350
O	hcp1	-5.528
	hcp3	-5.685
	hcp5	-5.685
	fcc1	-5.423
	fcc4	-5.557
	fcc5	-5.741
H	hcp1	-2.673
	hcp5	-2.687
	fcc2	-2.678
	fcc5	-2.723

APPENDIX B

Adsorption Sites and Corresponding Adsorption Energies on Alkali Promoted p(4x4) Surface

Adsorption Sites

Li_2O/Co(111)

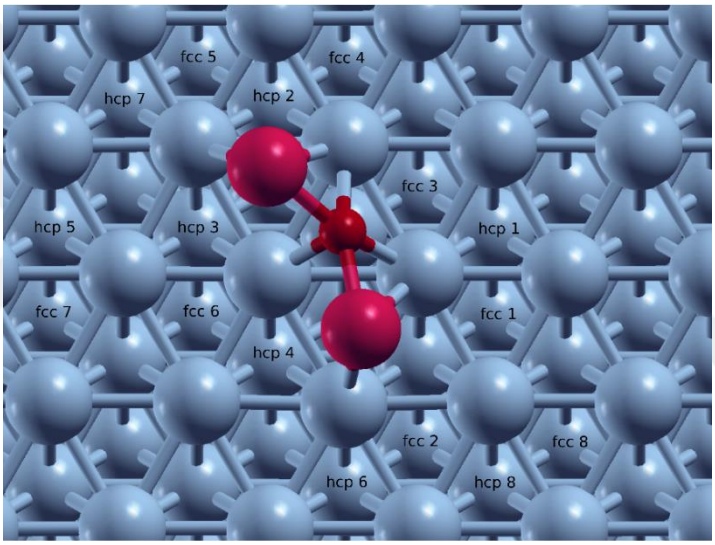

Figure B1. Possible adsorption sites on 0.06 ML Li_2O promoted Co(111) surface

Na_2O/Co(111)

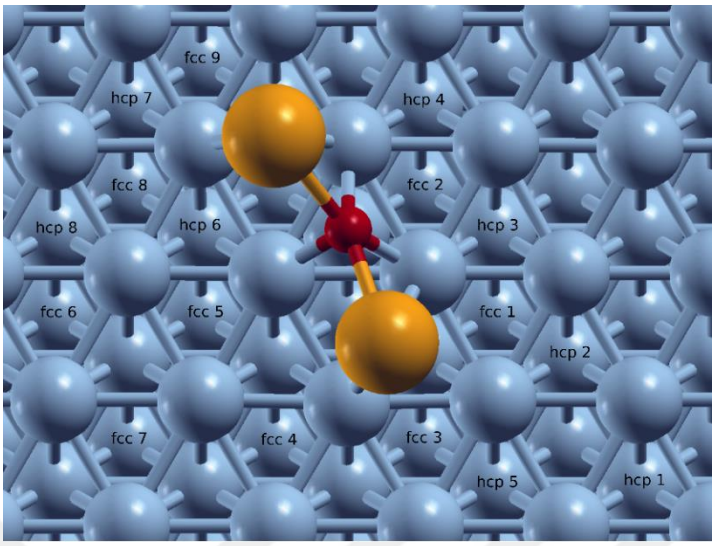

Figure B2. Possible adsorption sites on 0.06 ML Na_2O promoted Co(111) surface

K_2O/Co(111)

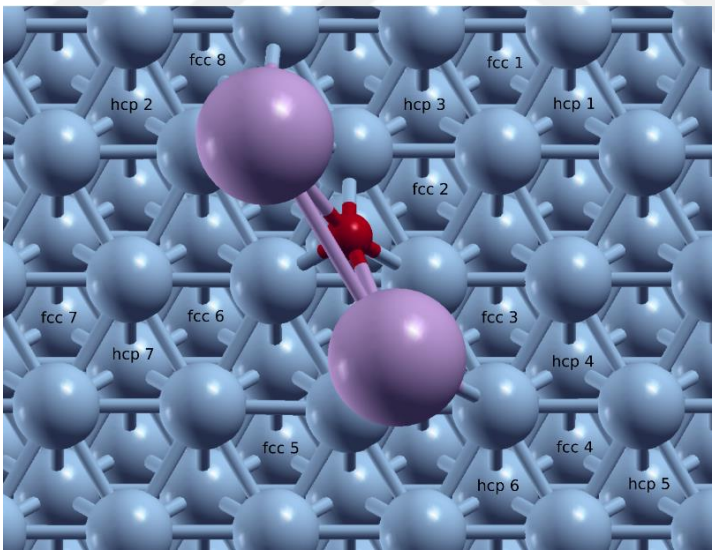

Figure B3. Possible adsorption sites on 0.06 ML K_2O promoted Co(111) surface

Adsorption Energies

Li_2O/Co(111)

Table B1. Adsorption energies on different adsorption sites on the 0.06 ML Li_2O/Co(111) surface

Adsorbed Species	Adsorption Sites	Adsorption Energy (eV)
CO	hcp1	-1.606
	hcp3	-1.745
	hcp4	-1.746
	hcp5	-1.416
	hcp6	-1.709
	hcp7	-1.710
	hcp8	-1.469
	fcc1	-1.709
	fcc4	-1.709
	fcc5	-1.792
	fcc6	-1.791
	fcc7	-1.422
	fcc8	-1.461
C	hcp1	-6.217
	hcp2	-6.654
	hcp3	-6.530
	hcp4	-6.529
	hcp5	-6.408
	hcp6	-6.486
	hcp7	-6.487
	hcp8	-6.432
	fcc1	-6.291
	fcc2	-6.479
	fcc4	-6.479
	fcc5	-6.479
	fcc6	-6.219
	fcc7	-6.165
	fcc8	-6.213
O	hcp1	-5.850
	hcp2	-5.852
	hcp5	-5.378
	hcp6	-5.774
	hcp7	-5.544
	hcp8	-5.368
	fcc1	-5.742
	fcc2	-5.813
	fcc3	-5.142
	fcc4	-5.742
	fcc5	-5.813

(cont. on next page)

Table B1. (cont)

	fcc6	-5.613
	fcc7	-5.303
	fcc8	-5.313
H	hcp1	-2.727
	hcp2	-2.757
	hcp3	-2.764
	hcp4	-2.764
	hcp5	-2.801
	hcp6	-2.786
	hcp7	-2.786
	fcc1	-2.776
	fcc2	-2.818
	fcc3	-2.307
	fcc4	-2.776
	fcc5	-2.818
	fcc6	-2.733
	fcc7	-2.821
	fcc8	-2.823

Na_2O/Co(111)

Table B2. Adsorption energies on different adsorption sites on the 0.06 ML Na_2O/Co(111) surface

Adsorbed Species	Adsorption Sites	Adsorption Energy (eV)
CO	hcp1	-1.680
	hcp3	-1.560
	hcp4	-1.531
	fcc5	-1.760
	fcc6	-1.482
	fcc9	-1.707
C	hcp1	-6.510
	hcp2	-6.511
	hcp3	-6.228
	hcp4	-6.228
	hcp5	-6.529
	hcp6	-6.408
	hcp7	-6.492
	hcp8	-6.412
	fcc1	-6.214
	fcc3	-6.338
	fcc4	-6.331
	fcc5	-6.165
	fcc6	-6.167
	fcc7	-6.164
	fcc8	-6.331
O	hcp3	-5.422
	hcp4	-5.423
	hcp6	-5.541
	hcp8	-5.400
	fcc1	-5.474
	fcc3	-5.621
	fcc4	-5.596
	fcc5	-5.449
	fcc6	-5.315
	fcc7	-5.315
	fcc8	-5.598
H	hcp1	-2.766
	hcp2	-2.765
	hcp3	-2.699
	hcp4	-2.697
	hcp5	-2.778
	hcp6	-2.717
	hcp7	-2.767
	hcp8	-2.796
	fcc1	-2.739
	fcc2	-2.787

(cont. on next page)

Table B2. (cont)

	fcc3	-2.772
	fcc4	-2.804
	fcc5	-2.725
	fcc6	-2.809
	fcc7	-2.809
	fcc8	-2.805

K_2O/Co(111)

Table B3. Adsorption energies on different adsorption sites on the 0.06 ML K_2O/Co(111) surface

Adsorbed Species	Adsorption Sites	Adsorption Energy (eV)
CO	hcp1	-1.555
	hcp2	-1.779
	hcp4	-1.741
	hcp5	-1.742
	hcp6	-2.017
	fcc1	-1.801
	fcc3	-1.690
	fcc5	-1.742
	fcc6	-1.875
C	hcp1	-6.402
	hcp2	-6.507
	hcp3	-6.279
	hcp4	-6.522
	hcp5	-6.522
	hcp6	-6.638
	hcp7	-6.435
	fcc1	-6.350
	fcc3	-6.255
	fcc4	-6.337
	fcc5	-6.303
	fcc6	-6.275
	fcc7	-6.332
O	hcp1	-5.410
	hcp3	-5.457
	hcp4	-5.648
	hcp6	-5.705
	hcp7	-5.422
	fcc1	-5.373
	fcc3	-5.485
	fcc4	-5.495
	fcc5	-5.586
	fcc6	-5.517
H	hcp1	-2.789
	hcp2	-2.773
	hcp3	-2.706
	hcp4	-2.772
	hcp5	-2.771
	hcp6	-2.792
	hcp7	-2.774
	fcc1	-2.810
	fcc2	-2.789

(cont. on next page)

Table B3. (cont)

	fcc3	-2.759
	fcc4	-2.803
	fcc5	-2.806
	fcc6	-2.806
	fcc7	-2.808